Optical Study of 2D Magnets and Their Heterostructures for Valleytronics

Ding Zhong

A dissertation

submitted in partial fulfillment of the

requirements for the degree of

Doctor of Philosophy

University of Washington

2019

Reading Committee:

Xiaodong Xu, Chair

Kaimei Fu

Anton Andreev

Program Authorized to Offer Degree:

Physics

University of Washington

Abstract

Optical Study of 2D Magnets and Their Heterostructures for Valleytronics

Ding Zhong

Chair of the Supervisory Committee:

Professor Xiaodong Xu

Department of Physics and Materials Science and Engineering

Electrons in layered van der Waals materials with a honeycomb lattice structure possess a valley degree of freedom in addition to charge and spin, which make van der Waals materials a tantalizing platform for valleytronics research. Among many candidates, transitional metal dichalcogenides (TMDs) have one of the most highly addressable valleys. For example, they possess valley optical selection rule which allows for interplay between light helicity and valley indexes; they also possess valley contrasting Berry curvature which allows for spatial separation of valley current without external field.

In this thesis, we interface a van der Waals magnet—CrI_3 with a representative TMDs—WSe_2 to achieve unprecedented valley control in WSe_2. Topics on optical studies on plain CrI_3 is also

covered. First, we demonstrate that strong exchange field and spin-selective charge hopping occurs at the interface between WSe_2 and CrI_3. The former leads to enhanced control of valley splitting, such as large valley splitting equivalent to Zeeman effect with 13T magnetic field, and rapid valley splitting switch nearly three orders of magnitude faster than can be achieved by the Zeeman effect in bare WSe_2; the later leads to remarkable population control of WSe_2. We then introduce layer-resolved proximity effects in WSe_2/bilayer and trilayer CrI_3 heterostructure and use this knowledge for revealing domain structure in CrI_3 that has never been observed. Next, we unravel the excitation power dependent metamagnetic transition in CrI_3, which is can be utilized for achieving continuous and reversible tuning of the valley splitting and valley polarization in WSe_2. For the second part, which is the optical studies on plain CrI_3, this thesis includes: Using magneto-optic Kerr effect to demonstrate that CrI_3 is the world's first discovered 2d magnet; its bilayer and trilayer have antiferromagnetically coupled ferromagnetic monolayer as their ground state; PL study on CrI_3 reveals photoluminescence at ~1.1eV originated from Frenkel Exciton, with its helicity connected to the magnetic order of itself.

TABLE OF CONTENTS

List of Figures

List of Tables

ACKNOWLEDGEMENTS

I would like to express my gratitude toward Xiaodong Xu, for his outstanding guidance and advice of all time. Behavior is more powerful than words. His passion, endeavor toward scientific discovery has always been motivating me. He not only gave me the right instruction when I was confused but also corrected me at a few critical moments that I utterly needed. Ph.D. is a test of intellect, stamina, and spirit. His supports have helped me through the ups-and-downs of my Ph.D. life. In research, Xiaodong is always capable of grabbing the essence of the data at a glimpse, which reflects his profound understanding of the research field. As a group leader, he has acute sensitivity to research hotspots. During the five years, I saw him leaded our group smoothly transit into the direction of magnet 2d materials, which turn out to be a great decision. His leadership created cohesion that any elite group desires, and undoubtedly lead the group to achieve current reputation and fame. In his group, there is motivating research atmosphere that everyone benefits in it. It is a great fortune to research this group. I believe this group, under his leadership, have a bright future and I wish the best of his career.

I would also like to express my gratitude toward other committee members. Kai-mei Fu generously offered time on her magnet cryostat that helped me through the very first project that I worked on, and later on, offered rigorous analysis and insight to the project. Anton Andreev, thanks for always being supportive over the years.

Thanks to all the collaborators that have contributed to my work. Xiayu Linpeng has been supportive and patient on guiding me through instructions on the magnet cryostat. Thanks for

spending days and nights working with me together to kick off my very first project. Emma Schmidgall shared expertise with me on liquid crystal variable retarder, then generously offered me Matlab scripts and calibration methods, which is essential to me in getting countless valuable data after. Daniel Gamelin and Xiaosong Li have been very helpful in our attempts to understand the behavior of 2d magnets. David Cobden and his students shared us with essential instruments for device fabrication, offer in-depth discussion, were a great help. Our theoretical collaborators, Di Xiao, Wang Yao, Hongyi Yu, and Ran Cheng, thank you for discussions over the Skype, and for making the theoretical model that provides enlightenment and great content to the papers. My work would not be possible without Michell McGuire (at Oak Ridge National Laboratory), and NIMS (Takashi Taniguchi and Kenji Watanabe) generously grew high-quality CrI_3 and hBN used in this work. Arka Majumdar gave me a big boost in my postdoc applications. Your help is highly appreciated.

I would also like to thank my lab mates. Those who welcomed me to the lab gave me support on kicking off my Ph.D. career: Sanfeng Wu, Grant Aivazian, Pasqual Rivera, Helin Cao, Genevieve Clark, John Schaibley, Mitch Jones, and Jason Ross. Mitch instructed me starting from the first day, which leads me to form several important practices we should keep doing that I benefit a lot in the following years. John has profound knowledge on laser, and I consider myself lucky to cross paths with him. From him, I have learned a great deal from his insight on optic elements and alignments. Thanks to Sanfeng Wu for sharing ideas with me about how a research idea is found and how researches are laid out. Sanfeng Special thanks to Kyle, who had put a tremendous amount of excellent work on CrI_3. his way of critical thinking is impressive, and discussion with him had cleared many of puzzles. I wish him the greatest success at Caltech. My Ph.D. also benefited a lot from those who join lab later than me, Bevin Huang, Nathan Wilson,

Tiancheng song and Chenfeng Du, Minhao He, John Cenker, Kyle Hwangbo. Thanks to Bevin Huang for maintaining the magnet cryostat. He is also a great source of laughter, Thanks to Nathan for keeping the lab in order. Good luck to you all and wish you enjoy the rest of your Ph.D. in the lab.

Thanks to all the visiting scientists and postdocs, they are a great source of intellect that has given Ph.D. student like me many pieces of knowledge and supports and helped the group rolling forward: Chunming Liu, Changhua Liu, Qi Zhang, Dmitry Ovchinnikov, Zaiyao Fei, Colin Chow, Changhua Liu. Colin is knowledgeable and innovative. Endless good ideas come out of his mind and for sure will be an excellent researcher for his career. Zaiyao Fei is reliable, humorous and diligent. I wish him the best luck in finding an academic position.

Thanks to my girlfriend Yan Gu, who has been very supportive and thoughtful through the course of my Ph.D. In those emotionally down days, she cheered me up and injected energies that helped to get back to the course. Thanks to my mom and dad. They helped me and encouraged me to chase my dream in the University of Washington, which turned out to be a great decision. When we are separated on the opposite side of the earth, remotely, but surely they cared about me. Their unwavering support gave me strength and made me feel that I could get through any difficulties in life.

DEDICATION

To my family.

Abbreviations

2D – Two Dimensional

PL – Photoluminescence

PRPL – Polarization-resolved Photoluminescence

RMCD – Reflectance Magneto Circular Dichroism

PC – Polycarbonate

HS – Heterostructure

hBN – Hexagonal Boron Nitride

QW – Quantum Well

GMR – Giant Magnetoresistance

PEM – Photoelastic Modulator

LCP – Left Circular Polarization

RCP – Right Circular Polarization

AC – Alternating Current

DC – Direct Current

LMCT – Ligand-to-Metal Charge Transfer

Chapter 1. INTRODUCTION TO TWO-DIMENSIONAL MATERIALS

1.1 THE WORLD OF MATERIALS

Six years ago. When I was an undergraduate student in Peking University, I went to a campus talk with my school mate Shuhao Ye. The talk was about the newly emerged technology at that time: the 3D printing. The idea was that with a blueprint which can be drawn on a computer, the 3D printer uses a nozzle to extrude a melted, plastic-like substance across pixels of the designed object. The substance then dries quickly in air after which the design is materialized. The idea was very new, fancy and attractive, and numerous startup companies were burning money on it. During the talk, the presenter spoke highly about 3D printing. In the end, he concluded: “the industry revolution invented manufactory, which can manufacture identical products for all customers. The 3D printing technology will redefine the concept of manufactory: it manufacture personalized product for every customer, at their own homes. Two hundred years ago, the creation of manufactory gave rise to the first industrial revolution. Today, the 3D printing technology will surely lead to the next!” The uplifting speech lit up the audience and won resounding applause.

After the talk, on our way home, Shuhao Ye and me were sharing idea about the talk. While I was convinced by the speaker, Shuhao didn’t seem to buy what the speaker has said. “The 3D printing is good but it won’t be as good as he promised. The innovation of the 3d printing technology is that it provides freedom to manipulate the shape of the product. It also comes with a fatal drawback: It doesn’t have freedom to choose the materials. If it only works with the material that melts in heat and dries quickly in air, like the plastic he demonstrated with, the product won’t go far. The role that materials play in manufactory should not be overlooked.”

I was shocked by the insight that Shuhao provides, after a few seconds, I must admit that what he said was totally correct. Materials plays an essential role in determined the function of any

product: a spring won't bounce if it were made of wood; a cloth won't keep you warm if it were made of plastic. If we look back on our history, it is marked by the discovery of new materials: the namely "stone age," "bronze age" and "iron age." These hallmarks of human history imply that mastering new material put human's ability to survive the environment, to change the nature, and to conquer another civilization up a level. At present, the innovation on materials is a driving force that has entirely changed the way we live: the purification of silicon is a critical factor for the advent of information era; the denser and denser population in cities is closely connected with the refining of the concrete material. In future, the thirst to master new materials will only get more and more intense. I was glad that I selected physics as my major which allows me to devote my energy into the researching of new materials that is so important to human civilization.

Among the research field of materials, a spectacularly interested research area in materials science is the field of nano materials. The nano materials are more than a volume-reduced version of bulky materials, for the purpose of building more complex structures in given limited space. As materials are exfoliated down to a few atoms thick, the quantum mechanics effect come into play. In addition, the normally ignored surface effect becomes prominent. These effects give rise to rich physics that only belongs to the nano materials, which allows for building devices with precedented functionality.

A rewarding branch in nano materials for discovering new phenomena is the van der Waals materials. These materials have a layered structure so that intralayer atoms are bonded by covalence bond and interlayer atoms are by van der Waals bond. Since van der Waals bonds are naturally weaker, it is possible to break them by exfoliation techniques, to create nanometers thick, even monolayer material. [1] The method was first introduced by A. K. Geim, accomplished with Scotch tape approach (more details in chapter 3)[1]. When the thickness is reduced to a single

atomic layer, the materials is now truly two-dimensional that one cannot divide it further in the vertical dimension. This category has been given a special name “2d materials”. 2d materials have been found use in photovoltaics, semiconductors, electrodes, etc. which is an exploding research direction.

There are many advantages of 2d materials over conventional thin film materials. First of all, prominent surface effect comes into play, which grants distinct property compared with its bulk counterpart, as many examples presented in chapter 2. These effects give rise to unique optical, electrical and information storage-oriented applications. Second, as a natural consequence of its layered atomic structure, an atomically smooth surface can be expected, which means no microscopically dangling bond and perfect in-plane periodicity. These properties means that stacking of heterogeneous materials into new complex heterostructures (HS) creates power devices that possess complex functions due to strong interfacial interactions. Third, the weak van der Waal bond facilitate the fabrication process. Without complex techniques such as molecular beam epitaxy (MBE), using simple scotch tapes to break the van der Waals bonds, one could fabricate van der Waals materials within minutes.

The graphene is the first successfully fabricated 2d material[1]. Since the discovery of graphene, the researchers started to realize that the field of van der Waals materials is a fertile platform for discovering rich physical phenomena. For example, massless electrons were found near the Dirac cone of graphene[2]; Majorana fermion, the concept that was raised in high energy physics was first identified in van der Waals materials[3]; Quantum Spin Hall effect in the absence of magnetic field[4] represent another beautiful theory that was verified experimentally first in van der Waals materials.

Since the thrive of graphene, more and more are materials have been successfully fabricated and added into the 2d family. Different chemical compositions endow them to have a variety of electronic structure, mechanical properties, and optical responses. One that attracted a lot of attention is group-6 transition metal dichalcogenides (TMDs), usually denoted as MX_2, where M represents transition metal atoms (W, Mo) and X represents chalcogen atoms (S, Se, Te). TMDs are semiconductors that are especially special in its 2d form. They are direct bandgap materials as monolayer and indirect bandgap material if the layer number is more than 1[5]. The implication is significant: Due to zero momentum transfer, the optical transition now primarily occurs between the conduction band minimum and valence band maximum, which implies high efficiency in quantum yield, making them an optical addressable materials. Furthermore, optical selection rule locks incident laser's helicity with carriers' spin and valley index, opening the possibility for optical addressable spin and valley material. In this thesis, we will have heavy contents covering study and analysis on TMDs, meanwhile the other protagonist in this thesis is the van der Waals magnetic materials.

1.2 Thesis Outline

In this thesis, we will cover the research results on heterostructure consist of a TMD and a magnetic van der Waals material—WSe_2/CrI_3. It's a semiconductor/magnetic materials heterostructure embodied in van der Waals materials. Rich phenomena were found in this configuration. After reading this thesis, you should be informed how this heterostructure could find its place in spin and valleytronics applications.

In Chapter 2 we will discuss the properties of 2d materials, where we concentrate on graphene and TMDs, introducing several important concepts that is necessary to understand the main body of thesis, presented in later chapters.

In Chapter 3, we will go through the fabrication of 2d materials, including mechanical fabrication and transferring (making heterostructures). Discussion on the fabrication process is not only beneficial for reader who has intention to reproduce the results presented in the thesis, but also aims at giving the reader an idea that how the development of fabrication technique is associated with the discovery of materials and new structure as a consequence.

In chapter 4. We shift our attention toward magnetic heterostructures, where we show that the origin of magnetism relies on exchange interaction, which has a quantum origin instead of dipolar interaction with a classical origin. We present a theoretical model of exchange interaction as the Heitler-London model, which leads us to obtaining an expression for the Heisenberg Hamiltonian. Finally, before moving onto 2d magnetic heterostructure, we discuss briefly on some pre-2d researches on magnetic heterostructures.

In chapter 5, we will start with our work on ferromagnetic semiconductor heterostructures. In this chapter, we built a WSe_2/CrI_3 heterostructure, in which we observed strong interactions that include strong exchange field and spin selective charge hopping across the interface. Upon studying the interaction, we also discovered that micro-sized CrI_3 form magnetic domains for reducing system's domain energy. The domain pattern evolves in magnetic field thus provides a us with certain degrees of freedom to control the valley degrees of freedom in WSe_2.

In chapter 6, with the studies of CrI_3 getting deeper and deeper, we cleaved CrI_3 down to monolayer and studied its magnetic properties with Magneto-Optic Kerr effect (MOKE). Contrary to the Wagner-Mermin theorem, the monolayer CrI_3 exhibits ferromagnetism, manifesting itself as 2d magnetic. Study on bilayer CrI_3 then revealed that the bilayer CrI_3 consist of two antiferromagnetically aligned ferromagnetic monolayers. The contradiction between existing

magnetism in monolayer CrI_3 and the Wagner-Mermin theorem is reconciled by strong Magnetocrystalline anisotropy in CrI_3.

In Chapter 7, we performed photoluminescence (PL) study on fewlayer CrI_3 down to monolayer. We find Frenkel style exciton in CrI_3 which give rise to PL emission at ~1.1eV. The PL emission exhibits strong intrinsic circular polarization connected to its magnetic state. Using ligand field theory, we attribute the emission to between *d-d* transition assisted by phonons.

In chapter 8, we study the two proximity effects in WSe_2/CrI_3 heterostructure with greater depth. Using WSe_2/bilayer and trilayer CrI_3, we unravel the proximity effect by each layer's magnetization. Then by harvesting the proximity using polarization-resolved photoluminescence and reflectance magneto circular dichroism, we image the magnetic domain of bilayer CrI_3, determined the ground state of bilayer CrI_3.

In chapter 8, we discuss another great property of WSe_2/CrI_3 heterostructure, which is optical tuning of proximity effect which can be used for valley manipulation in WSe_2/CrI_3 heterostructure.

Chapter 2. 2D MATERIALS

In this Chapter, we review important theoretical and experimental work in field of 2d materials.

2.1 GRAPHENE

Graphene, a single layer of graphite, the first isolated 2d material, marks the start of the new era in condensed matter physics [1, 2, 6].

It's quite meaningful to know meanwhile a lot to learn from how graphene, such a big hit to the scientific community was discovered. The path was twisty meanwhile miraculous. Enlighten by graphite researches, with a raw idea, Andre. K. Geim gave his graduate student Da a tablet of pyrolytic graphite, asked him to thin it down as much as possible. The instruction at this moment was to use a polishing machine that has submicron accuracy. With this method, Da achieved a 10μm thick piece of graphite, which was far from enough; Then he suggested him to try a finer polishing liquid. It also turned out to be a failure and the whole table was polished away with no yield. The idea was not thrown into the trash can and the breakthrough happened when Oleg Shklyarevskii, an expert in STM, showed Andre a tape attached with graphite. It was a graphite tape that was used to make a reference sample for STM. In routine practice, they prepare a fresh surface of graphite by removing the top layer with tape. However, the tapes were never paid attention to and were always thrown away. Andre quickly realized that this was the right direction, they examined the graphite on a tape, which turned out to be much thinner than the best they can achieve with a polishing machine.

After that, another student Kostya took over and pushed the project one step further—transferring the graphite flakes onto the glass slides. With good fortune, a bonus was discovered

that the interference color provided intuitive judging of the flake thickness, that led them to identify a monolayer graphite, as it was named “graphene”.

The story was not yet complete at this point, he could have published the result, instead, he made a remarkable decision, he decided to measure the conductivity before announcing the discovery. This act was very brilliant from the hindsight, and it could be one of the factors that set him apart from ordinary researchers. It was the fantastic electric property that he discovered that eventually drew the attention of subsequent researchers into this field. A. K. Geim et al took months to learn how to identify monolayer with atomic force microscopy, electron beam lithography to define hall bars. With these results, they composed the groundbreaking paper that was published on *science*[1]. This experience, as he summarized after winning Nobel Prize[7], told him “poking in new directions, even randomly, is more rewarding than is generally perceived”.

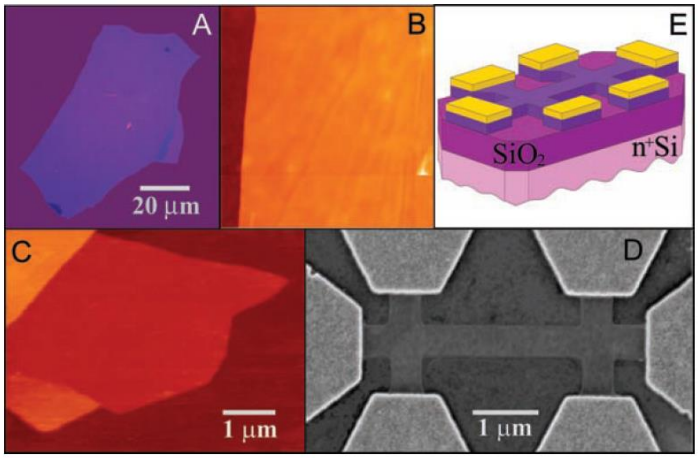

Figure 2.1. Graphene micrograph. (A) micrograph of a 3nm thick graphite on top of a (B) Atomic Force Microscope (AFM) image of 2um by 2um area of this flake. (C) AFM image of a single layer graphene. The monolayer is 0.8nm height under AFM. (D) Scanning electron microscope image of one of our experimental devices prepared from few-layer graphene. (E) Schematic of the device in (D). image reproduced from Novoselov, K.S., et al., Electric field effect in atomically thin carbon films. Science, 2004. 306(5696): p. 666-9.

Before graphene was practically fabricated, this task was deemed impossible according to theoretical predictions. Calculation showed that when comparing many configurations with more than 24000 carbon atoms (that is a flat sheet with ~25nm), various 3d configurations, such as carbon nanotubes, fullerene, are energetically more favorable than graphene[8]. For larger sizes, theory also showed that graphene is unstable with respect to scrolling, when one considers

competing contributions from the bending and surface energies[9]. This restrictions were circumvented by the merit of the fabrication process. First, the crystal was created initially in 3d instead of 2d, which quenches diverging thermal fluctuations. Second, when graphene was cleaved, the process was carried out at room temperature, such that the energy barrier remained sufficiently high. With both effort and luck, they successfully fabricated graphene that can remain flat on the substrate although it is energetically unfavorable.

Graphene is a single planar structure of carbon atoms arranged in a honeycomb lattice. One *s* orbital and two *p* orbitals exhibit in *sp*2 hybridization. Two adjacent carbon atoms are bonded by σ bond separated by 1.42 Å. The extra *p* orbital now orients in the perpendicular direction to the plane structure, is free to bond covalently with neighboring carbon atoms, forming π band. Since each p orbital has an extra electron, the orbital is half-filled. In each unit cell, there are two atoms located at site A and site B with basis vectors a_1 and a_2, as shown in Figure 2.2A. At the corner of Brillouin Zone,

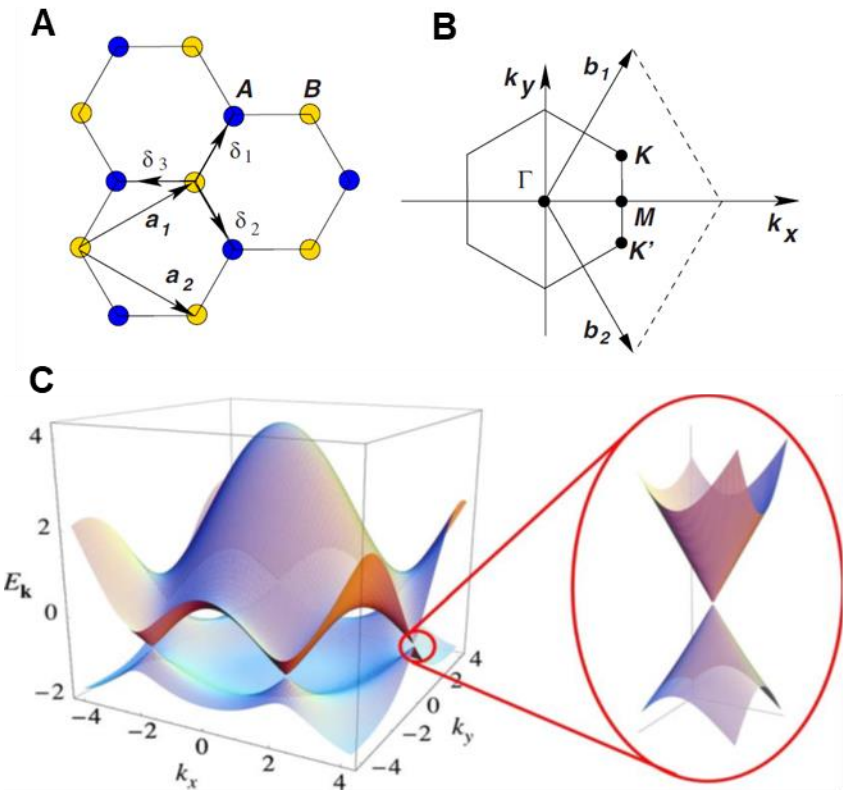

Figure 2.2. Graphene electronic band structure. (A) lattice structure of graphene, a1 and a2 are basis vectors, A and B are two sublattice site that make up a unit cell. **(B)**Brillouin Zone of graphene, the Dirac points are located at K and K' (or ±K). **(C)** The band structure of graphene. Six Dirac cones are observed of which 2 are inequivalent.

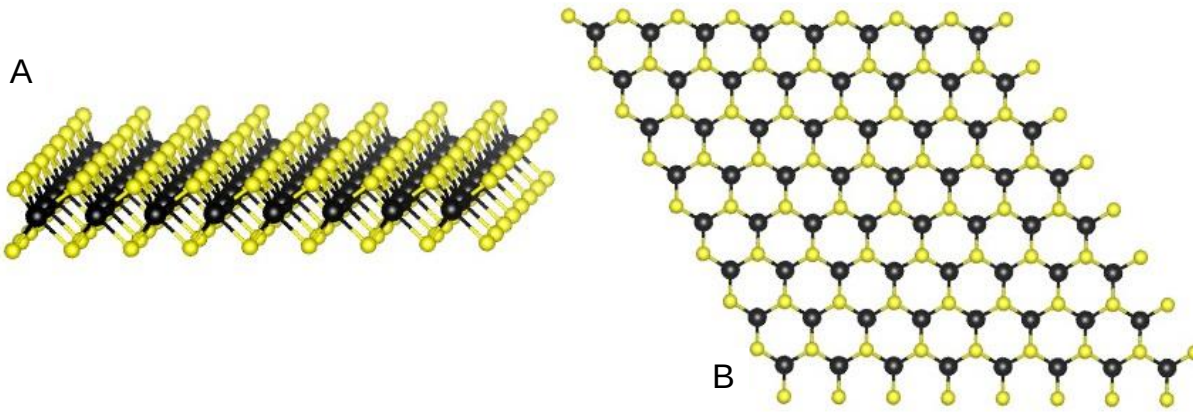

Figure 2.3. Crystal structure of MX_2. (A) Side view. The black atoms represent transition metal atoms; the yellow atoms represent chalcogen atoms. **(B)** Top view. The atoms form honeycomb lattice, similar to graphene. However, A and B sites are occupied by transition metal atoms and chalcogen atoms respectively, which break inversion symmetry.

Shown in Figure 2.2B there are two inequivalent points K and K' (or $\pm$K), which are known as Dirac Points. They are also known as "valley", which usually refers to the local minima in the band structure. Due to the unique cone shape structure at the valley, near the charge neutral point, graphene exhibits electron-hole degeneracy and vanishing carrier mass.

Rich physics uncovered in graphene suggest that new properties emerge when a bulk crystal is thinned down to monolayer. These cheering results paved the way for upcoming researches on 2d materials. It vastly accelerated the discovery of other 2d materials, such as transition metal dichalcogenides.

2.2 Transition Metal Dichalcogenides

Transition metal dichalcogenides are semiconductors usually referred to as MX_2, with M a transition metal atom (M, Mo, etc) and X a chalcogen atom (Se, S, Te, etc). A single layer (monolayer) of MX_2 consists of a plane of M atoms sandwiched between two X layers. The bulk crystal consists of repeated single layers with 2H-stacking—each successive layer is rotated by

180 degrees with alternative M and X atoms in the vertical direction. These layers are held together by van der Waals force.

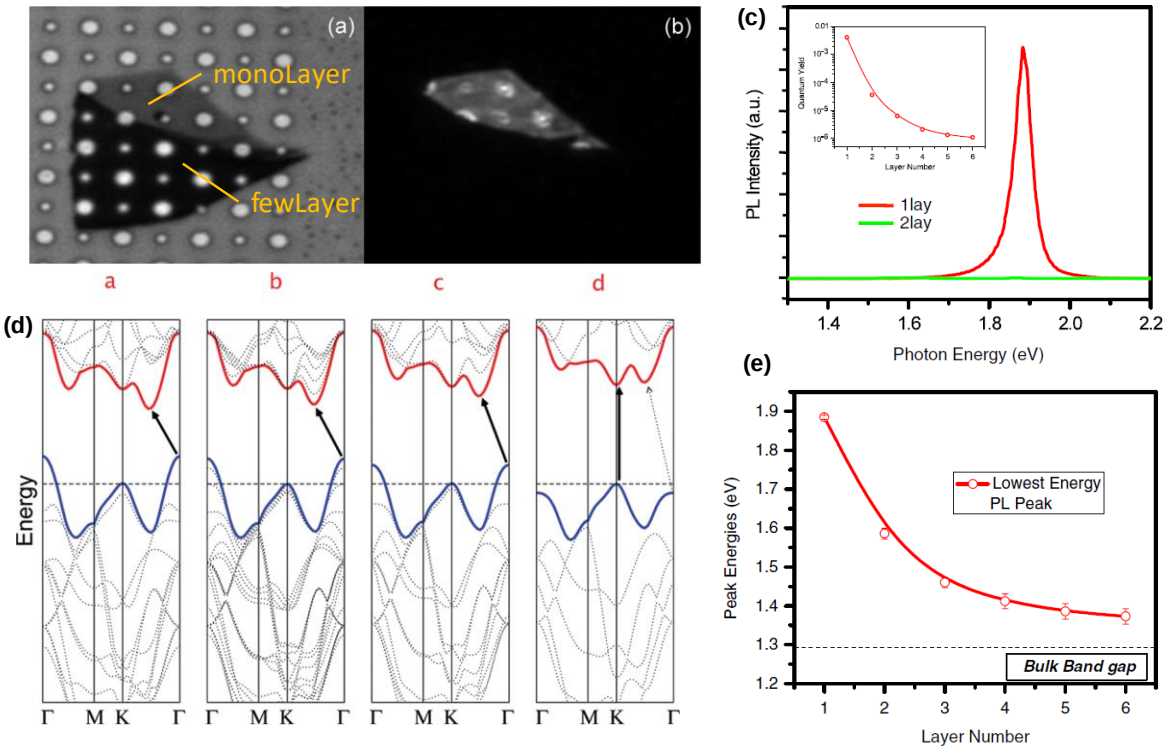

Figure 2.4. Layer dependent photoluminescence of MoS_2. **(a)** optical micrograph of mono and fewlayer MoS_2 on substrate with etched holes. **(b)** photoluminescence (PL) image over the same samples. The PL QY for monolayer region is much higher than the fewlayer region, which is too weak to be seen in the image. **(c)** PL spectra for monolayer and bilayer MoS_2. Inset, PL QY of thin layer for N=1~6. **(d)** Calculated band structures of bulk (panel a), quad (panel b), bilayer (panel c), monolayer (panel d) MoS_2. The black arrow indicates the lowest energy transition. **(e)** The lowest energy peak for 1-6 layers. The figure is reproduced from Mak, K.F., et al., Atomically Thin MoS_2: A New Direct-Gap Semiconductor. Physical Review Letters, 2010. 105(13): p. 136805. and Splendiani, A., et al., Emerging Photoluminescence in Monolayer MoS2. Nano Letters, 2010. 10(4): p. 1271-1275.

Before monolayer TMDs attracted substantial attention from researchers, they were no stranger to the industry. The layered structure makes the interlayer bond weak under sheer force. For this reason, it's been long used as a dry lubricant. In the year 2010, enlightened by single layer fabrication of graphene, the single layer MoS_2 was fabricated and measured [5, 10, 11]. It was reported that as the layer number of sample decreases, the experiments revealed a progressive

confinement-induced shift in the bandgap, the indirect gap 1.29 eV in bulk to 1.90eV in monolayer. The indirect gap to direct gap crossover happens in the monolayer limit. In addition, the photoluminescence (PL) quantum yield showed a dramatic enhancement, by more than a factor of 10^4. This effect is readily visible in a comparison between microscopic image and PL image, As shown in Figure 2.4(a) and (b), where we see bright PL from monolayer region meanwhile PL for the bulk region is negligible. In Figure 2.4(c), The PL spectrum for monolayer is shown. In Figure 2.4 (d), simulated bandstructure explicitly show that a bandgap enlargement from bulk to monolayer, meanwhile crossover from indirect bandgap to direct bandgap. Corroborating the simulation result, Figure 2.4 (e) shows the lowest absorption peak energy measured for different thickness.

Besides finite bandgap, a major difference between MX_2 and graphene is that MX_2 has large spin-orbit coupling (SOC). As illustrated for graphene, the existence of the inversion center in graphene dictates that SOC vanishes in graphene. On the contrary, in MX_2, the A site and B site are occupied by M atoms and X atoms, hence the inversion symmetry is broken. In MX_2, spin-orbits splitting amount to hundreds of meV in the valence band and a few meV in the conduction band (as shown in Table 2.1). The high SOC in MX_2 makes it well suited for spintronics and valleytronics applications, which will be illustrated with detail below.

In monolayer TMDs, the conduction band states at ±K valley mainly consist of d_{z^2} orbitals with the magnetic quantum number $m=0$; the valence band states at ±K valley consist of $d_{x^2-y^2} \pm i d_{xy}$ orbitals with $m=\pm 2$. For the conduction states, the dominant d_{z^2} component does not contribute to SOC, but the small components from d_{xy}, d_{yz} and the chalcogen p_x and p_y orbitals give rise to a finite spin splitting. Therefore, the magnitude of conduction SOC in the conduction band is much smaller than that of the valence band[12]. In Table 2.1, we present a theoretical calculation on the

energy of SOC for 5 TMDs. It should be noted that this conduction band splitting has an overall sign change between WX_2 and MoX_2.

Table 2.1. Theoretical energy of the spin-orbit coupling

	Valence band splitting (eV)	Conduction band splitting (eV)
MoS_2	0.148	0.003
WS_2	0.430	0.026
$MoSe_2$	0.184	0.007
WSe_2	0.466	0.038
$MoTe_2$	0.219	0.034

2.3 VALLEY AND VALLEYTRONICS

The use of electron freedom as an information carrier has been building our information era. In Field Effect Transistors (FET) and Charge Coupled Device (CCD), the two states, conducting state and non-conducting states, are used for storing information, which essentially uses electron charge as an information carrier. In the Magnetic Random Access Memory (MEMS) and Hard Disk Drive (HDD), spin up or down states for magnetic domains effectively use spin as an information carrier. In 2006, the use of valley as potential information carrier was first proposed in the study of conventional semiconductors such as AlAs and Si[13]. Later, in van der Waals materials, both graphene and TMDs are found to possess inequivalent valleys that constitute a binary index for low energy carriers (both electron or hole). Inherently, the valley can be a reliable information carrier because of the large valley separation in the momentum space. Therefore, it is robust against smooth deformation and low energy phonons. In addition, the large spin-orbit coupling creates spin valley locking effect, as well as a spin-flip barrier for intervalley scattering. In this section, we will discuss a couple of important properties associated with valleys. These facts demonstrate

that why valley index is a versatile, addressable, promising concept, and why TMDs is great candidates for valleytronics applications.

It will be instructive to make some general asymmetry analysis. Let's consider a valley contrasting property—magnetic moment $m_v = \chi\tau_z$. Where $\tau_z = \pm 1$ is the valley index and χ is a coefficient characterizing the material. Under time reversal transformation, both m_v and χ changes sign, then we reach that χ can be nonzero even if the system is nonmagnetic. Under spatial inversion, only τ_z changes sign. As a consequence, m_v can be nonzero only in systems with broken inversion symmetry.

The above analysis is true for any properties that hold the odd parity under time reversal transformation and even parity under spatial inversion transformation. One important example that falls into this scope of the rule is berry curvature. A nonzero berry curvature endows a material plenty of fantastic properties. As an example, berry curvature enters the electron's equation of motion:

$$\begin{aligned} \hbar\dot{k} &= eE + e\boldsymbol{v}(k)\times B \\ \dot{\boldsymbol{v}}(k) &= \frac{1}{\hbar}\frac{\partial \text{ò}(k)}{\partial k} + \dot{k}\times\Omega(k) \end{aligned}, \tag{2.1}$$

where Ω is the Berry curvature density and v is the group velocity of Bloch electrons. It is straightforward to see that the berry curvature acts as an effective magnetic field, which gives rise to an anomalous velocity. Note that the berry curvature is a valley contrasting property, thus the anomalous velocity leads to spatial separation of the carriers with opposite valley index, generating a net valley current. This effect lay the foundation of realization of valley hall effect in many valleytronics devices.

2.3.1 *Valley Optical Selection Rule*

If one inspects on the optical bandgap of four representative monolayer TMDs -- WSe_2, $MoSe_2$ MoS_2 WS_2, one could see that they all fall into an easily accessible wavelength range. It makes TMDs not only useful in making electric devices but also versatile in optical applications. In this section, we will present further an important property on TMDs—the optical selection rule[14-16].

It is worth noting that the optical selection rule based on valley physics was first suggested theoretical in 2008[17], which was discussed in the graphene system without valley inversion symmetry, such as being broken by substrate with inequivalent sublattice. However, it's experimentally hard to realize since the band gap of symmetry broken graphene usually falls in the mid-infrared region. It is until the rise of TMDs when people found TMDs to be a better candidate for optimal bandgap size and optical selection rule.

Unlike in atoms, optical selection rules are determined by orbital magnetic moments of the atomic levels. Optical selection rule in hexagonal lattice 2d materials has an entirely different origin. In addition to the intracellular current circulation of the parent atomic orbits, the orbital magnetic moment of Bloch electrons has a contribution from intercellular current circulation governed by bulk symmetry properties. In the following, we will explain this effect with a clearer physical picture.

In the system we consider, the intercellular circulation current from the parent atomic orbit can be assumed absent[17]. We first consider the orbital magnetic moment. Its contribution is now primarily from the intercellular current circulation, which gives:

$$\boldsymbol{m}(k) = -i\frac{e\hbar}{2m_e^{\,2}}\sum_{i\neq c}^{i}\frac{\mathbf{P}^{ci}(\boldsymbol{k})\times\mathbf{P}^{ic}(\boldsymbol{k})}{\varepsilon_i(\boldsymbol{k})-\varepsilon_c(\boldsymbol{k})}, \tag{2.2}$$

where $\mathrm{P}_{\alpha}^{ci}(k) = \langle u_{c,k} | \hat{p}_{\alpha} | u_{i,k} \rangle$ are the interband matrix elements of the canonical momentum operator. $\varepsilon_i(k)$ is the band dispersion. $|u_{i,k}\rangle$ is the periodical part of the Bloch wavefunction.

Now let's consider the simplest situation of a two-band model. The projection of $\boldsymbol{m}(\boldsymbol{k})$ along the light propagation direction $\hat{\boldsymbol{z}}$ can be expressed as:

$$-2\frac{\boldsymbol{m}(\boldsymbol{k})\cdot\hat{\boldsymbol{z}}}{\mu_B} = \frac{|\mathrm{P}_{+}(\boldsymbol{k})|^2 - |\mathrm{P}_{-}(\boldsymbol{k})|^2}{m_e[\varepsilon_c(\boldsymbol{k}) - \varepsilon_v(\boldsymbol{k})]}, \tag{2.3}$$

where $\mathrm{P}_{\pm} = \mathrm{P}_x^{cv} \pm i\mathrm{P}_y^{cv}$ and $\mu_B \equiv \frac{e\hbar}{2m_e}$ is the Bohr magneton. Furthermore, with the equality for the polarization averaged oscillator strength, we have

$$\frac{|\mathrm{P}_{+}(\boldsymbol{k})|^2 + |\mathrm{P}_{-}(\boldsymbol{k})|^2}{2m_e[\varepsilon_c(\boldsymbol{k}) - \varepsilon_v(\boldsymbol{k})]} = m_e \mathrm{Tr}\left[\frac{1}{2}\frac{\partial^2\varepsilon_c(\boldsymbol{k})}{\hbar^2\partial k_\alpha \partial k_\beta}\right]. \tag{2.4}$$

Hence we find, the circular polarization of interband transition,

$$\eta(\boldsymbol{k}) \equiv \frac{|\mathrm{P}_{+}(\boldsymbol{k})|^2 - |\mathrm{P}_{-}(\boldsymbol{k})|^2}{|\mathrm{P}_{+}(\boldsymbol{k})|^2 + |\mathrm{P}_{-}(\boldsymbol{k})|^2} = -\frac{\boldsymbol{m}(\boldsymbol{k})\cdot\hat{\boldsymbol{z}}}{\mu_B^{*}(\boldsymbol{k})}, \tag{2.5}$$

where $\mu_B^*(\boldsymbol{k})$ is the effective Bohn magneton with bare electron mass replaced by the isotropic part of the effective mass. This equation builds up a straightforward relation between the polarization of light and magnetic orbital momentum. The latter, as we discussed, has odd parity under time reversal symmetry and even parity under inversion symmetry. The lack of inversion center in monolayer TMDs satisfies the necessary condition for possessing a nonzero magnetic

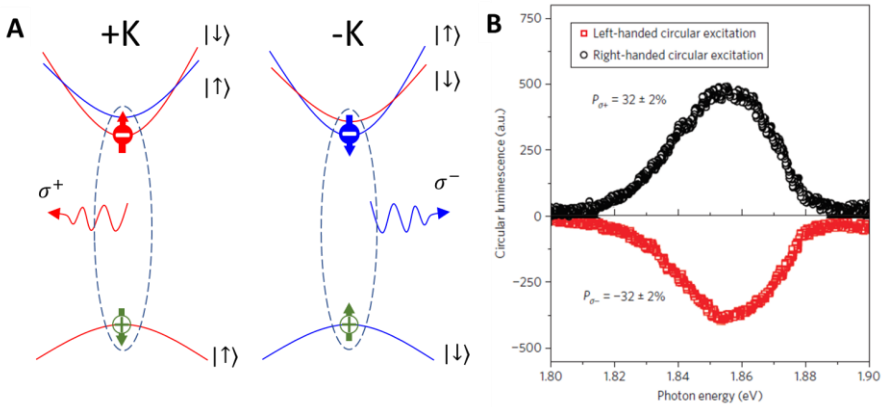

Figure 2.5. Optical selection rule of WSe_2. (A) schmatics of optical valley selection rule in MoS_2 **(B)** Circularly polarized photoluminescence spectra under 1.96eV excitation. 32% polarization is observed for both left and right circular polarized excitation. Figure reproduced from Zeng, H., et al., Valley polarization in MoS2 monolayers by optical pumping. Nature Nanotechnology, 2012. 7: p. 490.

moment, thus nonzero circular polarization.

In Figure 2.5A, we illustrate of valley optical selection rule in both valleys: the +K and -K valley are respectively coupled to σ^+ and σ^- light. Experimentally, it is found that the PL has the same helicity in its circularly polarized component as the excitation laser, as shown in Figure 2.5B The implication to the experiment in significant[15]. Not only it provides a pathway to control the population of electrons and holes in designated valley exciting the system with circularly polarized light, but it also provides a method to probe the population of excited electrons and holes by detecting PL that it emits.

2.3.2 *Valley Hall Effect*

The Hall Effect is a production of voltage across an electrical current carrying sample, in the direction transverse to the electric current and the external magnetic field, discovered by Edwin Hall in 1879. the Spin Hall Effect, where a spin accumulation of an electric current carrying sample is first experimentally demonstrated by Bakun et al in 1984 [18]; since the valley has been proposed as an important electron degree of freedom, there had been intense interesting in achieving Valley Hall Effect, which provides a new and standard pathway to achieve valleytronics. It was first experimentally demonstrated in 2012 in a monolayer TMD -- MoS_2 [19].

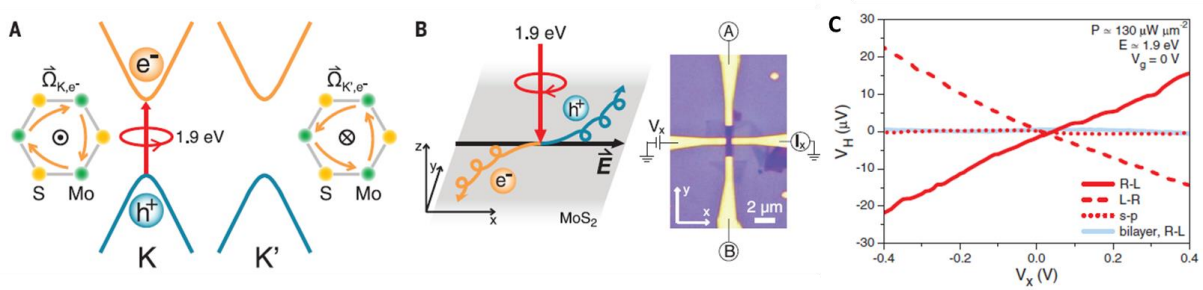

Figure 2.6. schematic of valley hall effect. (A) schematics of valley optical selection rule and the electrons at K and K' valley possess opposite berry curvature. The orange arrow represents clockwise and counterclockwise motion of electrons. **(B)** The schematics of photoinduced valley Hall current; and on the right is the image of the Hall bar device. **(C)** Hall voltage dependent on source drain bias. The R-L and L-R correspond to out of phase modulation and in phase modulation between PEM phase and lock-in amplifier. Figure reproduced from Mak, K.F., et al., The valley Hall effect in MoS2 transistors. 2014. 344(6191): p. 1489-1492.

To apply longitudinal voltage meanwhile measure transverse Hall voltage, the MoS_2 was patterned into Hall bar geometry. Thank to berry curvature, when semiconductor channel is biased, electrons from different valleys experience opposite Lorentz-like forces so that they move in opposite directions that are perpendicular to the drift current. Meanwhile, under time reversal symmetry, an equal amount of Hall current from each valley flow toward opposite directions so that no net Hall current can be detected. To resolve the situation, circularly polarized light is used to break time reversal symmetry, which means two valleys are unequally populated. Therefore, under a finite bias, both photoconduction and a net transverse Hall voltage are detected, and the

sign of the Hall voltage is connected to the helicity of the incident laser. In experiment, photoelastic modulator (PEM) is used to modulate the retardance at 45 degrees off the incident linear polarization, creating alternating left circular and right circular light. The Hall voltage is accordingly sent through lock-in amplifier for spectrum analysis. In Figure 2.6C, a positive Hall voltage under R-L modulation is observed, which is consistent with prediction. The sign of the signal is reversed when it is changed to L-R modulation.

The VHE in is a demonstration that lack of inversion center in TMDs makes valley degrees of free highly accessible, In graphene, extra technical practices are needed for realizing for similar phenomena. We refer to the interested reader that the same effect, in graphene, was first reported in 2014 by breaking the inversion symmetry with graphene/hBN superlattice[20].

2.4 Excitonic Properties

In semiconductors, when an electron is excited to its excited state, it leaves behind a quasiparticle, hole, that holds a positive charge on the valence band. Then the coulomb force kicks in, binding the electron and hole together, forming an excited state of solid state—exciton.

Some materials have relatively small dielectric constant, hence the Coulomb interaction between an electron and hole may be strong and the exciton tend to be small, which is on the same order or less than a unit cell. This kind of exciton is named Frenkel exciton, named after Yakov Frenkel. Frenkel excitons are typically found in alkali halide crystals and organic molecular crystals composed of aromatic molecules. In Chapter 9 we will be presenting my work on Chromium Triiodide (CrI_3), in which Frenkel exciton is generated by optical exciton.

In a lot of more other semiconductors, the dielectric constant is large. Consequently, electric field screening tends to reduce the Coulomb interaction between electrons and holes, resulting in a Wannier Exciton. Wannier exciton has a radius larger than the lattice spacing. A direct

consequence is that the effect of the lattice potential can be incorporated into the effective masses of the electron and hole. Likewise, although is mimic a hydrogen system, the screening causes the binding energy to be much less that of a hydrogen atom, typically on the order of 0.01eV.

Exciton in TMDs falls into the scope of Wannier exciton. However, it is very special if compared to typical Wannier excitons. On the one hand, the Coulomb interaction between electrons and holes are exceptionally strong, due to the two-dimensional geometry and the large effective mass, as a result, the binding energy is comparable to typical Frenkel exciton; On the other hand, the wavefunction is still largely of Wannier – Mott type, with the electron-hole relative motion extends over tens of unit cells.

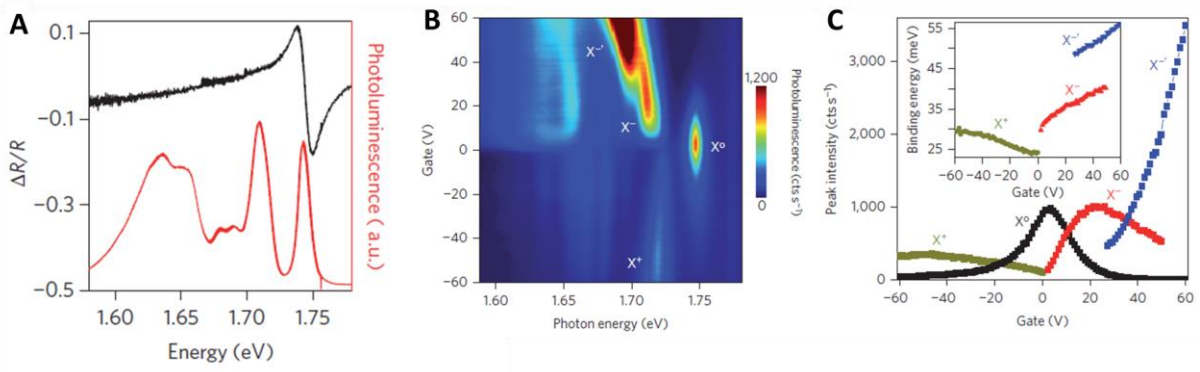

Figure 2.7. Photoluminescence of WSe_2 in response to carrier doping. (A) Red: Photoluminescence at charge neutral point. The emission at 1.74eV and 1.71eV are attributed to exciton and trion, respectively. Black: differential reflection spectra, strong resonance at exciton energy is observed. **(B)** The gate dependent photoluminescence spectrum. Photon energy shows neutral exciton (X^0), negative trion (X^-) and its fine structure ($X^{-\prime}$) and positive trion states (X^+). **(C)** Peak intensity of four peaks as function of gate voltage. Inset: binding energy as function of gate voltage.

In this chapter, we take WSe_2 as an example of TMDs, focusing on discussing excitonic emission in WSe_2 [21]. This purposed arrangement is for better cooperating with the WSe_2/CrI_3 heterostructure content in the next few chapters.

Figure 2.7A plots the photoluminescence and differential reflection spectrum of monolayer WSe_2 taken at 30K, without externally tuning the doping level. The strong excitonic resonance in the differential spectrum at ~1.74meV marks the exciton energy, in agreement with the 1.74meV

photoluminescence emission peak. The second featured peak on the lower side of exciton emission is the trion emission, which is at around 1.71meV. More peaks are shown on the lower energy side of trion. They come from phonon sidebands and defects.

This picture is well supported by gate dependent measurement. In Figure 2.7B, the same device is measured after adding gate. Four featured peaks are revealed in the map: neutral exciton (X^o), negative trion (X^-) and its fine structure ($X^{-\prime}$) and positive trion states (X^+). The exciton emission prevails near charge neutral, meanwhile the trion peak X^- (X^+) dominates with electron (hole) doping. At high electron doping, the trion peak is replaced by the $X^{-\prime}$ peak, which is trion with a different fine structure[21].

In Figure 2.7C we see the intensity and peak position of respective peaks extracted from Figure 2.7B. Both X^- and X^+ falls on the lower energy side of X^o. The energy discrepancy is called "trion charging energy", which refers to the energy difference between $X^\pm$ and the unbound state of an X^o plus a free electron or hole. For X^-, it is 30~40meV, depending on gating; for X^+, it is 24~30meV.

Another similar concept is the binding energy. It is defined as exciton energy compare to the free electron-hole pair. However, the direct determination of E_b has not been possible, as the edge of band-to-band transition has not been unambiguously determined. The most successful approach for extracting the number is by doing scanning tunneling spectroscopy (STS) grown on HOPG graphene. It shows a quasiparticle band gap of 2.51eV at 77K for WSe_2. If compared to WSe_2 excitonic resonance at room temperature (~1.65eV), it leads to E_b ~0.86eV.

One could see that both charging energy and binding energy are very large if compared to other quasi two-dimensional systems, such as quantum wells. It is a result of the two-dimensional nature and large effective mass of the carriers[22, 23]. These facts endow a stable exciton and trion states

even at room temperature. This aspect has attracted many research interests recently to realize excitonic devices at room temperature. [10, 24].

2.5 Magnetic Control of Valley Properties

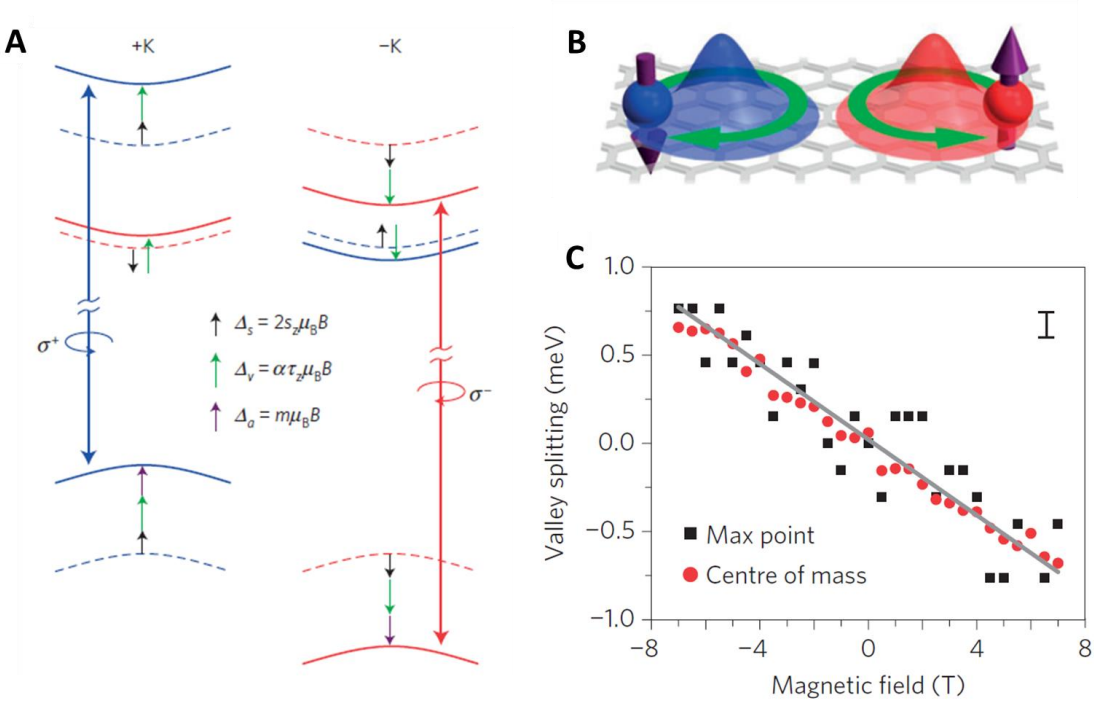

Figure 2.8. Zeeman splitting of valley pseudospin in WSe_2. (A) Three contributions to Valley Zeeman effect: Spin magnetic moment, the orbital magnetic moment, and the valley magnetic moment (from berry curvature). **(B)** A cartoon depicting the origin of valley magnetic moment. The blue (red) wavepacket with spin down (up) in +K (−K) valley self-rotates in clockwise (counter-clockwise) direction, which give rise to valley magnetic moment. **(C)** Extracted Zeeman splitting as function of magnetic field. Two different methods are used to ensure validity for peak position extraction. The figure is reproduced from Aivazian, G., et al., Magnetic control of valley pseudospin in monolayer WSe2. Nature Physics, 2015. 11: p. 148.

By discussion above, we have reached a consensus: If a system preserves both inversion symmetry and time reversal symmetry, such as pristine graphene, the orbital magnetic moment, berry curvature and optical helicity vanishes. While if a system has no inversion center but preserves time-reversal symmetry, the orbital magnetic moment, berry curvature and optical helicity can be non-zero. Meanwhile, Kramer's theorem indicates that for every state at +K valley, there is Kramer's pair state at −K valley with opposite spin and degenerate energy. Therefore, the optical bandgap for two valleys must be degenerate. For many valleytronics application, we would like to

achieve one step further. Such as, can we break the valley degeneracy such that the valleys information can be read out by emission energy? Can we tune the transition energy?

Symmetry analysis immediately suggests that to break the valley degeneracy, one needs to break time reversal symmetry. In section, we will talk about the Zeeman effect in monolayer WSe_2.

The orbital magnetic moment has two parts: a contribution from parent atomic orbital, and a valley magnetic moment contribution from the lattice structure, which is relative to berry curvature.

The overall Zeeman shift has three contributions[25]. The spin magnetic moment, the orbital magnetic moment, and the valley magnetic moment, as shown in Figure 2.8A. The spin magnetic moment shifts the band up by $\Delta_s = 2s_z\mu_B B$, where s_z is the spin direction of the band. However, it should be noted that the optical valley selection rule suggests that the spin of the initial and final states are the same. Hence the effects on the initial and final state are the same. The atomic orbital contribution, however, does affect them because the conduction bands are composed of d orbitals with $m = 0$, and the valences are composed of d orbitals with $m = 2$ in the +K valley and $m = -2$ in the −K valley. The total effect increases the optical resonance energy by $-2\mu_B B$ in the +K valley and $2\mu_B B$ in the −K valley, creating net $-4\mu_B B$ energy splitting. The third effect is the valley magnetic moment effect. The valley magnetic moment originates from the berry curvature induced self-rotation of the wavepacket, as shown in Figure 2.8B.

All the three effects, as shown above, are proportional to magnetic field B. Thus the expected total effects are expected to be linear with B. Experimentally, a mechanically fabricated device was measured in the out-of-plane magnetic field in 30K. The sample was excited and detected by a single helicity of light, and one can determine the valley splitting by comparing peak position for different polarizations.

In Figure 2.8C, we present the measurement result. Two different methods are used to extract the peak position to ensure the validity of the data, and they agree pretty well. As indicated by the gray line, an apparent linear relation between valley splitting and magnetic field is observed, with a slope of $(-1.9 \pm 0.2)\mu_B$.

Chapter 3. FABRICATION OF VAN DER WAALS MATERIALS

In 2004 Andrei et al [1] proposed a simple method to fabricate graphite down to ~0.7nm thick—using Scotch tapes. A story from my group four years ago is a vivid demonstration of how unbelievably simple it is to implement this method. At that time, a postdoc from our group was about to graduate, another colleague gifted him with a scotch tape and a batch of graphite pencil core, "when you miss us, you can fabricate some graphene by yourself." Of course, that's not the stand setup to fabricate graphene in the lab, yet it's a vivid demonstration how easily it is to get hands on fabricating graphene, the thing that won Andre a Nobel prize. In fact, writing with a pencil on a piece a paper is effectively producing massive graphene sheets. The simpleness of mechanical fabrication has always been reminding me that huge discoveries in science are just right there for one to discover with the right spirit.

3.1 MECHANICAL FABRICATION

There are two major types of methods to obtain 2d materials. The first one is the physical or chemical vapor transportation (PVD or CVD), which typically involves the heating of the proportionally mixed precursors upstream of a tube furnace, in the center of which places target substrate. The furnace is then heated at target temperature for days, when the stream of the flowing gas carries the constituent materials through the tube, part of which will condense on the substrate, nucleating and grow epitaxially. Some growth methods have requirements on the substrate material. For growing graphene, it was shown that the graphene grows primarily in registry with the underlying copper lattice for both Cu(111) and Cu(100)[26]. The merit of CVD growth is that it can reach to large size, and large substrate coverage ratio.

The quality is the main drawbacks of CVD growth. First, it's sensitive to substrate imperfections, such as grain boundaries, or thickness variations. [26]. Second, the thickness uniformity is hard to control, and thicker islands could form on top of monolayers. Third, point defects, or line defects are abundant. Fourth, the difference in thermal expansion coefficient between the substrate material and the grown material could lead to large strain [27];

Under high requirement for sample quality, for all the devices fabricated in this thesis, we use mechanical fabrication. This includes fabrication of hBN, graphene, WSe_2, CrI_3, and many other Van der Waals crystal that can also be fabricated down to few or monolayer with this method.

To start off the fabrication process, first we need to get the substrates ready. Two types of substrates are most frequently used. The 300nm SiO_2/Si substrate and the 90nm SiO_2/Si substrate. These two types are designed for fast and reliable identification of layer thickness by optical contrast[28]. The incident light reflects off the sample surface, sample/SiO_2 interface, and the SiO2/Si interface, causing interference. Some wavelengths are constructively strengthened in the reflected light, and some are destructively weakened. Therefore, the color of reflected light reveals their layer thickness, which then can be read out by a microscope. With a little experience, one could quickly learn to identify layer thickness with a microscope and start to search for monolayers. I personally find that for searching hBN, CrI_3 90nm SiO2/Si provides slightly better contrast and searching for TMDs and graphene is better with 300nm SiO_2/Si. It is also possible to use other substrates if one has particular reasons for doing so. For example, fabricating onto PDMS has a slightly better yield than SiO_2, and it provides a quick option to transfer onto another substrate, by gently pressing PDMS against it; Au is also occasionally used for fabricating materials that do not adhere to SiO_2. It also fabricates enormous TMDs. However, they adhere so strongly that they cannot then be removed.

The long-exposed wafers are usually covered with micro-contaminates, and the surface becomes inert and non-adhesive. The reactivation of the surface is necessary for high yield fabrication. Therefore, after cutting the wafer to desired size (~1.5cm×3cm), we soak it into aceton for 5 minutes. This process removes oils and organic residues. However, aceton itself do leave residue on the surface of the wafer as well. In a standard procedure, after the aceton bath, the wafer is quickly transferred into a beaker of isopropanol for another 5 minutes, during the transfer, it is critical to constantly spray isopropanol over the surface to prevent aceton from drying out. Once the time is up, remove the wafer from the isopropanol beaker and blow dry the wafer with a nitrogen gun. Then, we oxygen plasma the surface with 50W for 5 minutes to refresh its surface[29]. Finally the wafer is ready for fabrication.

The next step is to cleave the crystal. A few bulk crystals are carefully placed on a scotch type ~4cm long. The tape is gently bent over to touch the crystal, then retracted to cleave the bulk crystal into two. This process is repeated for 5~6 times. It is beneficial to avoid crushing crystals on one wing of the tape against crystal on the other wing, which results in shredding crystal into small pieces. It is a misconception to use as little crystal as possible from the start, in the hope of getting more thinner flakes after cleavage. On the contrary, the monolayers are more often found peeling off a large bulk crystal. Therefore, peeling off the tape too many times shreds all the crystal into tiny pieces, which is actually detrimental to achieve better exfoliation.

In the next step the tape is placed onto the wafer with the sticky side down, followed by gently rubbing against the back of tape with a rubber. This is to squeeze out the airs and achieve smooth contact between the tape and substrate. Rubbing too hard, again, will shred the crystals hence is not recommended. The wafer is then baked on a hotplate for ~5minutes. The temperature setting is dependent on the crystal. I would recommend 120 °C for TMDs and 90 °C for hBN and CrI_3.

After removing the ensemble from the hotplate, wait for it to cool down to room temperature again. The tape is then slowly peeled away from the substrate, leaving off a large amount of crystal flakes on the substrate to be searched with. Note that materials that are air sensitive must be kept in glovebox. Therefore, the same operation can be carried out inside the glovebox with gloves.

Once the substrate is ready, it is then placed under the microscope for searching. The thicknesses are immediately distinguishable by flake colors. The choice of magnification is important. Too large a magnification slows down the process significantly, while too low a magnification could leave quality flakes unnoticed. A typical size of TMD (hBN) flake is around 10μm (50μm), I usually search then with 20x objective lens to ensure both speed and accuracy. For graphene flakes, the size is typically larger. In certain situations, it can be searched with 5x objective lens to start with and then switch to 20x for a second inspection. Once a desired flake is located, I would gently make a scratch from several hundreds of μm away for location mark. The distance shouldn't be too close so that the SiO_2 dust particles might fly over which causes contamination. Finally, I take one picture with each of the 100x, 20x, 5x objective lenses, during which I ensure that the 5x picture includes both the location marker and the flake.

It has become a general practice to examine the flake with Atomic Force Microscopy (AFM) before adding it into your "qualified sample pools". Doing AFM serves two purposes: 1. To confirm the thickness of the flake, as judging by color is subjective, which can be biased by personal experiences. In addition, the thickness may vary within the interested region. Such case is especially harder to spot by eye when you are aiming at a piece that is more than a few nanometers thick. If a non-uniform thickness is detected, the safest measure is to dump this one and find another, or you could mark the portion that is uniform in thickness and only use that part for your heterostructure. 2. To examine the cleanliness of the sample. This procedure is aimed at

identifying tape residue, which is introduced during the cleavage of the crystal—a very common issue in mechanical fabrication. Not only it could impair the electronics and optical properties of the device, but it also makes damage the interface, making fabricating of robust heterostructure impossible. Unfortunately, tape residue cannot be effectively removed by aceton, isopropanol or other typical cleaning chemical solvents. The best solution is to find an alternative.

After all above is done. Congratulation, a nice beautiful piece could be added to your sample pool. Last, but not least, the sample should be carefully put away. Except for hBN and graphene, which is very stable in air, the samples should be preserved in inert atmosphere or vacuum for long-term storage. A vacuum-based desiccator or a glovebox are the most common options.

3.2 Transfer Technique

Since the discovery of graphene, more and more materials with various chemical composition are added to the 2d materials category. However, the diversity of the devices in theory is still limited by the number of crystals in this world that possess the van der Waals crystal structure. This situation has been entirely changed since the invention of transfer technique. By conducting these elaborate operations, the van der Waals materials can be stacked on top of the other, at a specific location with specific crystal orientation, forming heterostructures. This method provides numerous possibilities for the creation of new device designs. To provide an estimate, if a heterostructure is a stack of 2 species of van der Waals material, the possibility of design is the square of species number of van der Waals materials. If it is a stack of 3, the possibility is cubed. It could go on. The thickness of each component could also vary. Hence the possibility is practically endless. In other words, the invention of transfer technique greatly broadened the horizon of the van der Waals material world and endows this research field with countless

possibility. In this section, we will discuss the cutting-edge transfer technique that we employ in the Xu lab[30].

Before beginning transfer, one needs a blueprint for device architecture. The blueprint helps prevent the occurrence of several issues that could be detrimental to the transfer. The blueprint can be drawn with the help of specialized software, such as Klayout. To do this, the images of each flake first are imported into the software. The images are imported to be proportionally presented with respect to the real flake size. Then one could virtually stack them for the preview of transfer result. During the process, one could tune the relative position and angle between flakes for the best result. In certain designs, the crystal axes are also required to be aligned, which can be fulfilled in the software as well. During the designing of alignment, these issues should be taken into consideration: 1. Make sure that the heterostructure area matches the contact that is prepared (if there is). 2. Compare the relative size of each flake, consider the overlapping relations between flakes. For example, in cases where hBN is used for encapsulation, the hBN should be covering the encapsulated flake in any dimension. 3. Pay attention to surrounding flakes that are particularly close. For example, an irrelevant bulk WSe_2 in the vicinity of targeted the monolayer WSe_2 could lead to failure of good encapsulation.

To transfer one material onto another, a stamp is needed for temporarily holding up the transferred materials and placing it onto the second one. In addition to the adhesion of the targeted flake, it also requires the ability to retract and detach from the original piece of material once the stacking is done. A Polycarbonate (PC) membrane fits the goal. First, it sticks to the Van der Waals material at a certain temperature, allowing it to pick the flake that is to be transferred; Second, it undergoes a glass transition at 147 °C, at which temperature it detaches from the stamp easily, separating the

glass phase PC and the transferred flakes from the original stamp. The PC can be then washed away by chloroform cleanly.

A functional stamp is made up of four components: A glass slide, a PMDS cube, PC membrane, and some tapes that hold them together. The glass slide is the backbone, which holds up everything and installs on the micromanipulator. The PMDS serves to support the PC membrane from the back, which gives the PC membrane the curvature desired.

The PMDS are usually cut into two types of shapes: the dome-shaped PDMS and cube-shaped PDMS. The dome-shaped provides larger curvature to the pc membrane, which means a larger contact angle between the stamp and the substrate. A direct consequence is that when it is pressed against the substrate, the boundary of the contacting area advances more smoothly. This helps firmly push out bubbles between the HS, yielding less bubble. However, it also comes with serious drawbacks: It exerts a larger force against the substrate, due to the large contact angle. It causes two issues. First, it introduces large strain in the resulting HS, which is preserved even after the PC is washed away. The residual strain could have a drastic effect on the optical and electronic properties of the device. Second, heated flakes during transfer are highly mobile, the pressure could lead unpredictable in plane movements of individual flakes, destroying the architecture of the heterostructure. Due to these reasons, I personally prefer cubed PMDS.

The PMDS cube is prepared from Sylgard 184 Kit, with a 10:1 ratio. After mixing two components, the solution is poured into a beaker with a flat bottom, to a thickness of ~3mm. The beaker is placed in a vacuum chamber for 20min to eliminate the bubbles, which is next transferred into a 70°C oven, curing for ~2 days. A sharp blade is then used to cut the PDMS into 3mm*3mm*3mm cubes.

To make a PC thin film. A ~7% bisphenol-A polycarbonate (Alfa Aesar) is dissolved in chloroform. With a magnetic stirrer, in 2 days the dissolution should be complete. Then, prepare two clean glass slides, use a glass pipette to dispense PC solvent onto the glass slide. Now put the other glass slide over it, gently press and then slide them apart. Now a thin film of PC solvent should be formed over the first glass slide, which will dry within ~10min and be ready to use.

Then we can start assembling the stamp. Use a hole-punch to cut a ~8mm circle on double-sided tape and adhere to end a fresh glass slide. Now place a PDMS cube prepared above to the center of the circle. Then use the same hole-punch to cut a circle on a scotch tape, which is used to pick up the PC membrane. Now lay the scotch tape across the PC glass slide with the hole in the center. Use tweezers to gently push the scotch tape to ensure firm contact between PC and the scotch tape. Now cut the along the edge of the scotch tape to remove the attached PC membrane from the rest, which ends up with a PC membrane attached to the sticky side of scotch tape. The hole on the scotch tape is now sealed by PC. This is the core part of that is used for transferring. Carefully center and drape the scotch tape over the PDMS tape and press the side of scotch tape into contact with the double-sided tape. Again, use a tweezer to gently squeeze out the air ensuring a firm contact.

The transfer process in done on a transfer stage. A transfer stage has four functional parts: A heating stage (made of a chunk of aluminum) with center vacuum chuck hole, which controls the temperature of the substrate meanwhile hold it firm with the vacuum chuck; a micromanipulator that controls the movement of stamp in three dimensions; a microscope that provides vision, which is installed with long working distance objective lenses; a platform beneath the heating stage that allows movement in two horizontal directions and is free to rotate, which is responsible for angular and spatial alignment of the substrate. A handful of computer Software can be very helpful: a

software that accomplishes free drawing on the computer screen is need. Such as Epic Pen that I have been using, which is free and easy to use. One more software that accommodates image overlay is desired. There are plenty on the market that fulfills the requirement, such as Overlay2.

To begin the transfer process, a testing for the stamp quality is necessary. Find a wafer that has been fabricated once (so that the stickiness resembles the substrate that the stamp will be in contact with) such as the wafer of the first flake that will be used. Find a relatively clean area where the flakes are sparse, then install the stamp onto the micro-manipulator with the stamp facing down. Under the microscope, move the stamp to the center of view until one can look through the center of the PDMS cube and get a nice vision of the substrate. Set the thermal stage to 90 °C. Carefully lower the slide a little, use the microscope to focus on the substrate then on the stamp. Take the travel distance as an estimate for the distance between the stamp and the substrate. Repeat the process until they are very close. Newton's rings will show up signifying that touching is around the corner. Then carefully lower the stamp a little bit more until touching. When it touches, the contact region has a different color with respect to the rest so that it is very easy to tell. Translate the objective lens horizontally until the contact region is off the center by about ~200 μm . Use the epic pen to mark the contact center on the computer. Now it's good to gently retract the stamp from the substrate.

Delamination could happen during the retraction. when it happens, the contact region doesn't shrink as one raise the slide, and a clear layer of air can be seen, which means the stamp fails the test, usually caused by insufficient tension between the PC and PMDS. Now a remake of the stamp must be done meanwhile consider using a thicker PMDS or make sure there is firm adhesion between the PC and the double-sided tape.

If the stamp passes the test, now it's ready to pick the first flake. Translate the platform underneath to center desired flake in the view, rotate the substrate or the platform until the flake is in the desired orientation. Repeat the similar process in the stamp test to lower the glass slide until the touching happens. It should touch the same region that we have marked, which is 200 μm away from the center, where our flake is located. Next one needs to make the contact region expand until it covers the flake. There are two methods for doing it: raising the temperature of the heating stage, which will thermal expand to raise the substrate up; manually adjust the micro-manipulator to lower the glass slide. The former is preferred because the movement is way steadier than the latter, which heavily relies on the accuracy of micro-manipulator's movement and the operator's skill level, might not be reliable. The expansion of the thermal stage causes the rising of the substrate, which then causes the expansion of the contacting region. Eventually, the contacting boundary slowly crosses the flake, leading to a firm contact between the PC membrane and the target flake. Now the flake should be clearly visible, use the Epic Pen to plot the contour of the flake for later usage. To retract and release PC, reduce the set point of the temperature gradually, the reverse process will happen. Due to the strong Van der Waals force between the PC and the 2d material, the 2d material should now be attached to PC, coming off the substrate.

The subsequent pick-ups can be initiated following the same procedures. However, starting from the pick-up of the second flake, the alignment between flakes is now an important aspect of transfer. To do that, right before the PC come into contact with the substrate, the PC should be so close to the substrate that the PC and the substrate are loosely in the same focal plane, thus the flake on the PC and the flake to be pick-up are simultaneously imaged. To achieve precise positioning, using the ancillary software such overlay2 could be very helpful. Use the software to load and suspend the image of a targeted flake at a desired position, set the image to 50% transparent, then rotate

and translate the platform holding the flake until the flake overlap with the image. Triangulation with the flakes surrounding the target flake can also increase the rotational precision significantly. Once all except the last flake is assembled, it is ready to initiate the melting down process. Follow the same process as pick-ups, until the last piece is in contact with PC. However, this time, we would like to drop the whole stack of flakes on the substrate. Slowly increase the temperature, until the contacting boundary is away from the target flakes. Now keep steadily increasing the temperature while compensating the raise by the slowly raise up the glass slide, keep the contacting boundary stable. Beyond 147°C, the PC transit into the glass phase. Stay at 180°C for 5 minutes, then slowly retract the glass slide. At one point, the PDMS will detach from the PC, which is signified by a sudden brightness change over the contact region and tendrils can be seen around the contact region which is a consequence of tearing. Once this happens, keep retracting the glass slide until it's way above the substrate, which is then safe to be removed.

Once the transfer is finished, keep the substrate on the heating stage, letting the sample cool down to room temperature slowly. To remove the PC, soak the sample into the chloroform for ~10 hours and transfer into another fresh beaker of chloroform for another hour. Next, give it another bath in IPA for ~1 hour. When transferring it from one beaker to another, it is suggested to constantly squirting IPA over the sample, to prevent chloroform from drying which leaves a residue. Immediately after removing the sample from IPA, use the nitrogen gas gun to quickly dry the sample. Finally, take several microscope images and do AFM examination for evaluating the integrity and quality of the sample after the transfer for possible publication data.

Chapter 4. MAGNETIC HETEROSTRUCTURES

The exchange interaction is a central topic in this thesis. We will have a lot a discussion on the exchange interaction, such as exchange interaction between CrI_3 and WSe_2, magnetism in CrI_3, etc. Before diving into the content, we will use simple examples to illustrate how the interaction interaction occurs and how it gives rise to the magnetism.

Specifically, we will first see how classical theory exhibits difficulties in explaining the ferromagnetism, which leads to the theory of quantum origin—exchange interaction. Using a two-electron model, we demonstrate how the quantum original exchange interaction affects the electron location, and the coulomb interaction and thus the energy difference between different spin configurations. Then we will introduce an example on harvesting magnetism by building magnetic heterostructures. This is a work in analogy to our WSe_2/CrI_3 design realized in a thin film system in stead of van der Waals materials. During the writing of this chapter, the author read and reorganized some contents from the Ashcroft and Mermin's book[31].

4.1 THE ORIGIN OF FERROMAGNETISM

Ferromagnetism, represented by ferromagnetic materials, exhibits net magnetization without the presence of external magnetic field. If there were no interactions, discrete source of magnetic moment would be thermally disordered, pointing towards random directions, and would sum up to no net magnetic moment for the solid. Therefore, the net magnetization in a ferromagnet must be due to interaction.

4.1.1 *Estimation of dipolar interaction energy*

An immediate assumption is that the interaction arises from the magnetic interactions between the spins. Ether through magnetic dipole-dipole interactions, or through spin orbit coupling. However, magnetic interaction is not the dominant interaction.

We can estimate the direct dipolar interaction energy of two magnetic dipoles $\boldsymbol{m}_1$ and $\boldsymbol{m}_2$, separated by $\boldsymbol{r}$:

$$U = \frac{1}{r^3}[\boldsymbol{m}_1 \cdot \boldsymbol{m}_2 - 3(\boldsymbol{m}_1 \cdot \hat{\boldsymbol{r}})(\boldsymbol{m}_2 \cdot \hat{\boldsymbol{r}})]. \tag{4.1}$$

Atomic dipole moments are in the order of: $m_1 \approx m_2 \approx \frac{e\hbar}{mc}$. Plug it in, assuming two magnetic moments are in the sample plane oriented in the out-of-plane direction,

$$U \approx \frac{1}{r^3} \cdot (\frac{e\hbar}{mc})^2 = \frac{e^2\hbar^2}{r^3 m^2 c^2} = \frac{1}{137^2}(\frac{a_0}{r^3})\frac{1}{R_y}. \tag{4.2}$$

As a conservative estimation, in the atomic level, the magnetic moments are ~2Å apart. We got:

$$U \approx 1\times10^{-4}\,\text{eV}, \tag{4.3}$$

which is negligible compared with the electrostatic energy difference between the states. In fact, direct evidences could be provided by common ferromagnetic materials such as iron, cobalt, and nickel, which all have curie temperature of several hundreds of degree K. If the dipolar interaction causes the alignment of spins, one would expect the spin alignment to be thermally obliterated above a few degrees K. As a result, the magnetic moment dipole energy is not a dominant energy in determining the magnetism of the solid state.

It is also generally safe to rule out the spin-orbit coupling as a major source of magnetic energy. To understand this question, determining the magnetic moment of individual atoms is essential. Even in this case, however, in Hund Rules, the first two rules are purely determined by electrostatic

energy considerations, and only the third rule, giving the splitting between *LS*-multiplet is based on spin-orbit coupling.

Due to the above reasons, to a first approximation, many theories of magnetism ignore dipole-dipole interaction and spin-orbital coupling.

4.1.2 *Introduction to exchange interaction*

So that question is naturally asked that what is the real source of energy that is deterministic in magnetism? By far the most important source of magnetic interaction is a combination effect of electrostatic electron-electron interaction exchange interaction.

Exchange interaction is a quantum mechanical effect that has no classical analog. It only occurs between identical particles. It originates from the exchange symmetry of identical particles, both for Bosons and Fermions, which are symmetric and antisymmetric respectively. For Bosons, the exchange interaction exists in the form of attraction and can lead to Bose-Einstein Condensation. For Fermions, the exchange interaction exists in the form of repulsion which is sometimes called Pauli Repulsion.

Exchange interaction is also sometimes called exchange force but it’s a misconception to treat it as a true force since it lacks a force carrier. Its effect comes into play in the forms of requiring the wavefunction to comply with specific symmetry. The energy difference then arises as a consequence. In the following content, we will demonstrate how incorporating Pauli repulsion into a 2-electron system, even with spin independent Hamiltonian, leads to magnetic effects.

Heitler-London model is an important example for understanding the exchange interaction. Consider a two-electron system in a hydrogen molecule, as shown in Figure 4.1. with its Hamiltonian to be purely electrostatic, which is independent on spin. Therefore, the stationary

solution Ψ can be written as a product of coordinate wavefunction φ which satisfies Schrodinger's equation and a spin wavefunction. The former satisfies,

$$H\psi = -\frac{\hbar^2}{2m}(\nabla_1^{\,2} + \nabla_2^{\,2})\psi + V\psi = E\psi\,, \tag{4.4}$$

where

$$V = \frac{e^2}{4\pi\grave{o}_0}\left\{-\frac{1}{|\boldsymbol{r}_{a1}|} - \frac{1}{|\boldsymbol{r}_{b2}|} - \frac{1}{|\boldsymbol{r}_{b1}|} - \frac{1}{|\boldsymbol{r}_{a2}|} + \frac{1}{|\boldsymbol{r}_{12}|} + \frac{1}{|R_{ab}|}\right\} \tag{4.5}$$

is the electrostatic potential energy for the system. The protons are denoted by the letter a and b ; the electrons are denoted by the number 1 and 2. The vector $\boldsymbol{r}_{a1}$ denotes the vector pointing from

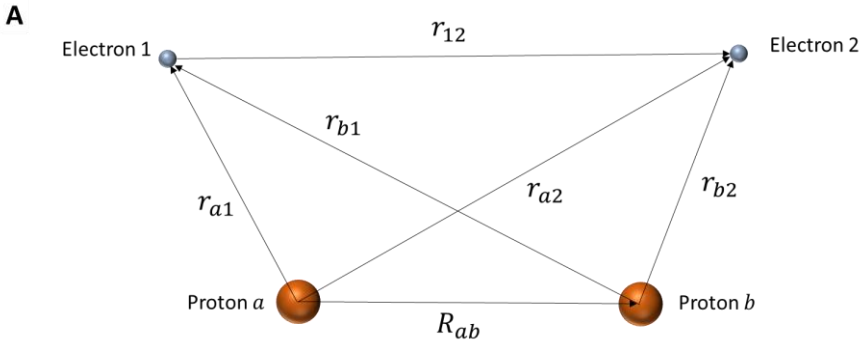

Figure 4.1. Schematic of Heitler-London model. (A) A hydrogen molecule consist of protons a and b and electrons 1 and 2. The electron 1 belongs to proton a while the electron 2 belongs to proton b . The coordinates of two protons are considered fixed.

proton a to the electron 1, such forth. Below is a schematic of this hydrogen molecule system. The spin wavefunction can be categorized into four possible representations by their permutation parity:

Table 4.2. Spin Eigenstates Under Permutation

State	S	S_z
$\frac{1}{\sqrt{2}}\left(\left\|\uparrow\downarrow\right\rangle-\left\|\downarrow\uparrow\right\rangle\right)$	0	**0**
$\left\|\uparrow\uparrow\right\rangle$	1	**1**
$\frac{1}{\sqrt{2}}\left(\left\|\uparrow\downarrow\right\rangle+\left\|\downarrow\uparrow\right\rangle\right)$	1	**0**
$\left\|\downarrow\downarrow\right\rangle$	1	**-1**

We note that the first spin state with S=0 is odd under permutation, while the other three with S=1 are even. Since Pauli principal requires that the total wave function to be odd under permutation, since the total wave function is a product of coordinate wavefunction and the spin wave function, the odd parity spin state (S=0) must be paired with even coordinate wavefunction; the even parity spin state (S=1) must be paired with odd coordinate wavefunction. There is thus a strict correlation between spatial symmetry of the coordinate wavefunction and the total spin: symmetry wavefunction requires symmetric spins, antisymmetric, triplets.

The model states that the electrons are shared between bonded atoms so that a given electrons belong with equal probability to either of two atoms. The solution to the coordinate wavefunction is therefore in the form:

$$\psi(1,2)=\frac{1}{\sqrt{2}}\left(\psi_a(1)\psi_b(2)\pm\psi_a(2)\psi_b(1)\right). \tag{4.6}$$

This presentation can be either symmetric or antisymmetric depending on the sign in the middle, and $+\,(-)$ sign correspond to symmetric (antisymmetric) wavefunction. If we can solve the problem, we will be able to see which state is energetically favored hence which spin configuration is the ground state.

Note that the first two terms in Equation (4.5) are the electrostatic potential for electron and proton that belongs to the first hydrogen atom and the second respectively, which can be treated as the unperturbed term. Meanwhile, the remaining four terms can be treated as perturbation terms (denoted as H') that can be solved by perturbation theory. We hence divide H into:

$$H = H^0 + H', \tag{4.7}$$

where

$$\begin{aligned} H^0 &= -\frac{\hbar^2}{2m}(\nabla_1^{\,2} + \nabla_2^{\,2}) - \frac{e^2}{4\pi\grave{o}_0}\left\{-\frac{1}{|\boldsymbol{r}_{a1}|} - \frac{1}{|\boldsymbol{r}_{b2}|}\right\} \\ H' &= -\frac{e^2}{4\pi\grave{o}_0}\left\{-\frac{1}{|\boldsymbol{r}_{b1}|} - \frac{1}{|\boldsymbol{r}_{a2}|} + \frac{1}{|\boldsymbol{r}_{12}|} + \frac{1}{|R_{ab}|}\right\} \end{aligned}. \tag{4.8}$$

The solution to the perturbation problem is provided by:

$$E_{\pm} = E_0 + \frac{C \pm J_{ex}}{1 \pm B^2}, \tag{4.9}$$

where E_+ is energy for the spatially symmetric solution and the E_- is the energy for the spatially asymmetric solution. C is Coulomb integral, B is overlap integral, and J_{ex} is the exchange integral. They are given by:

$$\begin{aligned} C &= \int \psi_a(\boldsymbol{r}_1)\left(\frac{1}{|R_{ab}|} + \frac{1}{|r_{12}|} - \frac{1}{|r_{a1}|} - \frac{1}{|r_{b2}|}\right)\psi_b(\boldsymbol{r}_2)\mathrm{d}^3 r_1 \mathrm{d}^3 r_2 \\ B &= \int \psi_b(\boldsymbol{r}_2)\psi_a(\boldsymbol{r}_2)\mathrm{d}^3 r_2 \\ J_{ex} &= \int \psi_a^*(\boldsymbol{r}_1)\psi_b^*(\boldsymbol{r}_2)\left(\frac{1}{|R_{ab}|} + \frac{1}{|r_{12}|} - \frac{1}{|r_{a1}|} - \frac{1}{|r_{b2}|}\right)\psi_b(\boldsymbol{r}_1)\psi_a(\boldsymbol{r}_2)\mathrm{d}^3 r_1 \mathrm{d}^3 r_2 \end{aligned}. \tag{4.10}$$

The sign of the second term in (4.9) determines whether E_+ or E_- is the ground state energy. If $\frac{C \pm J_{ex}}{1 \pm B^2} > 0$, then $E_+ > E_-$, the antisymmetric coordinate wavefunction with spin triplet is the

energetically favored, which means the system features ferromagnetic coupling; If $\frac{C \pm J_{ex}}{1 \pm B^2} < 0$, then $E_+ < E_-$, the symmetric coordinate wavefunction with spin singlet is the energetically favored, which means the system features antiferromagnetic coupling.

The exchange interactions happen to be positive in iron, nickel, and cobalt, that's the reason why they are prototype ferromagnets.

4.1.3 *Heisenberg Hamiltonian*

We would like to write the Hamiltonian in a form in which the spin operators are involved so that this energy level schemes are brought out by a spin Hamiltonian. Again we should note that goal here is merely for mathematical simplicity and does imply that the exchange interaction is a real force that is exerted on the spin. Let's use $2J$ to represent the energy difference between the ferromagnetic and antiferromagnetic states for simplicity. Which means from (4.9),

$$2J = E_+ - E_- = \frac{C + J_{ex}}{1 + B^2} - \frac{C - J_{ex}}{1 - B^2} \tag{4.11}$$

Heisenberg first wrote down the Hamiltonian, which is known as Dirac-Heisenberg Hamiltonian:

$$H = -2J\vec{S}_1 \cdot \vec{S}_2 \tag{4.12}$$

It may be readily verified that this Hamiltonian has the features described above and may be used to feature the ground state of a real magnetic model.

If $\vec{S}_1$ and $\vec{S}_2$ are in triplet state (ferromagnetic order), we have

$$\begin{aligned} H_{FM} &= -2J\vec{S}_1 \cdot \vec{S}_2 \\ &= -2J \cdot \frac{1}{2}\left[\left(\left| \vec{S}_1 + \vec{S}_2 \right| \right)^2 - \left| \vec{S}_1 \right|^2 - \left| \vec{S}_2 \right|^2 \right] \\ &= -2J \cdot \frac{1}{2}\left[1 \times 2 - \frac{1}{2} \times \frac{3}{2} - \frac{1}{2} \times \frac{3}{2} \right] \\ &= -\frac{1}{2} J \end{aligned} \quad . \tag{4.13}$$

If $\vec{S}_1$ and $\vec{S}_2$ are in singlet state (antiferromagnetic order), we have

$$\begin{aligned} H_{AFM} &= -2J\vec{S}_1 \cdot \vec{S}_2 \\ &= -2J \cdot \frac{1}{2}\left[\left(\left| \vec{S}_1 + \vec{S}_2 \right| \right)^2 - \left| \vec{S}_1 \right|^2 - \left| \vec{S}_2 \right|^2 \right] \\ &= -2J \cdot \frac{1}{2}\left[0 \times 1 - \frac{1}{2} \times \frac{3}{2} - \frac{1}{2} \times \frac{3}{2} \right] \\ &= \frac{3}{2} J \end{aligned} \quad . \tag{4.14}$$

The energy difference between the two states is

$$\Delta H = H_{AFM} - H_{FM} = 2J \, . \tag{4.15}$$

We note that with the situation in which antiferromagnetic state lying below the ferromagnetic state, we can take J<0 and the same representation of Dirac-Heisenberg Hamiltonian is kept.

A real solid-state magnetic material with long-range order actually contains a large number of ordered spins. Starting from the Dirac-Heisenberg Hamiltonian for two spins, we can write the Hamiltonian for a large number of spins as

$$H = -2J \sum_i \vec{S}_i \cdot \sum_{j \neq i} \vec{S}_j \, . \tag{4.16}$$

The second summation is summed over all the neighboring spins j around the site i. We assume the exchange interaction is the only nonzero between adjacent spins.

4.1.4 *Direct exchange, RKKY interaction, superexchange*

Above we have discussed on the exchange interaction presented by Heitler–London Model. This form of exchange interaction is rooted in the direct wavefunction overlapping between two adjacent atoms. Whether it's ferromagnetic, antiferromagnetic the exchange interaction between magnetic ions will force the individual moments into ordered alignments. Meanwhile, this type of exchange accounts for many magnetic systems in the world, there are other types of exchange interaction that are also common and has been intensively studied. In this section we will discuss two more major types of exchange interactions: a) RKKY interaction b) Superexchange interaction. RKKY exchange interaction is named after Ruderman, Kittle, Kasuya, and Toshida. It is a major type of exchange interaction is rare earth metals, where there is little or no overlap between neighboring electrons. They are therefore coupled through an intermediary electron (itinerant electron), which in metals are the conduction band electrons. A magnetic ion induces a spin polarization in the conduction band of the itinerant electron, which is then felt by the moment of another magnetic ion in range, causing the coupling. An important feature of the RKKY interaction is that its coefficient j oscillates up and down between positive and negative as the separation of the ion changes and has a damped oscillatory nature. Therefore, by tuning the separation one can change the coupling between ferromagnetic and antiferromagnetic.

Superexchange, also known as Kramers–Anderson superexchange is another exchange coupling that occurs between two ions that do not have direct contact with. It is coupled through an intermediary non-magnetic material. Superexchange is usually seen in transition metal oxides such as MgO. It originates from electrons having come from the same donor atom and being coupled with the receiving ion's spins. Furthermore, the Pauli principal dictates that between two magnetic

ions with half-occupied orbitals, the superexchange will be strongly antiferromagnetic while the coupling between an ion with a filled orbital and one with a half-filled orbital will be ferromagnetic.

4.2 SPINTRONICS

Before the 80s of last century, most information technologies are developed based on the concept of electronics, such as transistors, which was invented at Bell Labs in December 1947. During the 1980s, a new concept, spintronics, concerning spin-dependent transport properties emerged. Spintronics represent and rapidly developing field that holds unique properties such as non-volatile memory. In this chapter, we present several important spintronic device designs.

4.2.1 *Giant Magnetoresistance*

Giant magnetoresistance effect (GMR) was designed based on spin-polarized electronic transport. It is a quantum mechanical effect observed in layered magnetic thin film structures that are composed of alternating ferromagnetic and nonmagnetic layers. The conductance is dependent on the relative orientation of neighboring magnetic layers. When they are parallel, the spin dependent carrier scattering is minimized, and the device has the lowest resistance; when the ferromagnetic layers are anti-parallel, the spin dependent carrier scattering is maximized, and the materials has the highest

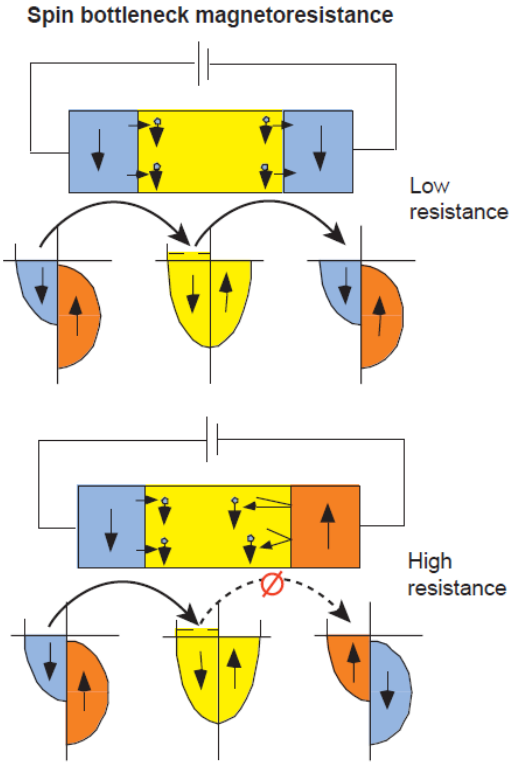

Figure 4.2. Schematic of GMR. (A) example of GMR. The device composes two ferromagnetic layers separated by a non-magnetic metal. If the two conductive channel in the FM metal, the device is in low resistance state, antiparallel, high resistance. The figure is reproduced from Prinz, G.A. Science, 1998. 282(5394): p. 1660.

resistance, as demonstrated in Figure 4.2. The discovery of GMR is announced first in 1988[32], only 6 years later the first commercial product was available[33].

Practically, this two layers system are usually referred to as “spin valves” [34], in which one of the layer is easily reversed by external magnetic field while the other is much more difficult to reverse. The soft layer then acts as valve control and is very sensitive to the external field. The GMR can be used to sense magnetic field then converted it into electronic signals. It has numerous applications.

4.2.2 *Magnetic heterostructures examples*

Another luring direction is integrating the magnetism into semiconductors. The advancements in semiconductors has irreplaceable importance in the last 100 years which has shaped up our information era. Integrating magnetism into semiconductors, for example, would facilitate an all-in-one-chip computer.

To developing the ferromagnetism in semiconductor, it is desired to find a ferromagnetic semiconductor, combining the high mobility of charge carriers in semiconductor and the magnetism of conventional ferromagnetic. However, fulfill all these demands in a monolithic semiconductor structure with ferromagnetic properties is difficult. For example, low-temperature ferromagnetic semiconductors, such as GaMnAs, InMnAs has rather poor mobility for charge carrier transport. As an alternative strategy, it has been suggested that a hybrid system—magnetic heterostructure that consists of a ferromagnet and a semiconductor could use different constituents take over separate tasks required for making functional devices.

A key to successful design is to achieve interaction between the ferromagnet and the semiconductor, which breaks the degeneracy of spins or create spin polarization in the semiconductor. For example, utilizing spin injection ferromagnet and semiconductor to induces

spin polarization[35] is widely studied. It was also found that the nuclear polarization in the semiconductor tracks the magnetization of the ferromagnetic layer and influence the coherent spin dynamics of the photoexcited electrons via hyperfine interaction. Such as Mn-based hybrid ferromagnetic/n-GaAs structure.

Here we present researches on $Ga_{1-x}Mn_xAs$/InGaAs quantum well (QW), separated by a GaAs spacer[35]. The former is ferromagnet, while the latter is a semiconductor. The Mn content x is ~5%. The Mn ions supply holes with density ~10^{13}–$10^{14}$$cm^{-2}$, mediating the ferromagnetism of GaMnAs with a Curie temperature of ~35K. A portion of the charge carrier can be injected into the QW through the spacer.

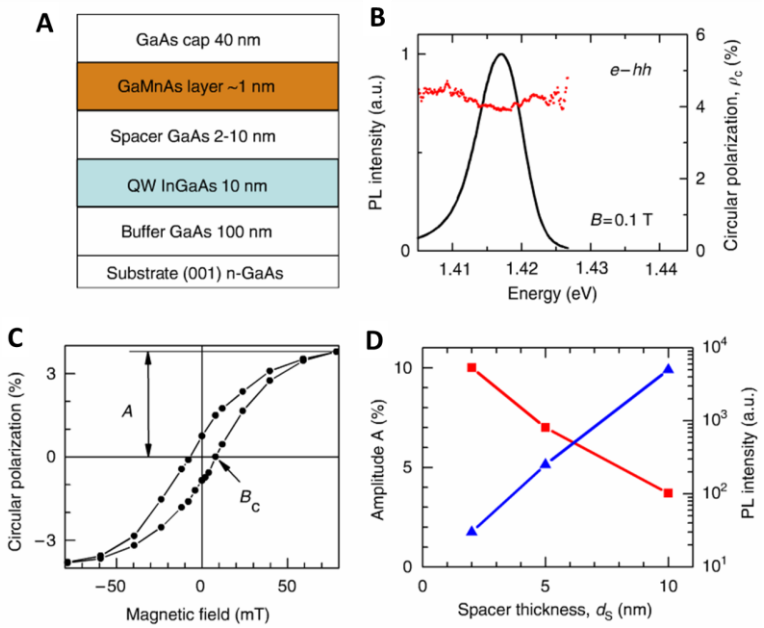

Figure 4.3. Photodetection of spin injection. (A) Scheme of structures. The brown layer indicates the ferromagnet layer. The cyan layer indicates the quantum well. **(B)** Spectra of photoluminescence intensity and polarization under linearly polarized excitation. The spacer thickness 10nm. **(C)** $\rho_c(B)$ hysteresis loop in faraday geometry. The B_c is the coercive Field; **(D)** dependence of amplitude and PL intensity on the spacer thickness. The figure is reproduced from Korenev, V.L., et al., Nature Communications, 2012. 3: p. 959

To detect the spin injection, the sample is illuminated by the 1.92eV laser. An emission at 1.417eV is seen which arise from recombination of electrons and heavy holes in the quantum well states. The intensity of σ^+ and σ^- are measured separately. And the spin polarization is detected from $\rho_c = \frac{(I_{\sigma^+} - I_{\sigma^-})}{(I_{\sigma^+} + I_{\sigma^-})}$ of PL circular polarization. In Figure 4.3B, The red point shows

the circular polarization of ρ_c in an external Faraday magnetic field B of 0.1T. The faraday In Figure 4.3C, we show the hysteresis loop ρ_c measured at the PL maximum under linearly polarized above-barrier excitation. The coercive field is around 9mT, and the maximum polarization measured around 80mT field strength is 3.5%. The hysteresis loop that appears in ρ_c is a demonstration that a carrier polarization in QW is established in accordance with GaMnAs's magnetization. To explain this connection, the first theorem is that it is built by exchange interaction of the carriers in QW with Mn-ions. As the Mn spin with g-factor of 2 is directed against the external magnetic field, the equilibrium spin of QW holes (electrons) would be oriented along (against) the magnetic field, because of the antiferromagnetic (ferromagnetic) coupling with the Mn spins. However, this explanation is not supported by the spacer thickness dependent measurement. As shown in Figure 4.3D, a considerable drop in PL intensity and linear increase of polarization is seen with decreasing spacer thickness d_s. This hints an effective capture of charge carriers by the FM owning to tunneling through the GaAs spacer. In contrast, the exchange interaction mechanism would predict an exponential d_s-dependence due to the exponential decay of exchange coupling strength. This is explained by photo-excited QW electrons, with spins either along or opposite to the magnetization of the ferromagnet, are captured by the FM at different rates. This leads to accumulation of electron-spin polarization in the QW, resulting in a circular polarization of the PL.

Chapter 5. SPINTRONICS AND VALLEYTRONICS IN WSe_2/CrI_3 HETEROSTRUCTURES

In the last chapter, we discussed several theoretical and experimental aspects of exchange coupling. Using $Ga_{1-x}Mn_xAs$/InGaAs QW as an example, we lead to the point that manipulating exchange interaction in magnetic heterostructures has proven to be an effective way to engineer highly functional materials [32, 36, 37]. Heterostructures of magnetic material integrated with superconductors[38] topological insulators [39-41] have been proposed and investigated. Since the emerging of 2d materials, the versatility for 2d materials has made it a tantalizing platform for numerous physical phenomena. Our work described in this chapters extends the field of magnetic heterostructure to the new territory by constructing and exploring the exchange interaction in a van der Waals interface between a monolayer WSe_2 semiconductor and an ultrathin ferromagnetic insulator CrI_3 [42].

The bulk of this chapter describes our work on optical characterization on WSe_2/CrI_3 heterostructures, reprinted from[43]. In this work, we create van der Waals heterostructures formed by an ultrathin ferromagnetic semiconductor CrI_3 and a monolayer of WSe_2. We achieve unprecedented control of the spin and valley pseudospin in WSe_2, where we detect a large magnetic exchange field of nearly 13 T and rapid switching of the WSe_2 valley splitting and polarization via flipping of the CrI_3 magnetization. The WSe_2 photoluminescence intensity strongly depends on the relative alignment between photo-excited spins in WSe_2 and the CrI_3 magnetization, which is due to ultrafast spin-dependent charge hopping across the heterostructure interface. The photoluminescence detection of valley pseudospin provides a simple and effective method to probe the intriguing domain dynamics in the ultrathin magnet as well as the rich spin interactions within the heterostructure.

5.1 CrI_3—An Layered Structured Magnet

At being of the project, I was started with the idea to use EuS, instead of CrI_3 for the magnet, which can be grown by the electron beam evaporation. Among 6 devices that were made, only one had shown excitonic emission from WSe_2, and the rest are either low quality or damaged during the evaporation. Luckily, the result with that one was cheerful. Amplified Zeeman effect by the exchange field was observed by polarization resolve photoluminescence measurement, the magnetic dependence also showed interesting features. However, I had never been able to fabricate another working device to complete the project successfully. The lesson I learned from this was that the good interface is not always desired in such design, and device quality could depend on the orientation, domain size, dangling crystal bond, which could vary from sample to sample. Furthermore, the complexity of fabricating the heterostructure poses a risk for damaging the fragile WSe_2. Meanwhile, it had been known that the stacking of Van der Waals materials easily achieves atomically smooth interface, because the fabrication process does not involve procedures that could lead to device damage, such as exposure to radiating electron beams. Eilightened by this, I was hoping to find a Van der Waals magnet to replace EuS.

This thought diverted our attention to CrI_3. At that time, a fresh paper came out about the characterization of bulk CrI_3, which is a Van der Waals magnet. CrI_3 is a layered insulating ferromagnet with Curie temperature of 61K. The saturation moment for CrI_3 is μ_B/Cr. The easy axis is in the out-of-plane direction, which fits our application perfectly. McGuire et al showed that it is monoclinic at room temperature, then undergoes a phase transition upon cooling to ~180K, which modifies its interlayer stacking order, turning the crystal structure into rhombohedral at low temperature.

5.2 Heterostructure Fabrication

CrI_3 quickly hydrate in air, decomposing in seconds. Therefore, the fabrication and the transfer was done in the glovebox with O_2 and H_2O levels below 0.5 ppm. Two flakes of hBN were used

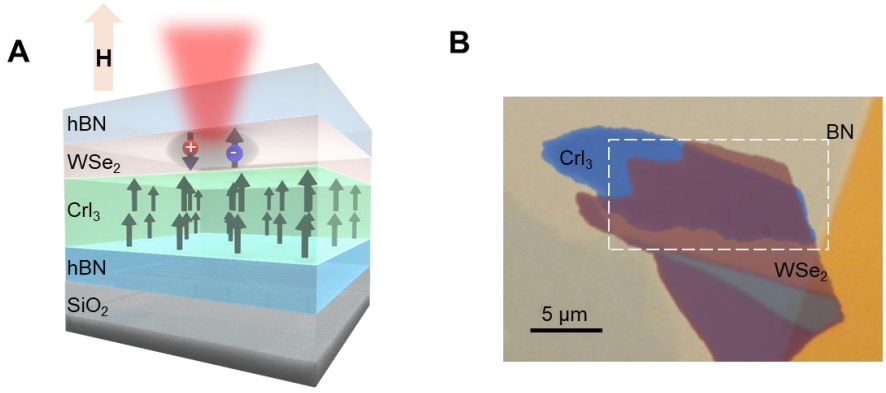

Figure 5.1. Schematics of WSe_2/CrI_3 device. (A) Device architecture, with BN/WSe_2/CrI_3/BN stacked from top to bottom. **(B)** Top view of the device. Both BN are larger than the scope of the image. They thus serve as sealed protection for both layers. Due to light reflection from multiple interfaces of the HS, the visibility of encapsulated layers in the original picture is compromised. This image is remade from overlay of individual pictures for clarity.

to encapsulate the WSe_2/CrI_3 heterostructure. We used ~10nm CrI_3 with monolayer WSe_2. The encapsulating BN was about 10nm~20nm. Not only they protect the device from the air when it is loaded into the cryostat in air, but also insulate it from the roughness of the SiO_2 substrate, ensuring high quality of the device. The device architecture is illustrated in Figure 5.1. There were no signs of degradation in the h-BN sandwiched sample in ambient conditions for at least an hour, allowing us to transport and mount the sample for measurement.

5.3 Polarization-resolved Photoluminescence Measurement

Photoluminescence was used to excitation and detection of the excited carriers in WSe_2. Optical selection rule connects the spin and valley index of electron and hole pair with the helicity of light (see chapter 2.3.1). Exciting WSe_2 with σ^+ helicity, we can selectively excite excitons in the +K valley that is composed of a spin up electron and a spin down hole; Exciting WSe_2 with σ^- helicity,

we can selectively excite excitons in the −K valley that is composed of a spin down electron and a spin up hole. For detection, since excited carriers recombine to generate luminescence, reading helicity resolved photoluminescence identifies the population of spin-polarized excited carriers. In addition, the luminescence energy is the optical transition energy between the conduction and valence band with the identical spin direction. We can thus measure the band shift by reading out the peak position of the luminescence.

The device was measured in a continuous helium flow cryostat with a 7T superconducting magnet, which can operate in a both Faraday and Voigt geometry. A continuous-wave HeNe laser (1.96eV) was used for above bandgap excitation of WSe_2. The laser was power-stabilized (30 μW) and focused to ~1 μm with an aspheric lens. The back-reflected PL was collected by the same lens and detected using a spectrometer and Si CCD. Samples were measured at 5K and in Faraday geometry unless otherwise specified. For the magnetic field measurements, we continuously sweep the field and collect the PL for the full hysteresis loop for each polarization before switching to the next polarization. Good overlap between the start point and the end point indicated the stability of the measurement and allowed comparison between two field sweeps with different polarizations.

A two-axis piezoelectric scanning mirror allowed us to raster scan the laser spot over the desired region for spatially resolved measurements. We use liquid crystal variable retarder for fast switching between the two polarizations within 100ms time frame. Two polarization were measured on the same spot before moving on to the next spot. This back-to-back measuring method ensures that the sample drifting does not effect the validity of the polarization measured for each pixel.

5.4 SPONTANEOUS TIME REVERSAL SYMMETRY BREAKING

5.4.1 *Strong Exchange Interaction In The Heterostructure*

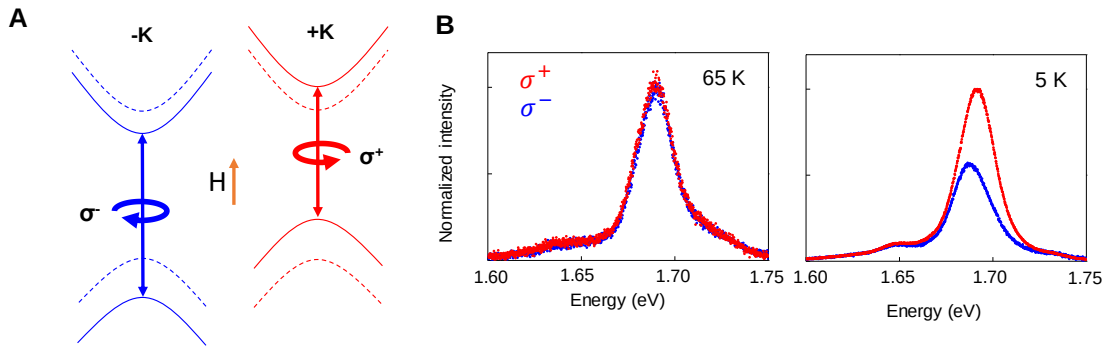

Figure 5.2. Polarization-resolved measurement on WSe_2/CrI_3 Heterostructure. (A) Optical transition energy diagram. The PL emission helicity is locked with spin and valley index. The PL energy correspond to optical bandgap size, which is shifted by (effective) magnetic field. **(B)** PRPL measurement without external magnetic field. The red (blue) curve correspond to exciting with σ^+ (σ^-) and detecting with the same helicity component in PL. Above T_C (65K), the time reversal symmetry is reserved; below T_c, the time reversal symmetry is broken due to spontaneous magnetization.

After loading the sample, we cooled it down to 65K, above the T_c of CrI_3. Figure 5.2B (left panel) shows the PL spectrum of the device. The labeling σ^+ and σ^- indicates both the excitation and detection polarization for the spectrum. Here the σ^+ and σ^- spectra are nearly identical, as expected from time-reversal symmetry between the valleys in WSe_2.

The PL peak is attributed to a positively charged trion state in WSe_2 due to the type-II band alignment, with the CrI_3 conduction band lying below that of WSe_2. The band alignment is determined by DFT calculations, which is shown in Appendix A1.

Remarkably, the valley degeneracy was lifted as the sample was cooled below the T_C of CrI_3. Figure 5.2B (right panel) shows a representative spectrum taken at 5 K. The σ^+ spectrum exhibits both larger peak intensity and energy than σ^-. By fitting them with a double peak, we can extract the parameters of each peak. The extracted valley splitting, defined as $\Delta = E_{\sigma^+} - E_{\sigma^-}$, is about 3.5 meV. Combining with the fact that the Zeeman splitting for the very same WSe_2 flake without

being stacked with CrI_3 was measured to be 260 μeV/T , we hence estimate the CrI_3 induced exchanged field to be 13T. The magnitude of the valley splitting is independent of the excitation power, which rules out carrier density effects as a dominant mechanism for the valley splitting. Thus, we attribute the energy splitting to a strong magnetic exchange field between the CrI_3 spins and WSe_2 excitons. We emphasize that since the optical transition is determined by the energy difference between the conduction and valence bands, the observed valley splitting reflects the distinct coupling of the exchange field with the conduction and valence bands (Figure 5.2A, solid lines). This mechanism of Zeeman splitting has been discussed in Chapter 2.5. In the following sections, we ignore the direct influence of the external magnetic field on WSe_2 PL intensity and energy [25, 44-46], since the exchange field is much stronger than the applied magnetic field (typically < ~1 T).

5.5 Field Dependent Proximity Effect

In addition to strong exchange coupling revealed by PL measurement, represented by the large valley splitting, the large intensity difference between two polarizations is also evident, which will be discussed in this section. Another task in this chapter is to reveal the relation between the direction of magnetization and the sign of exchange coupling. To answer these questions, we conducted further measurements below.

We did polarized PL while sweeping an applied magnetic field B perpendicular to the sample plane (Faraday geometry, B parallel to easy-axis, Figure 5.2A). In Figure 5.3A, the total PL intensity (I) for σ^- excitation (no polarization selection for detection) and σ^+ excitation (no polarization selection for detection) is plotted as a function of B field and emission energy for device 1. Six distinct regimes are denoted by the arrows, with three sharp jumps in PL intensity and peak energy near 0 T and ±0.85 T, and two smaller jumps near ±1.85 T. Figure 5.3B illustrates

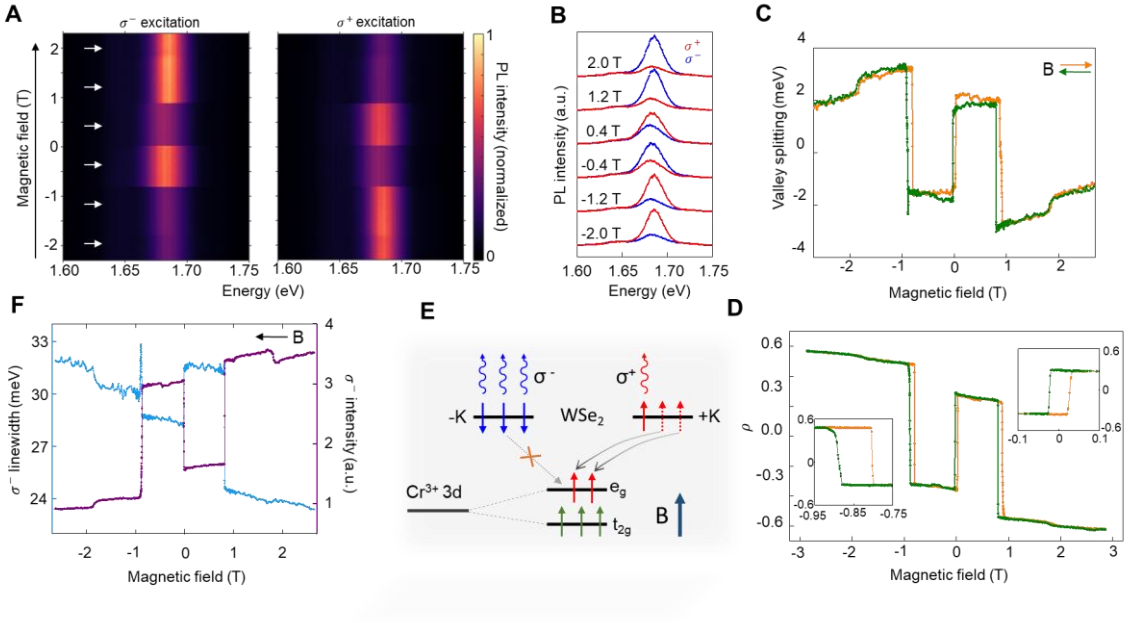

Figure 5.3 Ferromagnetic substrate control of spin and valley pseudospin dynamics. (A) Photoluminescence intensity plot as a function of emission energy and magnetic field for σ^- and σ^+ excitation. The black arrow indicates the applied magnetic field sweeping direction. **(B)** σ^+ and σ^- spectra at selected magnetic field (indicated by the white arrows in A). See text for definition of σ^+ and σ^-. **(C)** Valley splitting and **(D)** normalized PL intensity difference between σ^+ and σ^- as a function of applied magnetic field sweeping up (orange) and down (green). Insets in (D) are zoom-in plots of hysteresis curves. **(E)** Schematic depicting the spin-orientation-dependent charge hopping between WSe_2 and CrI_3, which leads to helicity-dependent PL in A. See text for descriptions. **(F)** σ^- PL spectra peak width (blue) and intensity (purple) vs B field (sweeping from positive to negative). Broad width is always associated with weak PL intensity.

the overlaid σ^+ and σ^- spectra at six selected magnetic fields corresponding to each region, highlighting the multiple jumps in peak energy and intensity. Figure 5.3C and D show the valley splitting and the normalized difference between σ^+ and σ^- intensities, $\rho = (I_{\sigma^+} - I_{\sigma^-})/(I_{\sigma^+} + I_{\sigma^-})$, as a function of increasing (orange curve) and decreasing (green curve) B field. Hysteresis loops, a hallmark of ferromagnetic effects, are observed at B = ±0.85 T and B = 0 T. The widths of observed hysteresis loops are around 50 mT. These hysteresis loops determinately associate the three jumps in ρ and Δ with magnetization reversal in CrI_3. Since in high external magnetic field, the FM CrI_3 tends to be magnetized in the direction of the external field, we conclude that the up magnetized CrI_3 leads to the reduction of emission from +K valley, as well as a red shift of PL energy from the +K valley.

To understand the mechanism for PL intensity reduction in one valley, in Figure 5.3F, we show the relation between the peak intensity and peak width for σ^-. The trend is observed that the linewidth broadens whenever the PL intensity decreases, and vice versa. In other words, the intensity reduction comes with a reduction in carrier lifetime, implying an extra relaxation channel. The channel is revealed by inspecting of band alignment between WSe_2 and CrI_3. In CrI_3, the lowest energy unoccupied conduction bands are mainly composed of the Cr atom's e_g orbitals spin polarized in major spin direction (Figure 5.3E). Therefore, electron charge hopping from WSe_2 to CrI_3 is only allowed for the aligned spin $|K, \uparrow>$ (Figure 5.3E). Under the condition that optical absorption at 1.96 eV is independent of light helicity, the electron spins created by σ^+ excitation have an extra non-radiative relaxation channel compared to σ^- excitation. This results in strongly quenched PL, as well as a broader spectral linewidth, compared to L excitation. The helicity-dependent PL is similar to the GaMnAs/GaAs QW system we discussed in the last chapter. However the PL polarization modulation is an order of magnitude stronger in our system with an order of magnitude smaller applied magnetic field range.

We can estimate the hopping rate by the difference in spectral width between σ^+ and σ^- conditions. For B = 1 T, the difference is ~5 meV, implying a spin-dependent charge hopping rate on the order of $\hbar / (5\text{meV}) \approx 130\, fs$, where $\hbar$ is Planck constant.

Another prominent feature in Figure 5.3C and D is the sharp change of the valley splitting and ρ near B = ±0.85 T and 0 T. For example, when we sweep the applied magnetic field down through the transition near B = -0.85 T, the valley splitting changes from -1.3 meV to 3.4 meV in a span of about 30 mT (Figure 5.3C). This corresponds to a valley splitting rate of over 150 meV/T, nearly three orders of magnitude larger than can be achieved by the Zeeman effect in bare WSe_2. Furthermore, when sweeping through -0.8 T in the other direction and also near zero field, the

switching is even faster, occurring within a $\leqslant$ 6 mT span. The sign change of the valley splitting and ρ implies a fast magnetization flip of the CrI_3 magnetization, which will be discussed in the next ection.

5.6 Polarization-Resolved PL Domain Imaging

An unclear issue so far is that dynamics of CrI_3's magnetization. Spatial maps of CrI_3 magnetization, represented by ρ from WSe_2 PL spectrum, can reveal the underlying magnetic domain structure. Inspired by this, we performed spatially resolved, polarized PL measurements as a function of applied magnetic field on device 2 (boxed region in Figure 5.1B). Figure 5.4 shows spatial maps of ρ as a function of magnetic field sweeping direction, which are ordered to highlight time-reversal pairs. The time-reversal pair consists of the two maps acquired at opposite applied magnetic field while sweeping in opposite direction. In the figure, each time reversal pair shows excellent consistency in their pattern except for the opposite sign, validating the stability of the system. We note that the domain structure and ρ disappear above ~60 K (Appendix A2), indicating that T_C is similar to bulk CrI_3 [42].

These maps reveal the evolution of the domain structure between -1.1 to 1.1 T in the ultrathin CrI_3. When the applied magnetic field is larger than the coercive field, the uniform color across the entire heterostructure indicates full magnetization of CrI_3. When the applied magnetic field is set at an intermediate value, a multi-domain structure appears with a domain size on the order of a few microns. We define domains that only switch signs with the applied magnetic field reversal as strong domains (indicated by the red arrow in B = -0.5 T map), while those that flip without switching magnetic field as weak domains (indicated by the blue arrow). Unlike the strong domains, the weak domains flip three times within one sweep. Therefore, if the laser spot is on a

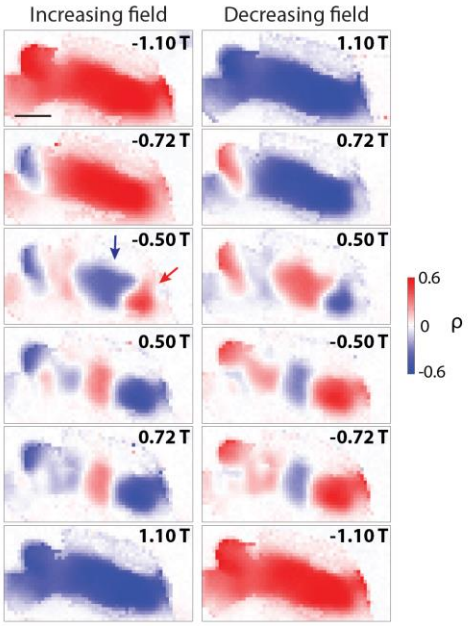

Figure 5.4. Polarization-resolved micro-photoluminescence imaging of domain structures as a function of applied magnetic field. Each panel is spatial map of ρ (see text for definition) at selected magnetic field. Left and right columns are arranged in a time-reversal manner corresponding to increasing (left) and decreasing (right) applied magnetic field, respectively. The blue arrow indicates a domain which flips sign of ρ three times by sweeping the applied magnetic field, while red arrow points to a domain flipping sign of ρ once. Scale bar, 3 μm.

weak domain, the corresponding valley splitting and ρ will also flip three times within one sweep, which is consistent with the observation in Figure 5.3C and D. A plausible interpretation of the multiple flips is the competition between the Zeeman energy and the magnetic dipole energy between strong and weak domains. In a certain applied magnetic field range, the dipolar interaction exceeds the Zeeman energy in a weak domain, which causes it to flip to reduce the magnetic dipole energy. A simple model of the magnetic domain evolution, which considers the Zeeman energy, the dipolar interaction between strong and weak domains, and the easy-axis anisotropy, qualitatively reproduces the observed curves in Figure 5.3C (Appendix A3).

5.7 Position Dependent Magnetic Domain Dynamics

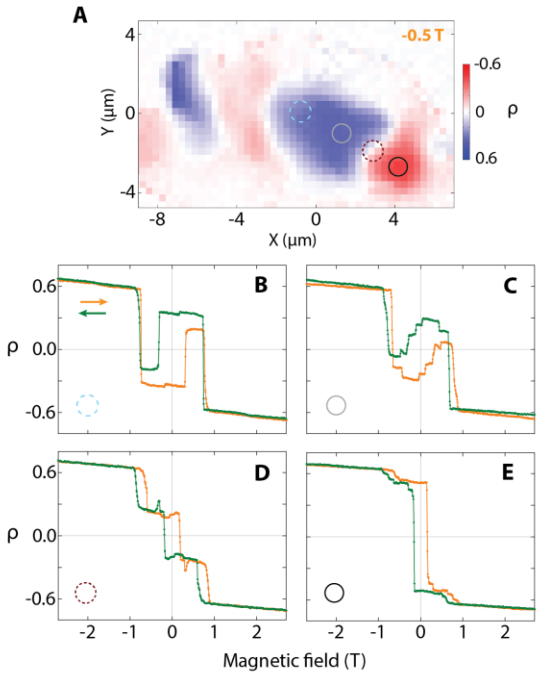

Figure 5.5. Position-sensitive ferromagnetic domain dynamics. (A) Spatial map of ρ from Fig. 3 (-0.5 T, sweep down) with blue, gray, brown, and black colored circles indicating the spots of selected magnetic field sweeps of ρ in **(B), (C), (D)**, and **(E)**.

Measurement of the valley-polarized exciton PL in WSe_2 additionally provides a new local probe to investigate spin and domain dynamics in adjacent ferromagnets through van der Waals engineering. Figure 5.5 shows multiple distinct ρ vs B curves at different sample positions. As expected from the spatial maps in Fig. 3, if the laser is focused on a weak domain (Figure 5.5 B and C), the magnetization can flip without changing applied magnetic field direction, while in a strong domain (Figure 5.5E), there is only one hysteresis loop centered at zero field. In addition to coarse changes in magnetization, fine structure is also observed. For instance, in Figure 5.5C we observe fine steps in ρ as the applied magnetic field varies. At first glance, the observation is an echo of the Barkhausen effect due to the rapid change of the domain size in ferromagnets. However, the laser spot is towards the center of the weak domain, which is less likely to be affected by changes in domain size. Furthermore, the ρ vs B curves near the domain boundary do not

exhibit these fine steps, as shown in Figure 5.5D. One possible explanation is that the magnetization in thin CrI_3 flips layer by layer, as in certain types of layered antiferromagnets [47, 48], and the magnetic moment dynamics of the second and lower layers are transmitted to the top layer through the dipolar interaction. In addition, Figure 5.5D shows an overshoot of ρ (or spikes) which may be related to negative differential magnetization [49]. Further interesting topics include unraveling the origin of the slow jumps at ±1.85T, which manifest themselves as an opposite trend between Figure 5.3C and D, and may indicate a different origin from the other jumps at lower fields.

All of these intriguing phenomena will require additional study to elucidate the underlying mechanisms. It is already evident, however, that this probe is highly sensitive to spin interactions and magnetization dynamics, providing a powerful addition to conventional techniques such as magneto-optic Kerr rotation (MOKE) in studying magnetism in thin films. In addition, the integration of van der Waals magnetic materials into other heterostructures should empower researchers to harness exchange interactions and interfacial effects for exploring novel physical phenomena and spintronics at the atomically thin limit.

Chapter 6. ATOMICALLY THIN MAGNET

In the last chapter, we discussed an example in which ultrathin magnetic CrI_3 is applied in valleytronics devices for control of the valley properties of known semiconductor—WSe_2. It can also be expected that the van der Waals magnet such as CrI_3' will have a bright future in spin and valleytronics applications. Nonetheless, CrI_3 was still the first van der Waals materials of which the property of ultrathin flakes was discussed. It was strongly suggested that the understanding of the van der Waals magnetic materials will not only enrich the researcher's knowledge to the world of magnetic materials, but also stimulate the development of spin and valleytronics.

In this chapter, we will discuss our original work on exploring the first 2d magnet in the world—atomically thin CrI_3. This work was reprinted from published study[50], Bevin Huang, Genevieve Clark, Efren Navarro-Moratalla, Dahlia R. Klein, Ran Cheng, Kyle L. Seyler, **Ding Zhong**, Emma Schmidgall, Daniel Larson, Michael A. McGuire, David H. Cobden, Wang Yao, Efthimios Kaxiras, Di Xiao, Pablo Jarillo-Herrero, Xiaodong Xu. *Layer-dependent ferromagnetism in a van der Waals crystal down to the monolayer limit*. Nature, 2017. 546: p. 270. Our experiment demonstrated that monolayer chromium triiodide (CrI_3) is an Ising ferromagnet, i.e. it exhibits out-of-plane spin orientation below the Curie temperature of 45 K. Magneto-optic Kerr effect (MOKE) studies depict a strong dependence of MOKE signal on the number of layers, revealing thickness-dependent magnetic states[5, 10, 51]. Remarkably, bilayer CrI_3 displays suppressed Ising ferromagnetism with a metamagnetic effect[52]. Our work opens opportunities for studying magnetism by harnessing the unique features of atomically-thin materials, such as exquisite electrical control for realizing magnetoelectronics[53], and van der Waals engineering for novel interface phenomena[54].

Before diving into experiments, we will discuss an existing theorem on 2d magnets, which exposes strict condition to the existence of 2d material—Mermin-Wagner theorem[55, 56].

6.1 Mermin-Wagner Theorem

We start by focusing on a simple model: the classical xy model, where we have a square lattice with a planar spin on each site. The Hamiltonian takes the form:

$$H = -J\sum_{\langle i,j\rangle} \boldsymbol{s}_i \cdot \boldsymbol{s}_j = -J\sum_{\langle i,j\rangle} \cos(\phi_i - \phi_j)\,. \tag{6.1}$$

To characterize the system, we define a correlation function,

$$c(\boldsymbol{r}-\boldsymbol{r}') = \left\langle e^{i(\phi(\boldsymbol{r})-\phi(\boldsymbol{r}'))} \right\rangle. \tag{6.2}$$

In any system with long-range order, the $\phi(\boldsymbol{r})$ is spatially homogeneous and the correlation function is non-zero even at large distances. On the other hand, if the correlation function goes to zero after finite correlation length, the systems do not persist long-range order.

If the temperature is zero, according to the form of Hamiltonian, all the spins point in the same direction, and the ground state spontaneously breaks the symmetry. The correlation function is 1. However, we will show that as long as the temperature is finite, the correlation function vanishes. Let's assume the temperature is low enough that the fluctuation between adjacent spins is small. The Hamiltonian can be approximated by:

$$H = E_0 + \frac{J}{2}\sum_{\langle i,j\rangle} (\phi_i - \phi_j)^2\,. \tag{6.3}$$

The temperature is also assumed low enough that the correlation length is much larger than the lattice spacing, so that we can go to the continuum limit,

$$H \approx \frac{J}{2}\int d^2x(\nabla\phi(\boldsymbol{r}))^2 . \tag{6.4}$$

Going into the Fourier space, we have $\phi(\boldsymbol{r}) = \frac{1}{2\pi}\int \phi(\boldsymbol{k})e^{i\boldsymbol{k}\cdot\boldsymbol{r}}d^2k$, thus

$$\begin{aligned} H &= -\frac{J}{2(2\pi)^2}\int d^2r\int d^2k\int d^2k' e^{i\boldsymbol{k}\cdot\boldsymbol{r}}e^{i\boldsymbol{k}'\cdot\boldsymbol{r}}\phi(\boldsymbol{k})\phi(\boldsymbol{k}')\boldsymbol{k}\cdot\boldsymbol{k}' \\ &= \frac{J}{2}\int d^2k\phi(\boldsymbol{k})\phi(-\boldsymbol{k})k^2 \\ &= \frac{1}{2}\int d^2k\grave{o}(\boldsymbol{k})\left|\phi(\boldsymbol{k})\right|^2 \end{aligned} \quad . \tag{6.5}$$

Where $\grave{o}(\boldsymbol{k}) = Jk^2$. Consider that the original field $\phi(\boldsymbol{r})$ is real, so $\phi(-\boldsymbol{k}) = (\phi(\boldsymbol{k}))^*$. In fact, the terms for $\boldsymbol{k}$ and $-\boldsymbol{k}$ are identical, we have

$$H = \int_{k>0} d^2k\grave{o}(\boldsymbol{k})\left|\phi(\boldsymbol{k})\right|^2 . \tag{6.6}$$

With this expression, we can now calculation partition function,

$$\left\langle \phi(\boldsymbol{k})\phi(\boldsymbol{k}')\right\rangle = \frac{\int d\phi\cdot\phi(\boldsymbol{k})\phi(\boldsymbol{k}')e^{-\beta H}}{\int d\phi\cdot e^{-\beta H}} = \frac{\delta(\boldsymbol{k}+\boldsymbol{k}')}{\beta\grave{o}(\boldsymbol{k})} . \tag{6.7}$$

Recall that we need to calculate $c(\boldsymbol{r}-\boldsymbol{r}') = \left\langle e^{i(\phi(\boldsymbol{r})-\phi(\boldsymbol{r}'))}\right\rangle$, since we have a gaussian Hamiltonian, it is equal to

$$c(\boldsymbol{r}-\boldsymbol{r}') = e^{-1/2\left\langle(\phi(\boldsymbol{r})-\phi(\boldsymbol{r}'))^2\right\rangle} . \tag{6.8}$$

To calculate $\left\langle(\phi(\boldsymbol{r})-\phi(\boldsymbol{r}'))^2\right\rangle$, we use Fourier transformation again,

$$\begin{aligned}\left\langle(\phi(\boldsymbol{r})-\phi(\boldsymbol{r}'))^2\right\rangle &= \int\frac{d^2k'd^2k}{(2\pi)^2}(e^{i\boldsymbol{k}\times\boldsymbol{r}}-e^{i\boldsymbol{k}'\times\boldsymbol{r}'})(e^{i\boldsymbol{k}\times\boldsymbol{r}}-e^{i\boldsymbol{k}'\times\boldsymbol{r}'})\left\langle\phi(\boldsymbol{k})\phi(\boldsymbol{k}')\right\rangle \\ &= \frac{1}{(2\pi)^2}\int d^2k'd^2k(e^{i\boldsymbol{k}\times\boldsymbol{r}}-e^{i\boldsymbol{k}\times\boldsymbol{r}'})(e^{i\boldsymbol{k}'\times\boldsymbol{r}}-e^{i\boldsymbol{k}'\times\boldsymbol{r}'})\frac{\delta(\boldsymbol{k}+\boldsymbol{k}')}{\beta\grave{o}(\boldsymbol{k})} \\ &= \frac{1}{(2\pi)^2}\int d^2k(e^{i\boldsymbol{k}\times\boldsymbol{r}}-e^{i\boldsymbol{k}\times\boldsymbol{r}'})(e^{-i\boldsymbol{k}\times\boldsymbol{r}}-e^{-i\boldsymbol{k}\times\boldsymbol{r}'})\frac{1}{\beta\grave{o}(\boldsymbol{k})} \\ &= \frac{1}{2\beta\pi^2}\int d^2k\,\frac{1-\cos(\boldsymbol{k}\cdot(\boldsymbol{r}-\boldsymbol{r}'))}{\grave{o}(\boldsymbol{k})} \\ &= \frac{1}{2\beta\pi^2}\left(\int_0^{1/(\boldsymbol{r}-\boldsymbol{r}')}d^2k\,\frac{1-\cos(\boldsymbol{k}\cdot(\boldsymbol{r}-\boldsymbol{r}'))}{\grave{o}(\boldsymbol{k})}+\int_{1/(\boldsymbol{r}-\boldsymbol{r}')}^{\infty}d^2k\,\frac{1-\cos(\boldsymbol{k}\cdot(\boldsymbol{r}-\boldsymbol{r}'))}{\grave{o}(\boldsymbol{k})}\right)\end{aligned} \quad . (6.9)$$

The first term vanishes,

$$\int_0^{1/(\boldsymbol{r}-\boldsymbol{r}')}d^2k\,\frac{1-\cos(\boldsymbol{k}\cdot(\boldsymbol{r}-\boldsymbol{r}'))}{\grave{o}(\boldsymbol{k})}\le\int_0^{1/(\boldsymbol{r}-\boldsymbol{r}')}d^2k\,\frac{2}{\grave{o}(\boldsymbol{k})}\to 0\,. \tag{6.10}$$

The cos in the second term strongly oscillates, which does not provide leading terms, leaving us with only

$$\int_{1//(\boldsymbol{r}-\boldsymbol{r}')}^{\infty}d^2k\,\frac{1-\cos(\boldsymbol{k}\cdot(\boldsymbol{r}-\boldsymbol{r}'))}{\grave{o}(\boldsymbol{k})}=\int_{1//(\boldsymbol{r}-\boldsymbol{r}')}^{\infty}d^2k\,\frac{1}{\grave{o}(\boldsymbol{k})}\,. \tag{6.11}$$

We end up with

$$\left\langle(\phi(\boldsymbol{r})-\phi(\boldsymbol{r}'))^2\right\rangle=\frac{1}{\beta J\pi}\int_{1/(\boldsymbol{r}-\boldsymbol{r}')}^{\infty}dk\,\frac{1}{k}\,. \tag{6.12}$$

Note this integral has a logarithmic divergence, however, the divergence is artificial because it appears in the power of the physical property—the correlation function, we can cut it off at α and plug

$$\left\langle(\phi(\boldsymbol{r})-\phi(\boldsymbol{r}'))^2\right\rangle=\frac{1}{\beta J\pi}\log(\alpha(\boldsymbol{r}-\boldsymbol{r}')) \tag{6.13}$$

into (6.8), we have

$$c(\boldsymbol{r}-\boldsymbol{r}') = (\alpha(\boldsymbol{r}-\boldsymbol{r}'))^{-\frac{T}{2\pi J}}. \tag{6.14}$$

This means that any long-range ordering goes to zero at any nonzero temperature. We note that We also note that the conclusion is not restricted to the xy model. In fact, it is quite universal. Any classical system in two-dimension with a continuous symmetry will have a massless field by the Goldstone theorem. The fluctuation created by the Goldstone modes destroys the order in a similar fashion to what we have shown above—even if the corresponding Hamiltonians are much more complicated. This has been proven in many scenarios over the years. In the next section, we discuss our experimental confirmation on 2d magnet; and in the conclusion section, we will reconcile the contradiction between the Mermin-Wagner theorem and the experiment.

6.2 Fabrication and Identification of Ultrathin CrI_3

CrI_3 samples are exfoliated under an inert atmosphere in a glovebox with O_2, H_2O<0.5ppm. Using an all dry viscoelastic stamping technique[30], which has been introduced in Chapter 3, we sandwich the CrI_3 flakes between two layers of approximately 5nm graphite to prevent reaction with oxygen and moisture. The flakes can now be handled in the atmosphere for further studies. AFM of graphite encapsulated

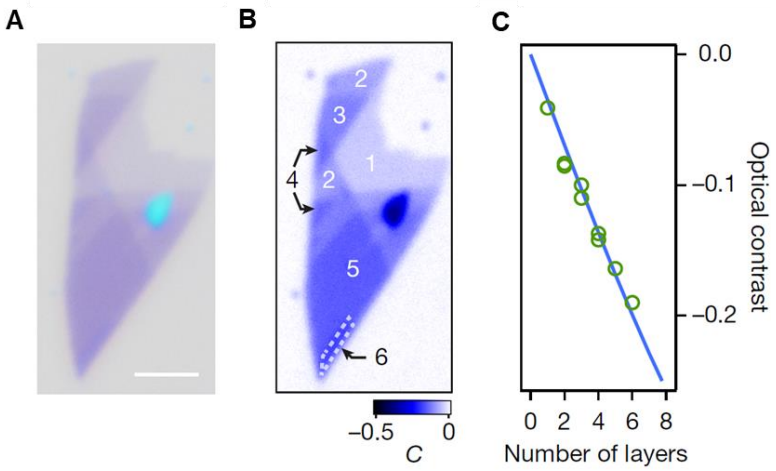

Figure 6.1. Optical RGB identification of fewlayer CrI_3 thickness. (A) Optical micrograph of a representative CrI_3 flake. **(B)** Calculated optical contrast map of the same flake with 631 nm optical filter. Scalebar, 3um. **(C)** averaged optical contrast of the steps of the sample with different numbers of layer (layer) fitted by a model based on Fresnel's Equations (solid line).

CrI_3 flakes were measured using a Bruker Dimension Edge atomic force microscope in tapping mode.

With reliable identification of CrI_3 thickness by AFM, we analyze the image of CrI_3 flake before encapsulation and establishes critical for identifying layer thickness based on the pixel red-green-blue (RGB) value. Figure 6.1A is an optical micrograph of a typical multi-step CrI_3 flake on a 285nm SiO_2 substrate, showing region ranging from 1 to 6 layers in thickness. Figure 6.1B shows an optical contrast map for the sample region illuminated by 631 nm light. The extracted optical contrast as a function of layer thickness is supported by an optical model based on the Fresnel Equation (Figure 6.1C, see also the detailed model in Appendix B1).

6.3 MOKE Measurement on Monolayer CrI_3

MOKE, i.e. magneto-optic Kerr effect, sometimes also referred to as surface magneto-optic Kerr effect, is the change to light reflected from a magnetized surface. Similar to the Faraday effect, which describes change to light transmitted through a magnetic material, the Kerr effect describes the changes to light reflected from a magnetic surface. These effects are a consequence of nonzero off-diagonal components of the dielectric tensor ò . As a consequence, the off-diagonal components give the magneto-optic material an anisotropic permittivity, and thus the speed of light is dependent on the direction of light propagation. In a specific type of Kerr effect, the polar Kerr effect, the light is directed at a magnetic surface with out-of-plane magnetization, the off-diagonal components cause rotation of the polarization angle of the incident light. The rotation can be then detected with an analyzer followed by a photodiode.

In Figure 6.2 we show a schematic of our setup, we used a continuous wave HeNe laser to measure the MOKE effect. A mechanical chopper provided intensity modulation at $f_1 = 800$ Hz that allows for accurate photodiode readout of laser intensity. The polarization of the light was initialized at

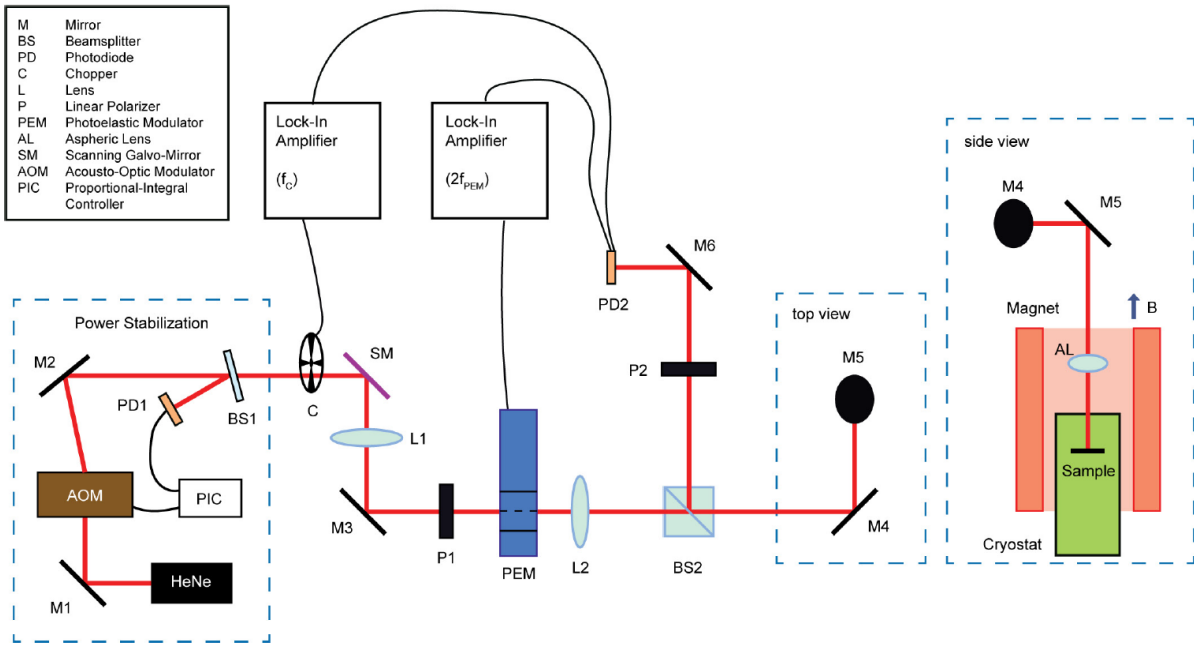

Figure 6.2. Schematic of MOKE setup. 633nm HeNe laser was power stabilized by a PID feedback system. A mechanical chopper and photoelastic modulator provide intensity and polarization modulation, respectively. Then we direct the beam into a closed-cycle cryostat at 15 K. A magnetic field is applied using a 7-T solenoidal superconducting magnet in Faraday geometry. The reflected beam passes through an analyzer onto a photodiode, where lock-in detection measures the reflected intensity (at f_1) as well as the Kerr rotation (at f_2).

45 degrees off the vertical axis and then sent through a photoelastic modulator (PEM) at $f_2 = 50.15$ kHz with a vertical axis. The PEM added a dynamic phase along its axis of the PEM such that the total polarization was varied between linear–left circular polarization (LCP)–linear in a perpendicular direction–right circular polarization (RCP) in a single period. If the light passes through an analyzer oriented in the same direction of the PEM axis, the signal detected by the photodiode afterward will have only the DC component. However, if the light reflects off a magnetic surface before it is sent to the analyzer, the rotation of the polarization causes an AC component at $2f_2 = 100.30$ kHz to appear in the photodiode signal. The amplitude of such AC component, which can be read out by a lock-in amplifier, is then normalized by laser intensity readout by the second lock-in amplifier locked at chopper frequency, to obtain an intensity independent quantity that characterizes rotation to the polarization. This quantity is proportional

to the off-diagonal element in the dielectric tensor, which can then serves as a measurement of magnetic order of the targeted substance[57].

As such, we conducted the MOKE measurement as a function of magnetic field on CrI_3 at 15K. In figure 6.3a, we show the MOKE signal from a thin bulk flake of CrI_3. The observed hysteresis loop and the remnant θ_K at zero magnetic field $\mu_0 H = 0$ T are hallmarks of ferromagnetic ordering, consistent with its bulk ferromagnetism with out-of-plane magnetization.

Remarkably, measurements on monolayer CrI_3 reveal that the ferromagnetic ordering remains in the monolayer limit. Figure 6.3b shows θ_K as a function of magnetic field for monolayer CrI_3. A single hysteresis loop centered around zero field demonstrates out-of-plane magnetization, which

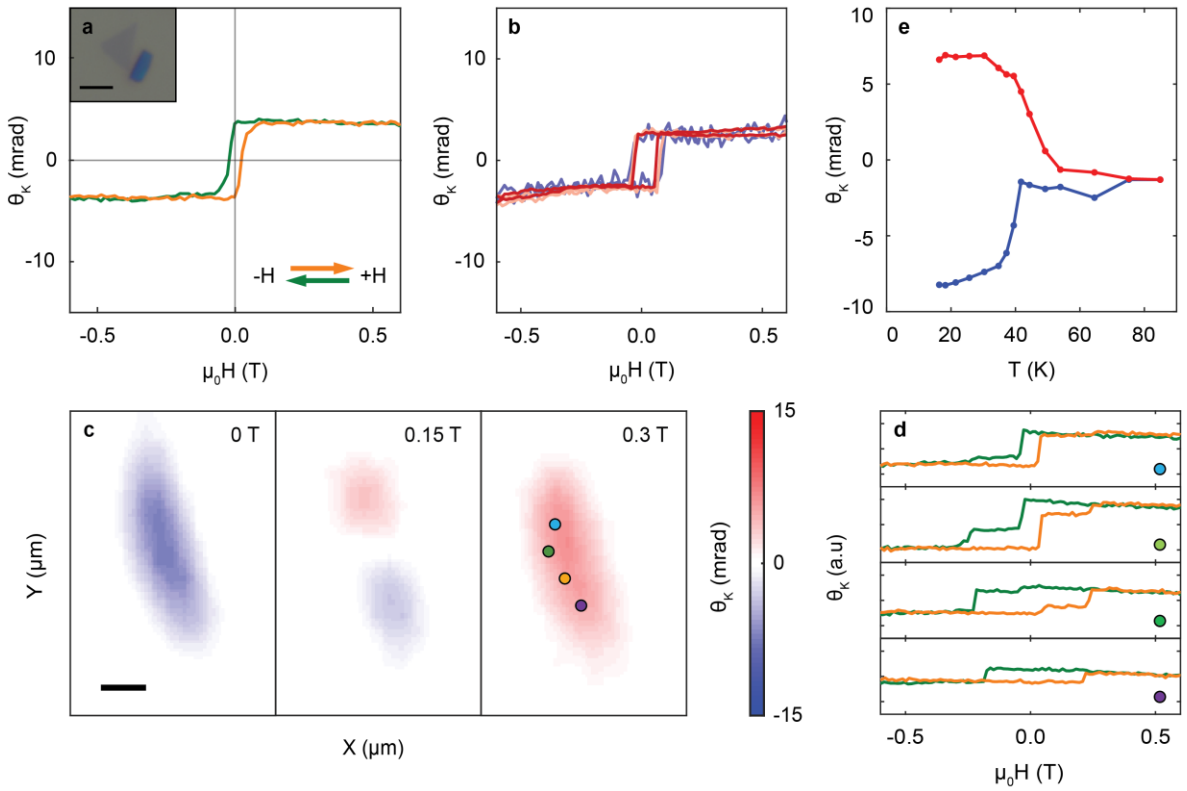

Figure 6.3. MOKE measurements of monolayer CrI_3. a, Polar MOKE signal for a CrI_3 monolayer. Inset shows the optical image of an isolated monolayer. The scale bar is 2 μm. **b**, Power dependence of MOKE signal taken at incident powers of 3 μW (blue), 10 μW (pink), and 30 μW (red). **c,** MOKE maps at $\mu_0 H$ = 0 T, 0.15 T, and 0.3 T on a different monolayer. The scale bar is 1 μm. **d,** θ_K vs. $\mu_0 H$ sweeps taken at four points marked by dots on the $\mu_0 H$ = 0.3 T map in **c. e**, Temperature dependence of MOKE signal with the sample initially cooled at $\mu_0 H$ = 0 T (blue) and 0.15 T (red).

implies Ising ferromagnetism. This effect is independent of excitation power, as shown in Figure 6.3b. In the following, all data are taken with 10μW excitation power. We have measured a total of 12 monolayer samples, which show similar MOKE behavior with consistent remnant θ_K values of about 5 ± 2 mrad at $\mu_0 H = 0T$. The coercive field ($\mu_0 H_c$), which is approximately 50 mT for the sample in Figure 6.3a, can vary between samples owing to the formation of domain structures in some samples. Figure 6.3c shows spatial maps of θ_K for another monolayer, taken at selected magnetic field values. After cooling the sample from above T_C at $\mu_0 H = 0T$, the entire monolayer is spontaneously magnetized (in blue, negative MOKE signal). As the field is increased to 0.15 T, the magnetization in the upper half of the flake switches direction (in red, positive RMCD signal). As the field is further increased to 0.3 T, the lower half of the monolayer flips and the entire flake becomes spin up, parallel to $\mu_0 H$. This observation of micro-scale lateral domains suggests diverse values of coercivity in each domain. Indeed, magnetic field sweeps (θ_K versus $\mu_0 H$) taken at discrete points ranging across both domains (Figure 6.3d) show the difference in coercive field between the upper and lower half of the monolayer. Sweeps taken only on the upper domain (marked by a blue circle) show a much narrower hysteresis loop (about 50 mT) than sweeps from spots on the lower domain (orange and purple circles, about 200 mT). When the beam spot is centered between the two domains, contributions from both domain can be seen in the resulting hysteresis loop (green circle), which is a consequence of the approximately 1μm beam spot illuminating both domains.

To determine the Curie Temperature T_C, we perform zero-field-cooled sweeps in which awe measure θ_K while cooling the sample in zero field. After warming up to a temperature well above the Curie Temperature (90K), we conducted zero field-cooled measurement upon cooling down in

the presence of a small external magnetic field 0.15T. Thermomagnetic irreversibility can be observed below T_C, at which point the zero-field-cooled sweep and the field-cooled sweep diverge, as shown in Figure 6.3e. We measured the average T_C for the sample to be 45K, lower than that of bulk CrI_3.

6.4 Layer Dependent Magnetic Order of Fewlayer CrI_3

The layered structure of CrI_3 provides a unique opportunity to investigate ferromagnetism as a function of layer number. Figure 6.4 a, b shows MOKE signal for both monolayer and bilayer CrI_3 devices. A remarkable observation is that the bilayer CrI_3 exhibits significant difference in magnetic behavior from the monolayer. For all bilayer measured, the MOKE signal is strongly suppressed, with θ_K approaching zero between field values ±0.65T. This observation implies a compensation for the out-of-plane magnetization compensation mechanism, which is likely that bilayer CrI_3 consists of two antiferromagnetic aligned ferromagnetic monolayers. At around

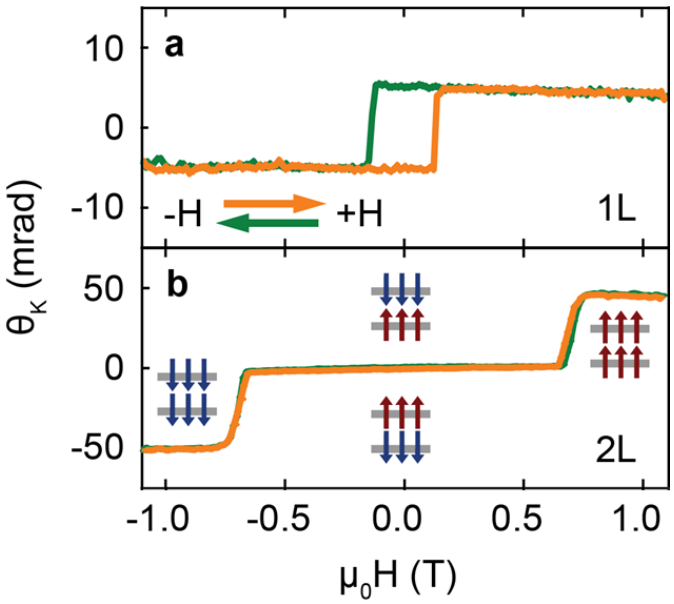

Figure 6.4. Layer-dependent magnetic ordering in atomically-thin CrI_3. (a), MOKE signal on a monolayer CrI_3 flake, showing hysteresis in the Kerr rotation as a function of applied magnetic field, indicative of ferromagnetic behavior. **(b)**, MOKE signal from a bilayer flake of CrI_3 showing zero Kerr rotation for applied fields less than ±0.65 T, suggesting antiferromagnetic behavior.

±0.65T, two sharp jumps mark a sudden restoration of out-of-plane magnetization, which can be understood as an external magnetic field driven transition from antiferromagnetic ordering to a fully spin polarized state. The sharpness of the transition is a consequence of strong magnetocrystalline anisotropy in CrI_3, such that the intermediate state with spin rotation into in-plane direction is metastable.

The revealing of AFM interlayer coupling is surprising since the bulk CrI_3 has long been known as a ferromagnetic material. The contradiction has not yet been well explained. Our group has been actively studying the properties of CrI_3 with various methods, and a recent discovery revealed a piece of critical information that might be relevant. It's been known that bulk CrI_3 is monoclinic in at room temperature, and it undergoes a phase transition ~180K from monoclinic to rhombohedral[42]. We found that such transition is missing for fewlayer CrI_3 layers, suggesting that the fewlayer CrI_3 possess a different stacking order from its bulk counterpart. The stacking order influences atomic orbital alignments between neighboring layers thus is crucial in determining the interlayer exchange interaction. However, it is necessary for future studies such as X-ray diffraction to provide more information on the stacking order of fewlayer CrI_3, and computational simulation might also be beneficial to unravel the relation between stacking order and interlayer magnetic interactions.

6.5 Conclusion

At the end of this chapter, we would like to revisit the Mermin-Wagner theorem we introduced at the beginning of this chapter. It is natural to ask how to fill the gap between contradicting results of our experimental and the theoretical prediction coherently. First, we note that the Mermin-Wagner theorem was raised in the 60s of the last century, far before the first 2d materials graphene was born in this world. In fact, Mermin-Wagner theorem have been successful in studies on

magnetic thin films, in which researchers have observed decay of magnetism as the thickness went down to several atomic thick[58], which corroborates the Wagner-Mermin theorem. The exemption of magnetic 2d materials from the Mermin-Wagner theorem relies on strong magnetocrystalline anisotropy. In a strong anisotropic system, a Heisenberg model description of magnetism becomes invalid. Rather, Ising model where the spin is tentative to take either spin up or spin down state is more suitable for describing strong anisotropic systems. In this sense, the CrI_3 is called "Ising magnet". Starting with the discovery of the CrI_3, the searching for more 2d magnetic materials will never stop. In addition to CrI_3, researchers have started to actively explore several other 2d magnets, including $FePS_3$[59], $Cr_2Ge_2Te_6$[60], Fe_3GeTe_2[61, 62], VSe_2[63] and $MnSe_x$[64], which exhibit a diversity of magnetic orderings and electronic structures. The Mermin-Wagner theorem is going to be very instructive in searching for more 2d magnet, which guides the researchers toward the right direction—the materials with strong anisotropy.

Chapter 7. LIGAND FIELD HELICAL LUMINESCENCE IN CrI_3

In the last Chapter, we showed that the CrI_3 had been added to the 2d family with a special identity—magnetic 2d materials. In this chapter, we present further exploration which found that in addition to magnetism, CrI_3 also possess fascinating luminescence properties. Contrary to many typical 2d materials, whose luminescence originate from the Wannier-Mott excitons, the CrI_3's luminescence is a result of Frenkel excitons. This work is reprinted from Kyle L. Seyler, **Ding Zhong**, Dahlia R. Klein, Shiyuan Gao, Xiaoou Zhang, Bevin Huang, Efrén Navarro-Moratalla, Li Yang, David H. Cobden, Michael A. McGuire, Wang Yao, Di Xiao, Pablo Jarillo-Herrero, Xiaodong Xu, Ligand-field helical luminescence in a 2D ferromagnetic insulator. Nature Physics, 2018. 14(3): p. 277-281[65].

7.1 SPONTANEOUS CIRCULARLY-POLARIZED PL FROM CrI_3

We prepared monolayer CrI_3 on sapphire substrates by mechanical fabrication of bulk crystals. Using the optical contrast method we introduced in chapter 6.2, we identify the layer thickness of CrI_3. Adapting to sapphire substrate, the parameter is tuned to be ~0.035 and ~0.07 at 631nm for monolayer and bilayer CrI_3.

For the PL experiments we excited with a linearly polarized HeNe laser at 1.96eV and analyze the circularly polarized PL components. The laser was focused to a ~1 μm spot diameter. A low power of 10μW was used to avoid sample heating and degradation. In the collection path, a confocal pinhole was added to ensure the localization of signal received. To achieve circular polarization excitation and detection, we used linear polarizers and achromatic near-infrared half waveplates and quarter waveplates.

We first measured the monolayer CrI_3 PL at 75K, above the Curie temperature of 45K[50]. As shown in Figure 7.1b, we detected emission at ~1.1eV with a full-width at half-maximum of about 180meV. The color represents the polarization of detection, as indicated in the legend of the figure.

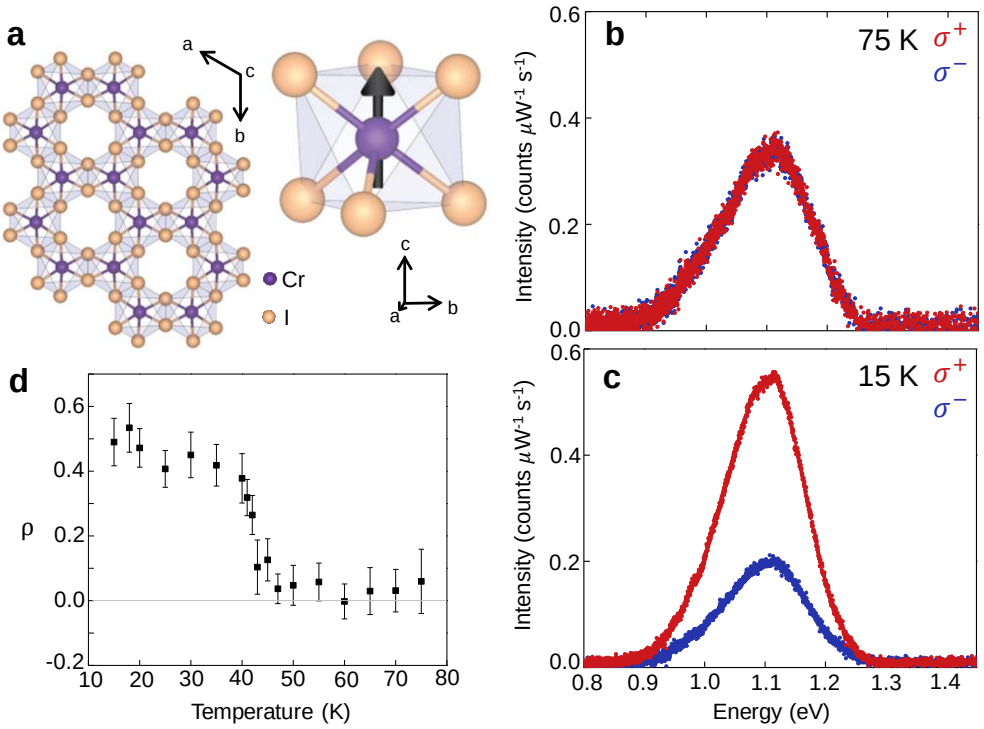

Figure 7.1. Spontaneous circularly polarized luminescence from monolayer CrI_3. (a) Top view of the crystal structure of CrI_3 (left) and side view (right) depicting single Cr site with an arrow representing its out-of-plane magnetic moment. **(b)** Photoluminescence (PL) spectrum for σ^+ (red) and σ^- (blue) circularly polarized PL from a monolayer at 75 K. The excitation is linearly polarized. **(c)** Same as (b), but at 15 K. **(d)** Temperature dependence of the degree of PL circular polarization (ρ) at 0 T from 75 to 15 K. Error bars show the standard deviation of the polarization at the peak. No external magnetic field was applied while acquiring the data in Figure 7.1 a-d.

Since the absence of magnetic field and time reversal symmetry, the two curves are indistinguishable.

Remarkably, on cooling to 15K, in the absence of a magnetic field, we see a diverge in the intensity of σ^+ and σ^- in Figure 7.1c. Defining the PL polarization $\rho = \frac{I_+ - I_-}{I_+ + I_-}$, where $I_\pm$ is the peak intensity of $\sigma^\pm$ PL, calculated by averaging 100 points about peak center, we find $\rho \approx 0.45$. This observation indicates breaking of time reversal symmetry. Since no external source (such as light

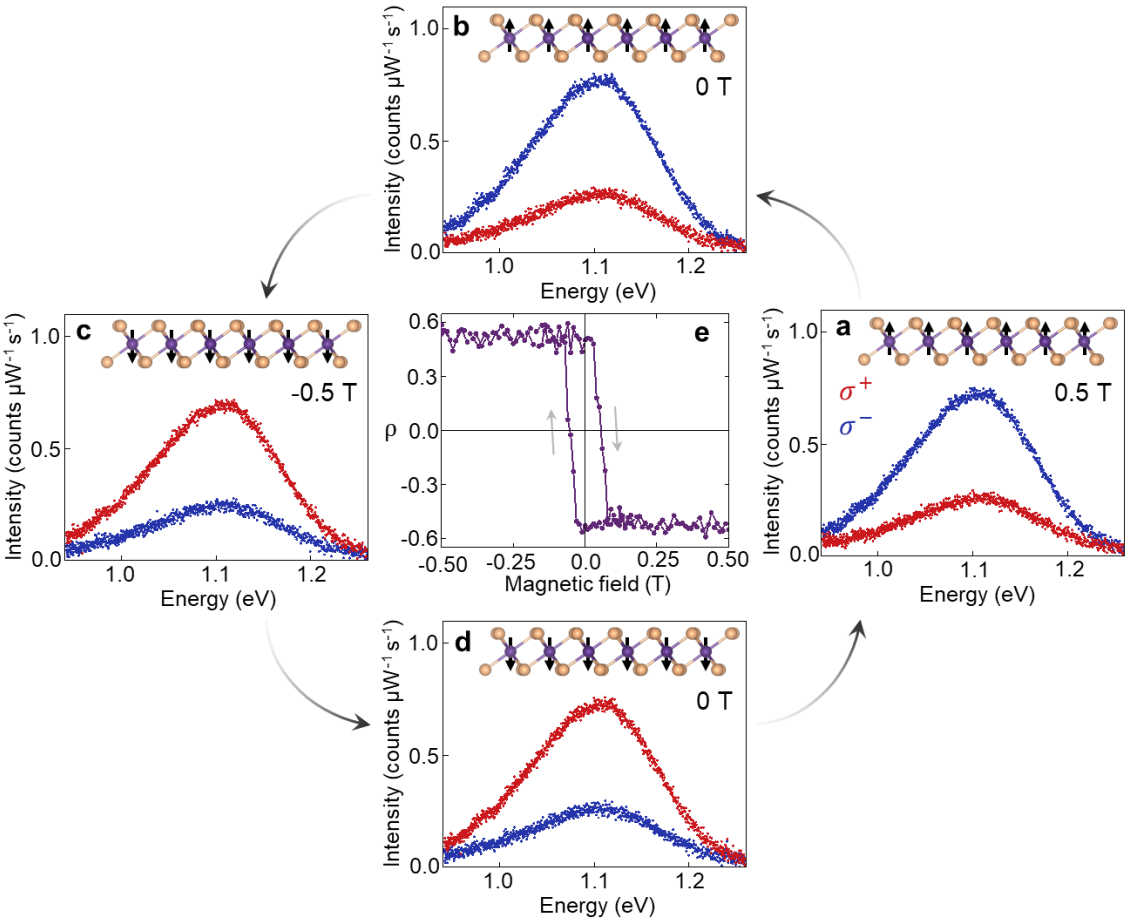

Figure 7.2. Photoluminescence from monolayer CrI_3 in an applied magnetic field. Sequence of PL spectra for σ^+ (red) and σ^- (blue) circular polarization components, acquired at 15 K under linearly polarized excitation. **(a)** 0.5 T (increasing from 0 T), **(b)** 0 T (decreasing from 0.5 T), **(c)** -0.5 T (decreasing from 0 T), and **(d)** 0 T (increasing from -0.5 T). The curved arrows indicate the magnetic field sweep direction, and the insets depict the magnetization direction relative to the lattice. **(e)** Circular polarization (ρ) as a function of applied field over one full cycle. Gray arrows show the sweep direction of the applied field.

polarization, applied magnetic field) breaks the time-reversal symmetry, it is attributed to the spontaneous magnetization of CrI_3 itself. In Figure 7.1d, we show the temperature dependence of ρ, where we see the onset of ρ at ~45K, right where the Curie Temperature is. The result is a reconfirming that ρ is associated with the magnetic order of CrI_3.

7.2 Field Dependent Circularly-Polarized PL

Since the magnetic state is associated with ρ, it is interesting to explore the effect of applied out-of-plane magnetic field. Figure 7.2a shows the circularly polarized PL spectra at 0.5T. Here the

polarization is reversed relative to Figure 7.1c, which means the applied field has flipped its magnetization. If the field is then lowered to 0T, the spectra remain unchanged (Figure 7.2b). Keep sweeping the field to -0.5T, we see that the PL returned to its original state with a stronger σ^+ than σ^- (Figure 7.2c). This state is in turn preserved when the field is returned to zero (Figure 7.2d). We show ρ over a cycle of magnetic field in Figure 7.2e, where the observed hysteresis loop is clearly the hallmark of ferromagnetic behavior.

These results unambiguously demonstrate that the helicity of CrI_3 PL is determined by its magnetic ordering. Figure 7.3a-c presents the circular polarization-resolved PL from a bilayer of CrI_3 at 15K. at magnetic field -1T, 0T and 1T respectively. We see strong circularly polarized PL at ± 1T (Figure7.3 a,c) while there is no net circular polarization at zero field, as shown in Figure 7.3b, if we continuously sweep the magnetic field between ± 1.2T, we can see a full picture in which the polarization ρ is negligible between ± 0.65T and jumps abruptly to a value of -0.5 above 0.65T and +0.5T below -0.65T. This magnetic field dependence forms a close parallel to the MOKE measurement of bilayer hysteresis curve in the last chapter. This consistency reinforces the interpretation that at low fields, bilayer CrI_3 consists of two antiferromagnetically aligned ferromagnetic monolayers.

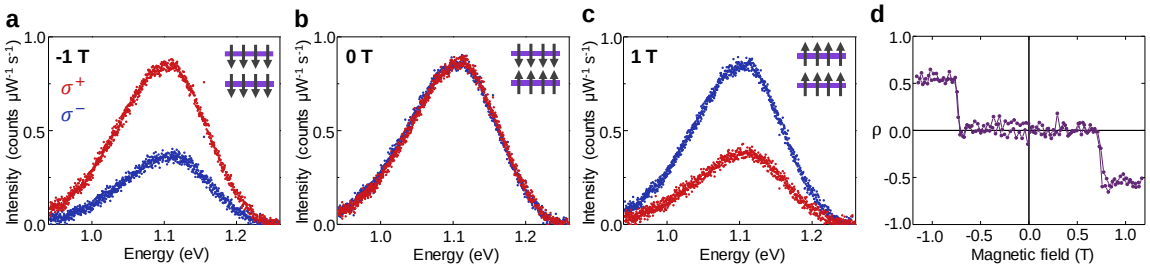

Figure 7.3. Bilayer luminescence reveals antiferromagnetic ground state. PL spectrum of a bilayer sample for σ^+ (red) and σ^- (blue) circular polarization and linearly polarized excitation acquired at 15 K at magnetic fields of -1 T **(a)**, 0 T **(b)**, and +1 T **(c)**. The inset figures depict the inferred magnetization pattern of the bilayer. It should be noted that at 0 T the net magnetization is zero, but the exact spin orientation within each layer is unknown. **(d)** Circular polarization (ρ) as a function of magnetic field. Data points for increasing and decreasing magnetic field overlap to within uncertainty. The data in (a)-(c) are from a bilayer on sapphire while the data in (d) are from a bilayer on SiO_2. Their behavior is consistent.

7.3 The Origin of The PL

What is the origin of the luminescence in atomically thin CrI_3? In well studied 2D semiconductors, such as WSe_2, the photo-response can be described as band-to-band transitions with strong excitonic effect. As we discussed in Chapter 2.4, these excitons are Wannier-Mott excitons that has a radius larger than lattice spacing. In CrI_3, however, the 3d electrons are much more spatially localized. Thus to understand an optical response, a molecular orbital approach is more suitable.

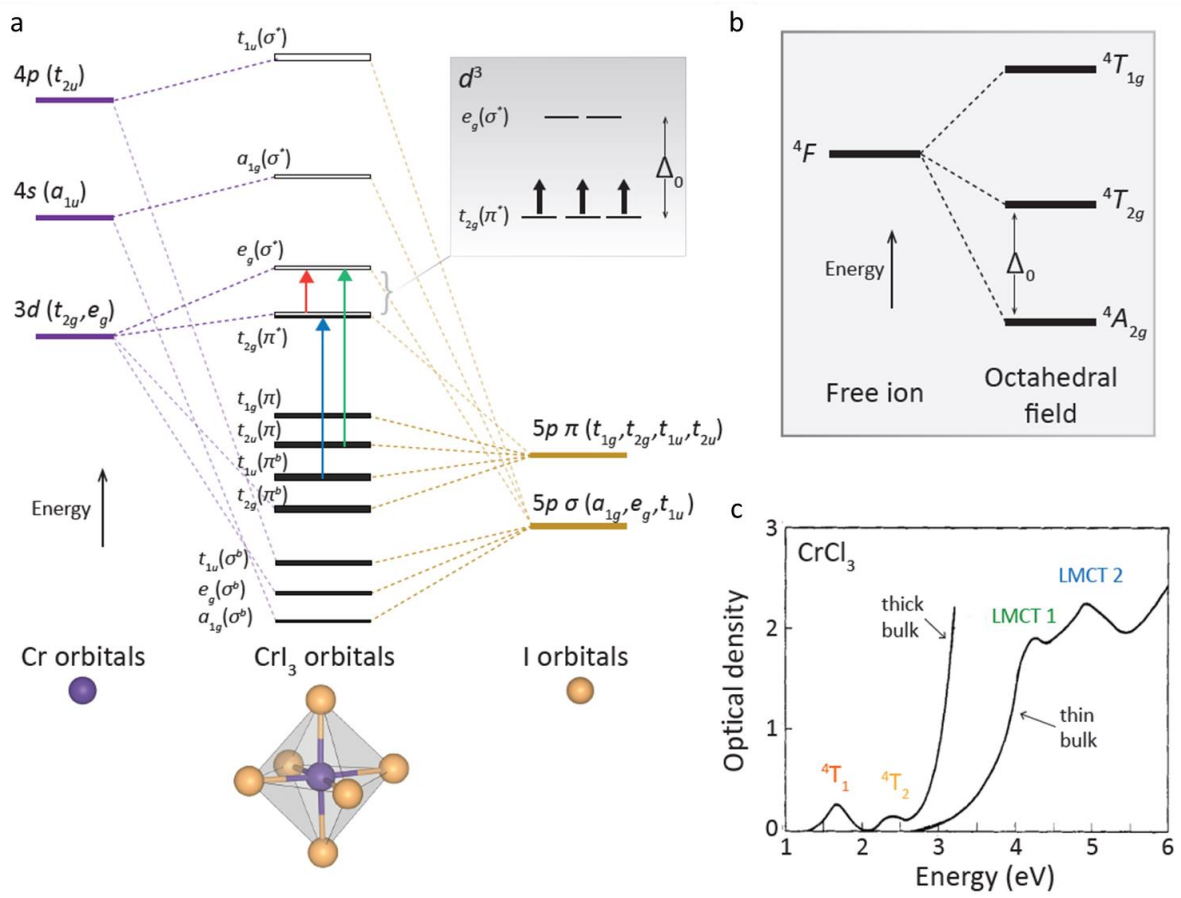

Figure 7.4. Chromium Trihalides energy levels. (a). Molecular orbital energy diagram for CrI_3. The bonding and anti-bonding orbitals are denoted by "b" superscripts and asterisks, respectively. The orbitals from $a_{1g}(\sigma^b)$ through $t_{1g}(\pi)$ are completely filled by the iodine electrons. Three spin-aligned electrons occupy $t_{2g}(\pi^*)$ in the ground state. (see inset diagram—ligand field splitting Δ_0 is given by difference between $t_{2g}(\pi^*)$ and $e_g(\sigma^*)$). The effect of spin-orbit coupling is not included and the relative energy space are not quantitative. The red arrow shows a *d-d* transition. The green and blue arrows show two of the possible LMCT transitions. Note that the transition to $t_{2g}(\pi^*)$ involves a promotion of an electron with spin anti-parallel to the d^3 electrons. **(b)** Splitting of the free-ion term ^4F into its octahedral irreducible representations. **(c)** Example absorption spectrum for CrCl3 showing the ligand-field *d-d* and LMCT transitions. Panel c is reproduced from I. Pollini et al. "Intrinsic optical properties of $CrCl_3$". *Phys. Stat. sol.*(*b*) 41.2 (1970)

In general, to interpret optical spectra of bulk transition metal halides[66, 67], ligand field theory is used, which predicts intra-atomic *d-d* transitions and higher energy charge-transfer transition within metal-ligand complexes. We now present evidence that these intrinsic localized photo-excitations dominate 2D CrI_3.

Figure 7.4a shows a molecular orbital energy diagram for CrI_3, which shows the influence of the iodine ligand field on the 3d electrons in Cr^{3+}[68, 69]. The orbitals from $a_{1g}(\sigma^b)$ through $t_{1g}(\pi)$ are occupied by the iodine electrons. Leaving 3 pin-aligned electrons from Cr to occupy the $t_{2g}(\pi^*)$ level. The exchange interaction between the unpaired electrons between neighboring Cr sites give rise to the ferromagnetic intralayer order and lead to a net magnetic moment of ~3.1 μ_B /Cr. Even though $t_{2g}(\pi^*)$ is partially filled, CrI_3 forms an energy gap and becomes a Mott Insulator due to strong on-site repulsion. It is possible to excite electrons between $t_{2g}(\pi^*)$ and $e_g(\sigma^*)$ electrons, so-called ligand field transitions, or $d-d$ transitions.

Considering the electronic configurations in the ground and excited states can help us understand the optical excitations. The available energy states are determined by the effect of octahedral symmetry reduction on the free-ion terms. For electrons configurations in the CrI_3 in the $t_{2g}(\pi^*)$ and $e_g(\sigma^*)$ with 3 electrons, the ^4F free-ion ground state split into three levels, given by their irreducible representations: the $^4A_{2g}$ ground state and $^4T_{2g}$ and $^4T_{1g}$ excited state configuration (4 is the spin multiplicity), as shown in Figure 7.4b. Therefore, optical excitations are allowed from $^4A_{2g}$ to $^4T_{2g}$ and $^4T_{1g}$. Due to octahedral symmetry, the configurations each have even parity and the $d-d$ transitions are thus electric-dipole forbidden by the Laporte parity selection rule. However, as we will see, both lattice vibrations and the reduced crystal symmetry of the lattice

can make the transition weakly allowed. Since g is the notation for “even parity”, we will leave out g in future reference to these electron configurations.

Another optically allowed transition is the transition from the iodine character bonding orbitals into the unoccupied Cr antibonding orbitals. Two possibilities are from $t_{1u}(\pi^b)$ to $t_{2g}(\pi^*)$ and from $t_{2u}(\pi)$ to $e_g(\sigma^*)$, which are shown in figure 7.4a by blue and green arrows. These are knowns as ligand-to-metal charge transfer (LMCT) transitions, which are parity allowed and thus with higher oscillator strength. This picture will give a qualitative understanding of the different electronic transitions, but we emphasize that other important effects, such as spin-orbit coupling, Jahn-Teller distortions, and the Zeeman field should be considered in future first-principals calculation for a better understanding.

We reiterate that the monolayer PL intensity is linear in excitation power, as shown in Appendix C1. Taken together with the tight link between the PL helicity and layer-dependent magnetic phases, this rule out the possibility that the PL is from defect-bound excitons, which tend to saturate at higher excitation intensity.

To investigate the electronic response more broadly, we measured the differential reflectance of monolayer CrI_3 on sapphire. We spatially filtered a tungsten halogen lamp through a pinhole and focus the beam into a ~3μm spot size. The reflected light from CrI_3 was deflected with a beamsplitter and detected with a Si CCD or In GaAs array, which enabled measurements from 1~3eV. The differential reflectance was calculated by subtracting and normalizing the CrI_3 by the reflectance of the bare sapphire substrate.

As shown in Figure 7.5a, there’s a weak peak near 1.5eV along with stronger features around 2eV and 2.7eV. Using the ligand-field framework, we can attribute the 2.7eV peak and the strongest two peaks near 2eV to dipole-allowed ligand-to-metal-charge-transfer (LMCT) transitions

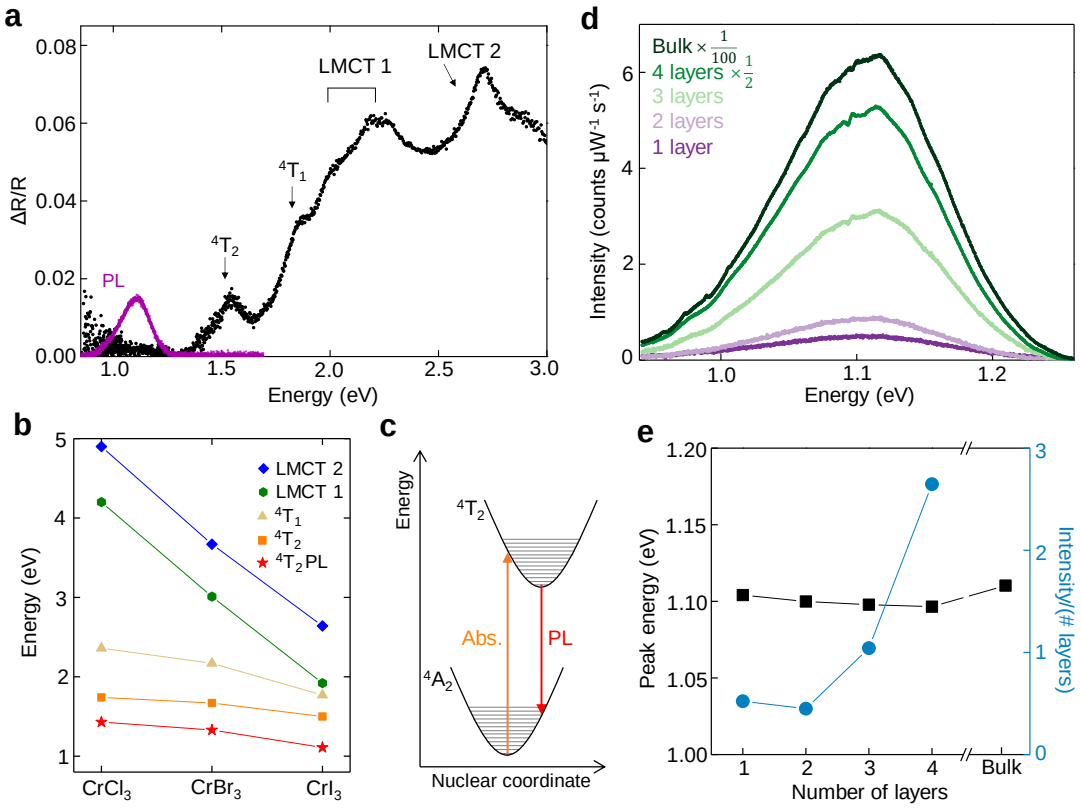

Figure 7.5. Reflection spectrum and thickness-dependent PL. (a) Differential reflection spectrum of monolayer CrI_3 (black) and overlaid PL spectrum (purple). See text for discussion of labelled peak assignments. **(b)** Energies of the corresponding peaks in bulk $CrCl_3$, $CrBr_3$, and CrI_3. The data for $CrBr_3$ and $CrCl_3$ are compiled from Refs. 69, 73-75. **(c)** Configurational coordinate diagram in the harmonic approximation for the observed ligand-field $^4T_2$ absorption and PL. The horizontal lines represent vibrational levels. The calculated Huang-Rhys factor is ~10. **(d)** Layer dependence of the PL spectra at 15 K and zero magnetic field. Note that the 4-layer-thick and bulk spectra have been divided by a factor of 2 and 100 respectively. The small features near 1.08 eV are due to a slight artefact of the grating which could not be corrected. **(e)** Peak energy (black) and PL intensity (counts μW^{-1} s^{-1}) normalized by number of layers (blue) for different thicknesses. The peak energy is calculated by weighted average using the spectra in **(d)**.

between the iodine 5p orbitals and the Cr^{3+} 3d orbitals. The 1.5eV transition has not been discussed before in literature. As we described in the previous section, the approximate octahedral symmetry of the iodine ligands around the Cr^{3+} site, the d^3 configuration (^4F term) in isolated Cr^{3+} splits into an $^4A_2$ ground state and $^4T_2$ and $^4T_1$ excited states of the t_{2g} and e_g orbitals in CrI_3. We assign the 1.5eV peak to the lowest energy transition between these levels, from $^4A_2$ to $^4T_2$. Despite being electric-dipole forbidden by the parity selection rule, d - d transitions can become weakly allowed by mixing with odd parity states, such as produced by phonons. In addition, the trigonal field of

nearest neighbor Cr atoms eliminates the local inversion symmetry of each Cr site, allowing the weak d-d transition to happen. From the deferential reflection data, The $^4T_2$ absorbance was determined as $\frac{1}{4}(n^2-1)\frac{\Delta R}{R} \approx 0.7\%$ [70], where $n \approx 1.76$ is the ordinary refractive index of sapphire at for 1.5eV light. Comparing this value with the absorbance for the A and B excitonic resonances in monolayer semiconducting transition metal dichalcogenides (such as MoS_2), we find that the former is an order of magnitude weaker. This property underscores the weakly allowed parity-forbidden nature of the d-d transition.

These assignments of the reflection features is consistent with the result of prior experiments and recent calculation on bulk $CrCl_3$ and $CrBr_3$[71, 72]. To connect these with CrI_3, in Figure 7.5b, we plot the absorption peak energy of bulk CrI_3 that we measured against those of $CrCl_3$ and $CrBr_3$ from previous studies[69, 73-75]. The relationship between the optical spectra of these trihalides then becomes clear. The LMCT transitions has large energy shift from chloride to iodide, which is the consequence of its charge transfer origin. On the other hand, the d-d transitions exhibit weaker dependence on the ligand.

We can now begin to understand the origin of PL monolayer CrI_3. The clear correlation between the three Cr trihalide compounds in the energies of the lowest absorption peak and PL implies that the monolayer CrI_3 PL originates from $^4T_2$ to $^4A_2$ d-d transition. The ~430meV Stokes shift between the PL and 1.5eV reflection peak is a consequence of the Franck-Condon principle and strong electron-lattice coupling. In Figure 7.5d, we display the layer dependent PL of which the intensity and peak energy is extracted in Figure 7.5e. It is seen that the PL intensity per layer increases with increasing thickness, suggesting that the d-d relaxation process is affected by interlayer or substrate interactions. Furthermore, we can estimate the emission intensity at the energy E by the following equation:

$$I(E) = \frac{e^{-S} S^{p}}{p!}(1 + S^{2}\frac{e^{-\hbar\omega/kT}}{p+1}),\ p = \frac{E_0 - E}{\hbar\omega}. \quad (7.1)$$

Here E_0 is the energy of the zero-phonon line, S is the Huang-Rhys parameter, k is the Boltzmann constant, $\hbar\omega$ is the effective phonon energy involved in the emission process. Using $T = 15\,\mathrm{K}$ and $E_0 = 1.312\,\mathrm{eV}$ in Eq (7.1), we achieve a good fit to the PL spectrum with $S \approx 10$ and $\hbar\omega \approx 24\,\mathrm{meV}$, as shown in Figure 7.5c. Furthermore, if we plot the corresponding absorption line shape using the same parameters as the PL fit, we find pretty good overlap with the experimental peak. This agreement is further evidence that they share the same origin, which is the transition between $^4A_2$ and $^4T_2$ excited states. One might think the Stokes shift is large here. In fact, it's reasonable for $^4T_2$ transitions in Cr^{3+} octahedral complexes. For example, previous literature has reported Huang-Rhs parameters of 3.6 and 6.7 in $CrCl_6^{3-}$ and $CrBr_6^{3-}$ complexes[76]. Since larger metal-ligand distance typically increases Huang-Rhys parameter, a large Huang-Rhys parameter in CrI_3 due to relatively large Cr-I bond lengths can be expected.

As we stated above, the energy discrepancy between $^4T_2$ and $^4A_2$ correspond to the ligand field splitting. Such ligand field splitting can be estimated by

$$\Delta_0 = 3e_\sigma - 4e_\pi, \quad (7.2)$$

where e_σ and e_π are the angular overlap model parameters for σ and π bonding, which can be obtained from previous literature to be $e_\sigma = 4100\,\mathrm{cm^{-1}}$ and $e_\pi = 670\,\mathrm{cm^{-1}}$ [77]. These values lead us to an estimated ligand-field splitting of ~1.2eV, which is a good agreement with experiment.

We also have some notes on the weakly allowed d-d transitions. For O_h symmetry, the phonon modes that can enable the d-d transition are odd parity modes, which are t_{1u} and t_{2u}. This strong vibronic mixing precludes the formation of a separate phonon sideband in the spectra. In the Cr

trihalides, the trigonal arrangement of nearest neighbor chromium atoms distorts the octahedral field and thus provide an additional mechanism for intensifying d - d transitions.

In summary, the emergent PL in CrI_3 creates new opportunity to study and control light-field spectra in 2d limit with magnetic ordering. Our results demonstrated that the PL experiment can serve as an important probe of magnetic order in atomically thin CrI_3. Nonetheless, the underlying mechanism is still unclear at this point. The direction is new and deserve more future experiments and theoretical simulations for understanding the thickness and polarization dependence and the charge-transfer and ligand-field transitions. Our work expands the horizon of light-matter interaction in 2D limits, by demonstrating the Frenkel exciton from a 2d material. We preview CrI_3 to be a fascinating atomically thin magnetic insulator for van der Waals heterostructure applications. For example, existing knowledge suggests that CrI_3 to be a great candidate for exploring spin-dependent tunneling phenomena or transporting phenomena; harvesting the proximity effect in CrI_3 by serving CrI_3 as a magnetic substrate is another promising direction that deserves more work into.

Chapter 8. Layer Resolved Proximity Effect

8.1 From WSe_2/Thin Bulk CrI_3 to WSe_2/Fewlayer CrI_3

At the interface formed by a magnetic and non-magnetic material, the magnetic order can drastically influence the properties of the nonmagnetic component[78, 79], which can expose new functionalities absent from the individual materials. This proximity effect is usually short-ranged due to the finite extension of the electronic wavefunctions across the interface. With the recent arrival of van der Waals (vdW) magnets[50, 59, 61-64, 80-89], there may be new opportunities to engineer magnetic proximity effects. These opportunities arise from the flexibility to create vdW heterostructures with an atomically sharp interface, as well as the unique properties of both magnetic and nonmagnetic 2D materials[88, 90-96].

In Chapter 6, we observed emergent phenomena in heterostructures formed by monolayer WSe_2 and magnetic insulator CrI_3 (Fig. 1a)[43, 97]. Monolayer WSe_2 is a non-magnetic semiconductor with coupled spin-valley physics[98]. By interfacing it with CrI_3, the proximity-induced exchange field gives rise to spontaneous valley excitonic Zeeman splitting. In addition, a type-II band structure forms at the WSe_2/CrI_3 heterostructure interface with the bottom conduction band in CrI_3. Since the relevant bands in CrI_3 are spin-polarized, this type-II band structure facilitates spin-dependent charge transfer between WSe_2 and CrI_3 (Fig. 1b), leading to large spontaneous exciton valley-spin polarization. However, for 10 nm thick CrI_3, as studied in Chapter 6, the magnetic structure is too complicated to unravel several fundamental issues. For instance, the magnetic proximity effect involves both real and virtual electron hopping at the heterostructure interface; it is unclear how the two hopping processes manifest at the heterostructure interface and beyond. It remains elusive how the observed valley dynamics in WSe_2 connect to the magnetic states in CrI_3. Such knowledge is important for understanding the magnetic properties of CrI_3 (e.g., magnetic

domains) and engineering magnetic vdW heterostructures to harness the proximity effect for new functionalities.

In this chapter, we report a magneto-optical spectroscopy study of the proximity effect in heterostructures formed by monolayer WSe_2 with either bilayer or trilayer CrI_3. We employed polarization-resolved magneto-photoluminescence to measure the effect of CrI_3 proximity on the valley-spin dynamics of WSe_2. Combined with reflective magnetic circular dichroism (RMCD) experiments, which measure the magnetic order of CrI_3, we show that spin-dependent charge transfer between WSe_2 and CrI_3 is dominated by the interfacial CrI_3 layer magnetization, while the proximity exchange field has a strong dependence on the layered magnetic structure as a whole. Building on this layer-resolved effect, we used monolayer WSe_2 as a magnetic sensor to probe the magnetic domains in bilayer CrI_3, which is a challenge for conventional techniques, such as RMCD, due to the vanishing magnetization of the AFM order. At zero magnetic field, we uncovered both reconfigurable and pinned layered AFM domain walls. Near the magnetization-flip transitions, we observed the evolution of AFM/FM domain walls as a function of the magnetic field.

8.2 METHOD

In this study, a couple of WSe_2/bilayer CrI_3 and WSe_2/trilayer CrI_3 devices were studied. Monolayer WSe_2 and hBN flakes were exfoliated in the ambient condition and then transported into the glove box. CrI_3 flakes were exfoliated onto 90nm Silicon Oxide/Silicon wafer inside the glovebox with <0.5ppm O_2 and <0.5ppm H_2O environment. We identify bilayer CrI_3 by optical contrast, which was further confirmed by RMCD in the experiment. Right after identification of bilayer, we immediately assembled the heterostructure by Polycarbonate based dry transfer,

ensuring high quality of the device. After hBN encapsulation, heterostructure is robust in the ambient environment that allows us to take it out of the glovebox for loading into the cryostat.

In this project, two main optical measurement techniques were used. The polarization-resolved photoluminescence (PRPL) and the reflectance magneto circular dichroism (RMCD). We used the HeNe laser (1.96eV) for both PRPL and RMCD measurements. In both cases, the laser was normal incident to the sample with a beam spot size of about 1μm beam spot. For photoluminescence measurement, we used 3 μW for spatially resolved maps and 10 μW for magnetic field sweeps. For RMCD measurement, the laser intensity is modulated by an acoustic optical modulator (AOM) at f_1=726Hz. The photoelastic modulator (PEM) added a f_2=50kHz time variant phase difference between the vertical and horizontal polarization. The laser was set at a 45 degree linearly polarized state with respect to the axis of PEM. Since nonzero Kerr Ellipticity η_k changes the ratio of the σ^+ and σ^- light, light intensity variance shows up in accordance with f_2 in reflected laser. The laser was then sent to a photodetector which was connected to two lock-in amplifiers for analysis.

8.3 Layer Resolved Proximity in Trilayer Device

We first study a WSe_2/trilayer CrI_3 heterostructure. A device schematic is shown in Figure 8.1a, where WSe_2 is on top of CrI_3. In labeling the magnetic states of CrI_3 below, we count the CrI_3 layers from top to bottom, where the top layer interfaces with WSe_2. The excitation laser was fixed at 1.96 eV (a He-Ne laser), and the applied magnetic field is perpendicular to the sample plane. For measurement of monolayer WSe_2 photoluminescence, we performed co-circular polarized excitation and detection (either σ^+/σ^+ or σ^-/σ^-) to read out the valley exciton information. Figure 8.1c shows circular polarization-resolved photoluminescence spectra at 5 K and zero magnetic field, which is dominated by positively charged trion emission[43], consistent with type-

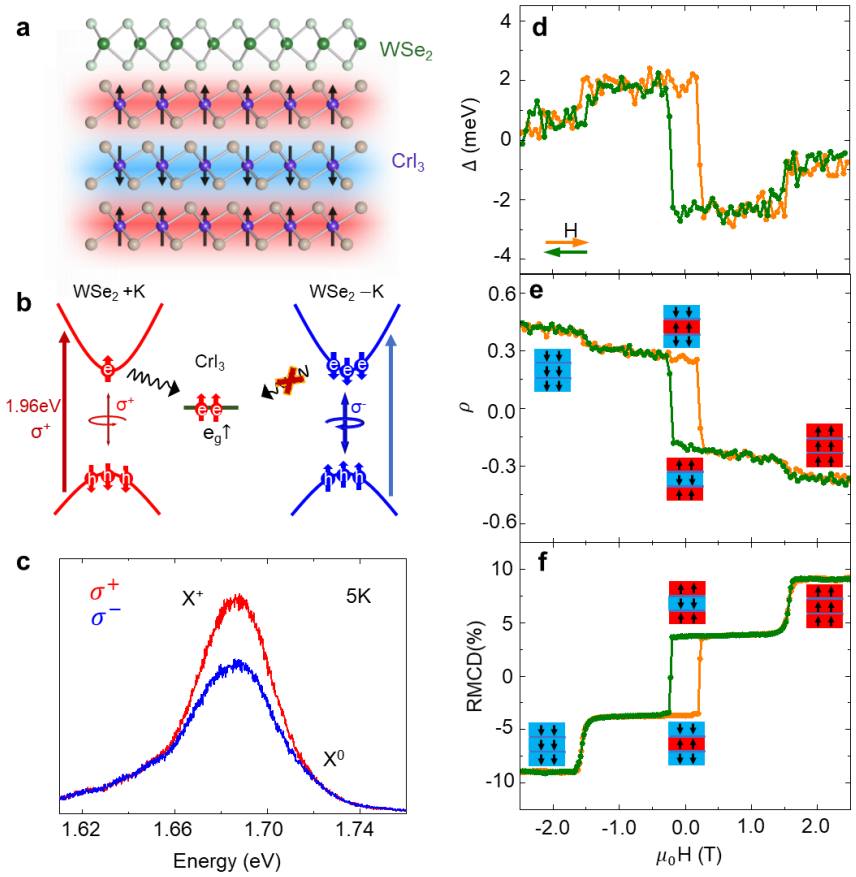

Figure 8.1. Proximity control of valley dynamics in monolayer WSe_2 interfacing with trilayer CrI_3. a, Schematic of monolayer WSe_2 and trilayer CrI_3 heterostructure and **b**, and its type-II band alignment. Assuming spin-up magnetization CrI_3, the optically excited spin-up electrons in the +K valley will transfer to the Cr^{3+} spin polarized 3d e_g band, while charge transfer of the spin down electron in the -K valley is suppressed. This spin-dependent charge transfer leads to spontaneously circularly polarized WSe_2 photoluminescence. **c**, Polarization-resolved photoluminescence of WSe_2/trilayer CrI_3 heterostructure at 1.6 K and zero magnetic field, showing spontaneously σ^+ polarized photoluminescence. **d,** Valley Zeeman splitting, **e**, degree of circular polarization in photoluminescence, **f,** and reflective magneto-circular dichroism (RMCD) as a function of magnetic field. Orange and green curves represents magnetic field sweeping up (increase) and down (decrease), respectively.

II band alignment. The σ^+/σ^+ photoluminescence (red curve) is stronger than σ^-/σ^- (blue curve); this spontaneous circularly polarized photoluminescence demonstrates the breaking of valley degeneracy and thus time-reversal symmetry of monolayer WSe_2 by proximity to the magnetic trilayer CrI_3. As discussed in Ref. [80], when the photoexcited electron spin in WSe_2 has the same orientation as the CrI_3 magnetization, charge transfer is allowed (Figure 8.1b). Otherwise, it is suppressed. This spin-selective charge transfer from WSe_2 to CrI_3 gives rise to strong circularly polarized photoluminescence (Figure 8.1c).

To investigate the relationship between the proximity effect and magnetic states, we performed polarization-resolved photoluminescence and RMCD as a function of magnetic field at 15 K. We quantify the photoluminescence polarization as $\rho = (I_{\sigma^+} - I_{\sigma^-})/(I_{\sigma^+} + I_{\sigma^-})$, where I_{σ^+} (I_{σ^-}.) represents photoluminescence intensity with co-σ^+ (co-σ^-) excitation and detection. In addition to spin-dependent charge transfer, the magnetic exchange field introduces excitonic valley Zeeman splitting, which is defined as $\Delta = E_{\sigma^+} - E_{\sigma^-}$. Here, E_{σ^+} (E_{σ^-}) is the peak position of $\sigma^+/\sigma^+\left(\sigma^-/\sigma^-\right)$ photoluminescence from K (-K) valley trions. Figures 1d-f plot ρ, Δ, and RMCD signal as a function of magnetic field, respectively. Consistent with previous reports, the RMCD signal in Fig. 1f shows three transitions in a given field sweep (at about $\pm$ 1.6T and $\pm$ 0.2T), with each corresponding to a flip in layer magnetization. The magnetic states, two fully spin-polarized states $\uparrow\uparrow\uparrow$ and $\downarrow\downarrow\downarrow$, and two layered AFM states $\uparrow\downarrow\uparrow$ and $\downarrow\uparrow\downarrow$, are indicated in Figure 8.1e-f.

As shown in Figure 8.1d and e, the evolution of magnetic states as a function of magnetic field is also manifested in both ρ-H and Δ-H traces. Let us first focus on the ρ-H trace. Consider the sweeping up curve in orange where the CrI_3 trilayer starts from a fully polarized state ($\downarrow\downarrow\downarrow$). Photoexcited electrons with spin down in WSe_2 efficiently transfer to CrI_3, resulting in stronger σ^+ polarized PL. As the magnetic field increases beyond -1.6 T, CrI_3 transitions from $\downarrow\downarrow\downarrow$ into $\downarrow\uparrow\downarrow$, with the middle layer flipping its magnetization. Correspondingly, ρ decreases slightly, by about 22%. Further increasing the magnetic field to be above 0.2 T causes CrI_3 to transition into $\uparrow\downarrow\uparrow$ with the top layer flipping its magnetization. As a result, ρ sharply changes from positive to negative since electrons with spin up are now favored to transfer from WSe_2 to CrI_3. When the magnetic field is larger than 1.6 T, CrI_3 becomes fully spin polarized ($\uparrow\uparrow\uparrow$) and

ρ reaches maximum negative value. The ρ-H trace implies that the spin-dependent charge transfer is dominated by the interfacial top layer, while the middle layer, 0.7 nm away below the interface, has a much weaker effect.

In stark contrast to ρ, the proximity exchange field, and thus the induced valley Zeeman splitting Δ has a distinct dependence on the magnetic states. As shown in Figure 8.1d, when CrI_3 is the AFM states, Δ is much larger than it is for the fully spin-polarized states. This is quite surprising since the proximity exchange field is a short-range interaction, and thus, it is expected to be dominated by the magnetization in the top layer. One would, therefore, expect the proximity exchange field to remain the same for the $\downarrow\downarrow\downarrow$ and $\downarrow\uparrow\downarrow$ configurations.

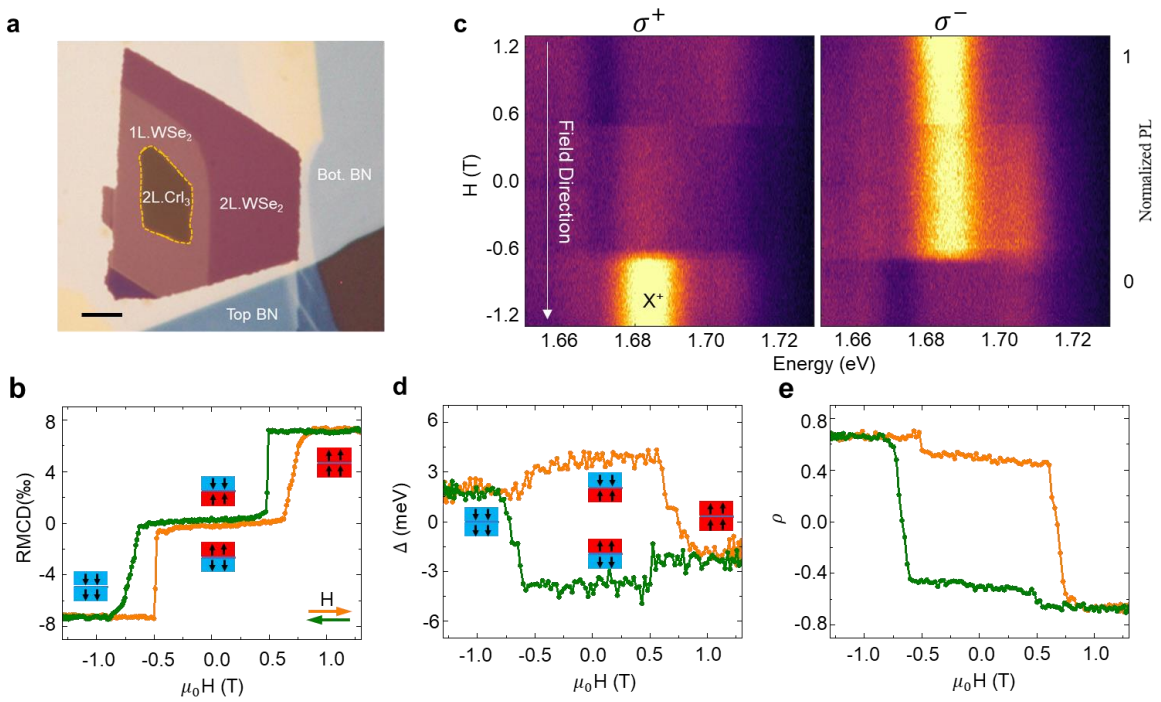

Figure 8.2. Proximity effect in monolayer WSe_2/Bilayer CrI_3 heterostructure. a, Optical microscope image of a monolayer WSe_2/bilayer CrI_3 heterostructure (Device BD1), encapsulated by hBN. Scale bar: 5μm. **b**, RMCD as a function of magnetic field, showing typical features of a layered antiferromagnetic bilayer CrI_3. **c**, Photoluminescence intensity plot of co-σ^+ (left) and co-σ^- (right) polarized excitation and detection as a function of magnetic field and photoenergy. **d**, Valley Zeeman splitting and **e,** degree of circular polarization as a function of magnetic field, extracted from data in (c).

8.4 Layer Resolved Proximity in Bilayer Device

This observation is further corroborated by measurements done on monolayer WSe_2/bilayer CrI_3 heterostructures. Figure 8.2a shows an optical microscope image of a WSe_2/bilayer CrI_3 device (BD1), with heterostructure area indicated by the yellow dashed line. The RMCD signal in Figure 8.2b is typical of bilayer CrI_3, showing two AFM states ($\uparrow\downarrow$ and $\downarrow\uparrow$) and two fully spin-polarized FM states ($\uparrow\uparrow$ and $\downarrow\downarrow$). Figure 8.2c shows the photoluminescence intensity plot of co-σ^+ (left) and co-σ^- (right) excitation and detection as a function of magnetic field and photon energy. The extracted Δ -H curve in Figure 8.2d shows that AFM states produce larger valley Zeeman splitting than the FM states. In contrast, ρ reaches maximum when CrI_3 is in the fully spin-polarized states and has a slight decrease in the CrI_3 AFM states.

The distinct behavior between ρ and Δ can be explained as following. The photoluminescence polarization ρ is determined by the real hopping of electrons from WSe_2 to CrI_3 accompanied by energy relaxation. In contrast, the proximity exchange field is primarily from a second-order virtual hopping process that shifts the WSe_2 band edge of certain spin species by $\Delta_{c/v} \sim \frac{t^2}{\Delta E}$, where t is the hopping matrix element between WSe_2 and CrI_3, and ΔE is their band offset. In the AFM configuration (e.g., $\uparrow\downarrow\uparrow$), the anti-parallel spin alignment of adjacent CrI_3 monolayers suppresses the interlayer hopping of charge carriers, which is otherwise significant in the fully spin aligned configuration (e.g., $\uparrow\uparrow\uparrow$). This magnetic-configuration-dependent interlayer hopping between CrI_3 layers leads to significantly different band edge energies of the two magnetic configurations. Distinct values of ΔE are thus expected between the CrI_3 FM and AFM configurations, which results in the change of proximity exchange field with the magnetic configuration. The measured Zeeman splitting in the photoluminescence is the difference between the conduction and valence

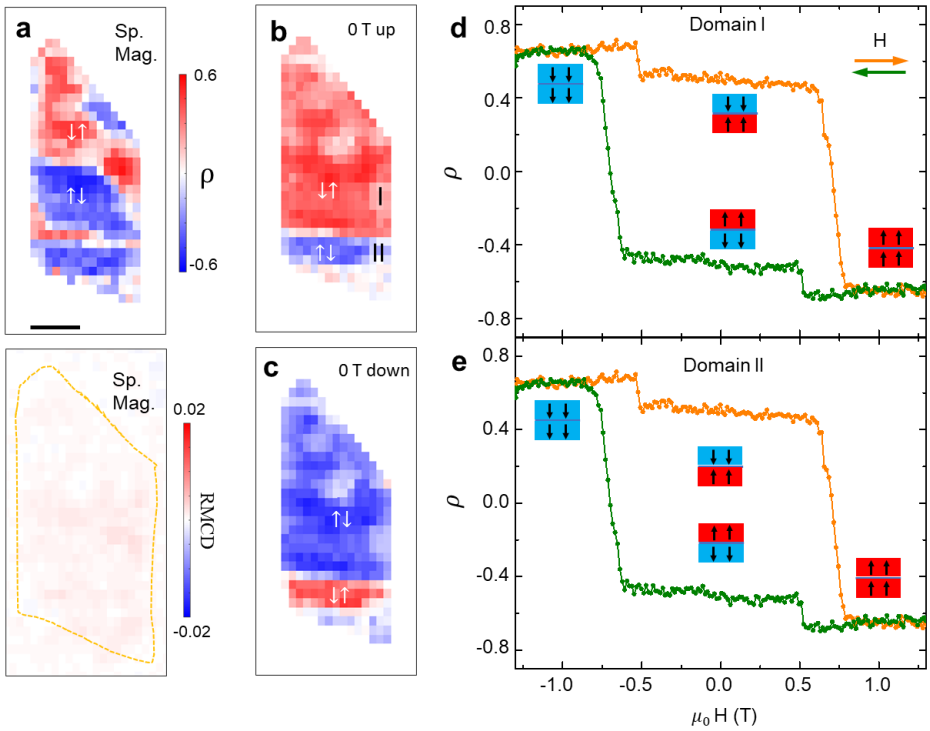

Figure 8.3. Imaging layered antiferromagnetic domains in bilayer CrI_3 by monolayer WSe_2. a, Spatially resolved RMCD (bottom) and spontaneous circular polarization (ρ) of WSe_2 photoluminescence (top) as the device BD1 cools down to 1.6 K without applying magnetic field. Scale bar: 2 μm. **b**, Spatial map of ρ at zero magnetic field as CrI_3 is initialized in ↓↓ state by applying negative magnetic field. I and II labels two layered antiferromagnetic domains. **c**, The same as (b) but with CrI_3 is initialized at ↑↑ state by applying large positive magnetic field. **d-e**, ρ as a function of magnetic at selected spots in domain I (d) and II (e). Insets depict the magnetic states.

band shifts: $\Delta = \Delta_c - \Delta_v$. We find that the observed change in Δ can be reproduced with reasonable choices of t and band offset ΔE (Appendix D4), while the precise determination of these parameters requires further experimental (e.g., angle-resolved photoemission spectroscopy) and computational studies.

The sensitive dependence of the proximity effect on the spin structure of CrI_3 shown above allows us to use monolayer WSe_2 as a magnetic sensor to probe the domain structures and dynamics in layered antiferromagnetic bilayer CrI_3. Since bilayer CrI_3 has vanishing magnetization in the AFM configuration, RMCD cannot probe the domain effects. However, the photoluminescence polarization, ρ , is dominated by the interfacial layer, thus providing an excellent probe of

magnetization in the top CrI_3 layer. Combined with RMCD, which probes the total magnetization of the bilayer, we can construct the layered AFM domains.

Figure 8.3a shows the intensity map of ρ (top) and RMCD signal (bottom) of device BD1. The data was acquired after cooling the sample down to the 1.6 K in the absence of a magnetic field. The map of ρ is composed of positive and negative polarization patches, which corresponds to the up and down magnetization domains of the top layer in the CrI_3 bilayer. On the other hand, the RMCD map has nearly zero intensity across the whole heterostructure, showing that bilayer CrI_3 is in an AFM ground state. The comparison of both maps reveals the spontaneous formation of $\uparrow\downarrow$ and $\downarrow\uparrow$ layered AFM domains.

The spontaneously formed layered AFM domain walls can be reconfigured by applying an external magnetic field. For instance, after initializing the bilayer to the $\downarrow\downarrow$ state by a large negative magnetic field, we sweep the magnetic field back to zero. The resulting spatial map of ρ in Figure 8.3b shows two dominant layered AFM domains, labeled by I and II. We can also initialize the bilayer in the $\uparrow\uparrow$ state and then sweep the magnetic field back to zero. The corresponding spatial map of ρ, shown in Figure8.3c, is a time reversal of Figure 8.3b. Figures 8.3d and e show ρ-H at two selected spatial points in domains I and II, respectively. When the magnetic states switch from FM to AFM, ρ drops slightly in domain I (Figure 8.3d), while it changes drastically and reverses sign in domain II (Figure 8.3e). These data demonstrate that the top layer in CrI_3 bilayer flips magnetization first in domain II, while the bottom layer flips first in domain I (see Appendix D1 for additional data). Comparing to Figure 8.3b&c with Figure 8.3a, we can see that among the spontaneously formed layered AFM domains in Figure 8.3a, domain II is pinned with a fixed boundary, while others are movable and reconfigured after magnetization initialization. This pinned domain II is likely due to strain introduced by the heterostructure fabrication.

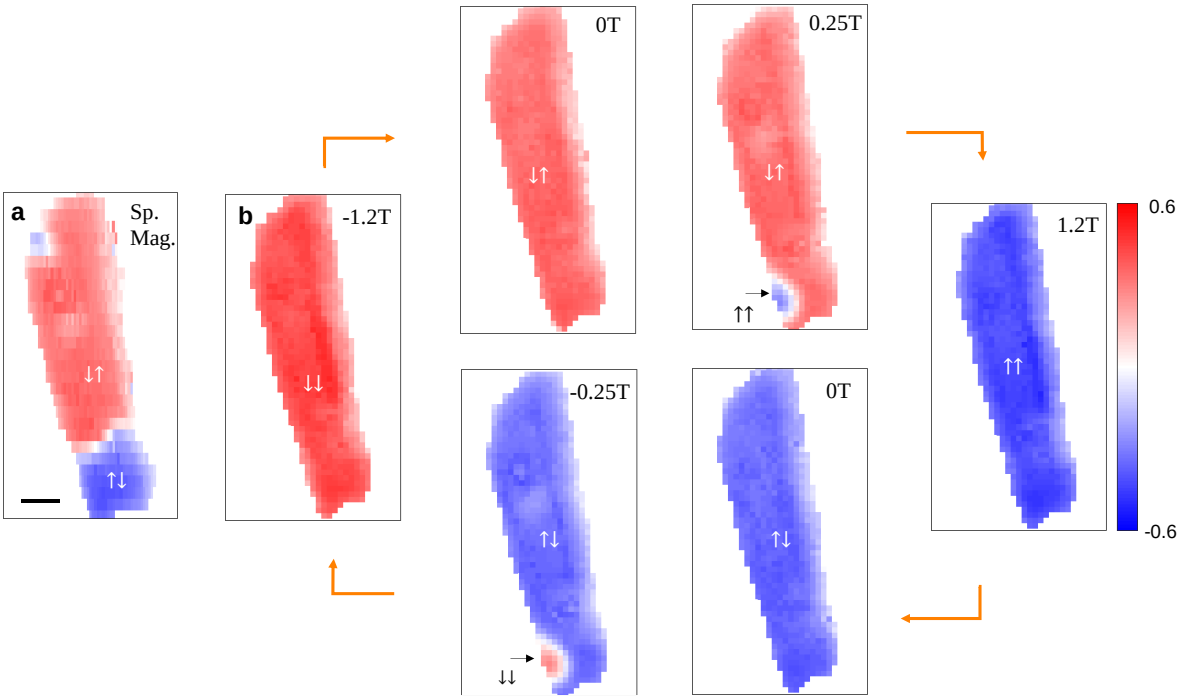

Figure 8.4. Imaging layered antiferromagnetic-ferromagnetic domains in bilayer CrI_3 by monolayer WSe_2. **a**, Spatial map of ρ of spontaneously circularly polarized WSe_2 photoluminescence as device BD2 cools down to 1.6K without applying magnetic field. Scale bar: 2 μm. **b**, Spatial map of ρ at selected magnetic fields. Layered antiferromagnetic and ferromagnetic domains at ±0.25T maps are indicated. Insets depict the magnetic states.

8.5 Probing Domain Patterns in CrI_3 with WSe_2

We found that the domain structures vary between devices, likely caused by the uncontrolled heterostructure fabrication process. Figure 8.4 shows another example (device BD2) measured at 6.6 K. The spontaneously formed domain structure is mainly dominated by two layered AFM domains (Figure 8.4a). After the bilayer CrI_3 has been initialized by the magnetic field, the layered AFM domains at zero field vanish, and only a single domain exists (Figure 8.4b). However, at finite magnetic fields, we observed a layered AFM/FM domain wall. For instance, as the magnetic field increases from zero, a ↑↑ domain forms first at the bottom left corner of the heterostructure at a magnetic field of 0.25 T, while the rest of the sample is still in the ↓↑ state. Distinct ρ-H traces from these two domains are shown in Appendix D2. Compared to BD1, this device has less

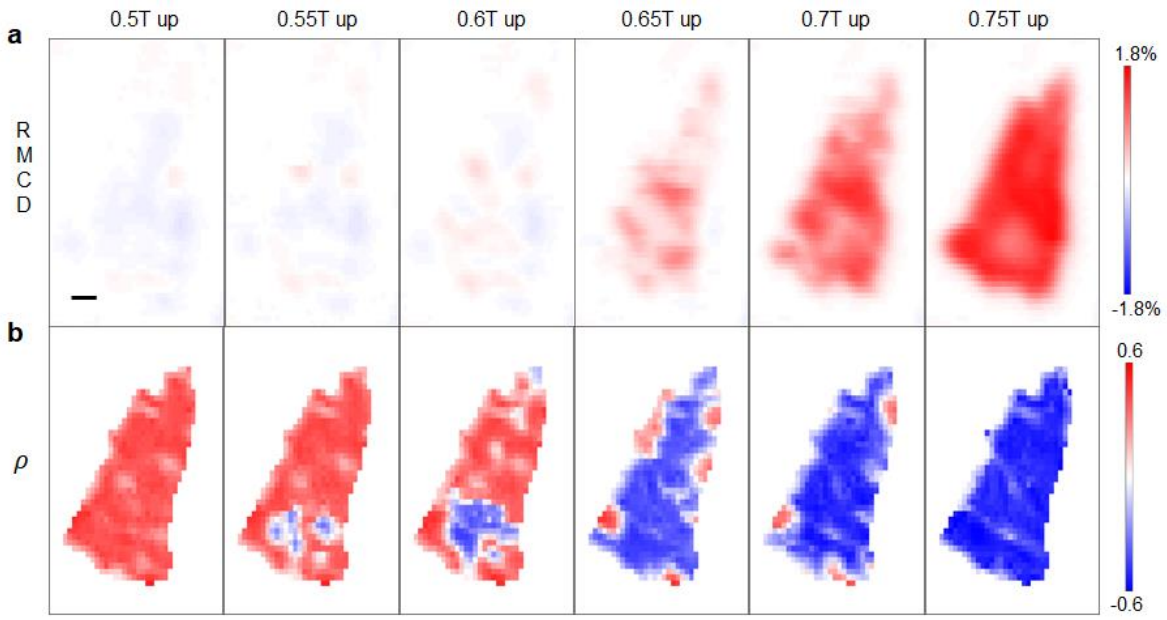

Figure 8.5. Imaging domain dynamics near metamagnetic transitions of bilayer CrI_3. Spatial maps of **a**, RMCD, and **b**, ρ at selected magnetic fields near metamagnetic transition from a third monolayer WSe_2/bilayer CrI_3 device (BD3). The evolution of layered antiferromagnetic and fully spin polarized ferromagnetic domains is evident in the maps of ρ. Scale bar: 2 μm.

complicated domain structures at zero magnetic field, which may indicate a better transfer with a more homogeneous strain distribution.

We have also observed complicated, layered AFM/FM domain patterns in a less homogenous sample compared to device BD2. Figure 8.5 shows spatial maps of both RMCD and ρ on a third monolayer WSe_2/bilayer CrI_3 device (BD3) as the magnetic field sweeps through the metamagnetic transition at 1.6 K. The RMCD maps in Fig. 5a shows faint spotty patterns, indicating spatial inhomogeneity in the transition from $\downarrow\uparrow$ to $\uparrow\uparrow$. The evolution of domains across this metamagnetic transition is clearer in the spatial maps of ρ (Figure 8.5b), which highlights the domain dynamics near the spin-flip transition. Appendix D3 shows similar complicated domain effects in BD1. As suggested, the inhomogeneity is likely from strain introduced in the heterostructure transfer process. Our work gains insights on the magnetic proximity effects in a vdW magnetic heterostructure, as well as highlights an example of

harnessing spin-valley physics in a monolayer semiconductor for probing rich magnetic domain physics in a vdW magnet.

Chapter 9. OPTICAL TUNING OF WSe_2/CrI_3 HS FOR VALLEYTRONICS

In the previous chapter, our studies on WSe_2/CrI_3 heterostructure demonstrated several merits for valleytronics applications. Interaction between the WSe_2 and CrI_3 takes place, which integrates strong exchange field and enhanced magnetic field response to WSe_2's valley degrees of freedom. However, all these features rely on the domain dynamics of CrI_3 while control over CrI_3's domain magnetization is very limited. Thus, the control of valley degree of freedom is strictly dependent on CrI_3's magnetization which to some extent, limits the flexibility and versatility of the device. For example, due to strong anisotropy, the CrI_3's magnetization tends to take either up or down direction, which means that ρ and Δ for the most part take discrete values that are either high positive or high negative, unless the field is within metamagnetic transition region. Even when it is the case, the magnetization can go one way and the state stability is a issue since it is extremely sensitive to perturbation to the applied field. Thus, achieving a continuous tuning of valley properties in between two extreme values is hard. Second, the tuning of ρ and Δ is mostly desired to go one way, since resetting the magnetic state usually requires conducting a whole magnetic field sweep to complete.

In this chapter, we present the realization of optical control of CrI3's magnetization, which subsequently achieves optical control of valley properties in WSe_2. This is achieved by having a laser excitation power dependent metamagnetic transition in weak domain CrI_3, which allows for the wide continuous and reversible tuning of the valley polarization and valley Zeeman splitting with small changes of optical power. Our result adds a new function to the WSe_2/CrI_3 heterostructure and reveal a convenient new path towards optical control of valley pseudospins. This work is reprinted from Kyle L. Seyler, **Ding Zhong**, Bevin Huang, Xiayu Linpeng, Nathan P. Wilson, Takashi Taniguchi, Kenji Watanabe, Wang Yao, Di Xiao, Michael A. McGuire, Kai-

Mei C. Fu, Xiaodong Xu, *Valley Manipulation by Optically Tuning the Magnetic Proximity Effect in WSe_2/CrI_3 Heterostructures.* Nano Letters, 2018. **18**(6): p. 3823-3828 [97].

9.1 The Power Dependent Metamagnetic transition in CrI_3

The heterostructure consists of monolayer WSe_2 and ~10nm CrI_3 protectively encapsulated by two 10~20nm hexagonal boron nitride, as shown in Figure 9.1a. The data in this chapter were taken at 1.6K under 1.96eV continuous-wave laser excitation with about 1 μm excitation spot diameter.

Similar to previous chapter, our method of measurement includes polarization-resolved photoluminescence (PRPL) on WSe_2. The valley polarization ρ and valley splitting Δ are extracted from the intensity difference and energy difference between σ^+ and σ^-. As demonstrated in Chapter 5, these quantities are proximity induced effect from CrI_3, and the sign of which are directly correlated with the underlying CrI_3 magnetization direction. Figure 9.1c is a spatial map of the WSe_2 PL intensity, which was acquired by rastering the laser over the boxed region in Figure 9.1b. Spatial maps of ρ thus reveal magnetic domain structure in CrI_3. For instance, ρ is spatially uniform and negative at 1T (Figure 9.1d, right panel), with respective spectra shown in Figure 9.1e. This implies uniform positive magnetization at the interface. However, upon decreasing to 0.7T (Figure 9.1d, left panel), a domain of heterostructure flips to positive ρ signifying a change in the magnetization state of underlying CrI_3. We label this region as domain A. Magnetic field dependent measurement inside domain A at indicated spot reveals three times sign flips in ρ, as shown in Figure 1f. This result indicates the "weak domain" feature which is a concept we introduced in chapter 5.

For the outer hysteresis loop (indicated by shaded area in Figure 9.1f) of domain A, we found it to be strongly dependent on the photo-excitation power. In Figure 9.2a, ρ is plotted as the magnetic

field sweeps from 0.6 to 1.2T and then back to 0.6T at selected excitation powers. The hysteresis loop gradually evolves from wide and square at 1μW to narrow and sloped at 100μW. This photoinduced change in the coercivity has dramatic consequences for the optical control of valley

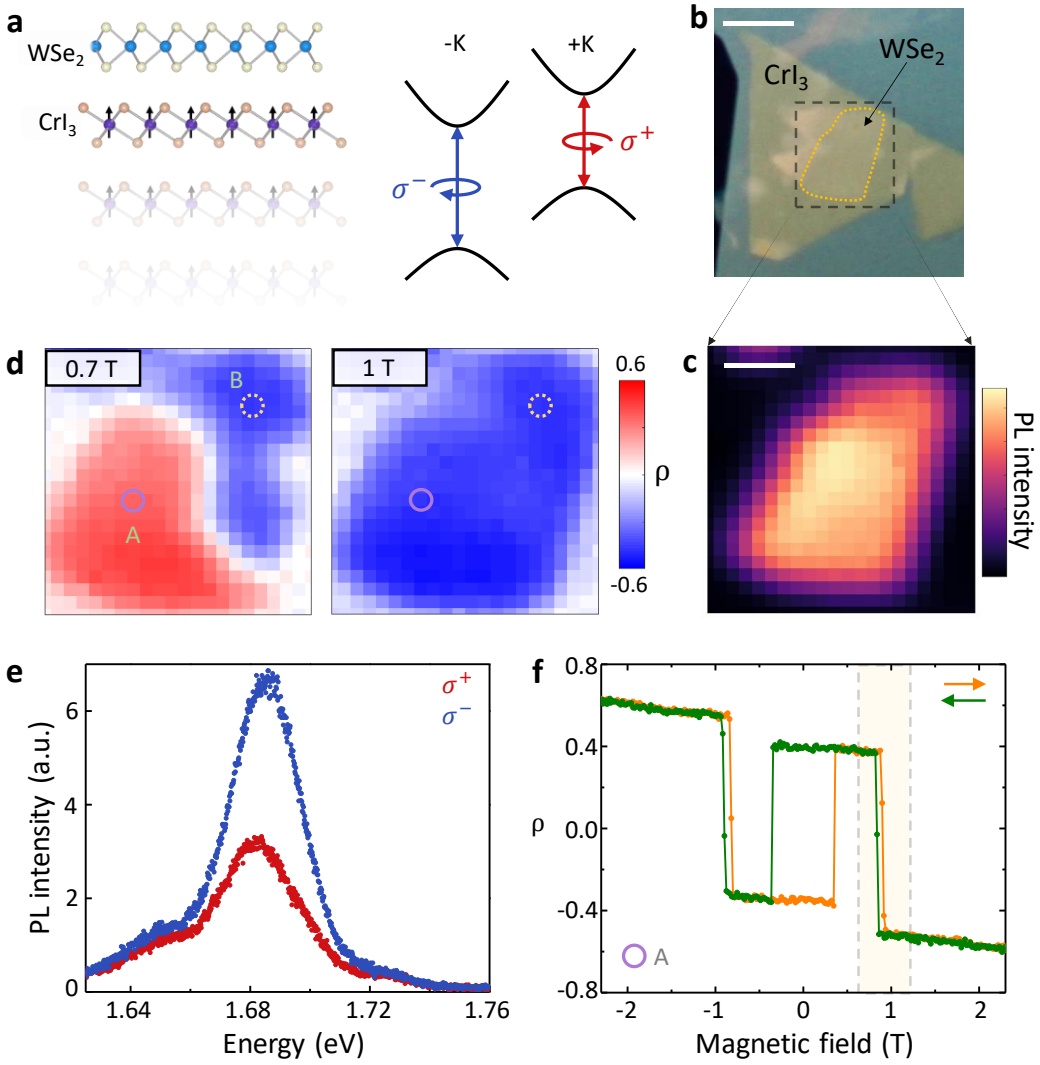

Figure 9.1. Basic characterization and domains of WSe_2/CrI_3 heterostructure. (**a**) Schematic of WSe_2/CrI_3 heterostructure (left). Valley energy levels and optical selection rules of monolayer WSe_2 with magnetic exchange field coupling (right). h-BN encapsulation layers are not shown. (**b**) Optical microscope image of heterostructure. Dashed box region shows the laser scanning area and the dotted yellow curve outlines the WSe_2 monolayer region. Scale bar, 5 μm. (**c**) Spatial map of total photoluminescence (PL) intensity within the boxed region of Figure 9.1b. Scale bar, 2 μm. (**d**) Spatial maps of the polarization parameter ρ (see text for definition) at 1 T (right) and 0.7 T (left) applied magnetic field. Same scale as Figure 9.1c. (**e**) Spectra of σ^+ (σ^-) PL under σ^+ (σ^-) laser excitation taken at 1 T applied magnetic field, shown in red (blue). (**f**) ρ as a function of applied magnetic field sweeping up (orange) and down (green). The data was taken at the location marked by the solid purple circle in Figure 9.1d.

properties at a fixed magnetic field near the hysteresis loop. We performed power-dependent measurements of ρ at fixed magnetic fields from 0.7T to 1T, as shown in the 2D plot of ρ in Figure 9.2b. The magnetic field was first initialized by sweeping up from 0.6T. Below ~0.75T and above ~0.92T, ρ decreases in magnitude slightly with increasing power, but its sign remains the same; meanwhile at intermediate fields, the sign of ρ flips at high powers. The curved white area shows that the critical power decreases at higher magnetic fields, which is consistent with the power dependence of hysteresis loop in Figure 9.2a. We also find similar power dependence and switching behavior for the valley Zeeman splitting (Δ), which is shown in Appendix E1.

9.2 Reversibility of The Power Dependent Hysteresis Loop

We first use a set of PRPL results with different power at 0.88T to illustrate the power-switchable valley properties. At low excitation powers, I_+ is more intense and has higher energy than I_-.

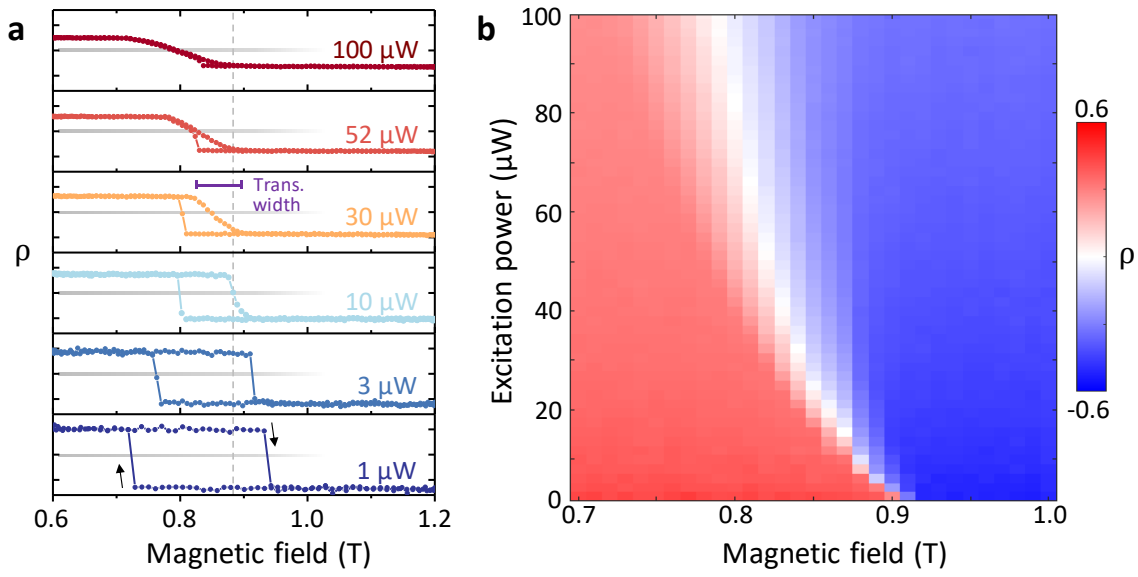

Figure 9.2. Power-dependent hysteresis and valley switching. (**a**) Magnetic field sweeps of ρ from 0.6 to 1.2 to 0.6 T (highlighted region in Figure 9.1f) at different excitation powers. Gray horizontal lines indicate ρ = 0 and the neighboring tick marks on the y-axis are ±0.5. Sweep directions are shown by the black arrows. The transition width for 30 μW hysteresis loop is marked by the purple line. (**b**) Map of the power dependence of ρ taken at different applied magnetic fields. The magnetic field was first initialized by sweeping up to 0.7 T. A power dependence was then performed from 1 to 100 μW at the different fixed magnetic fields from 0.7 to 1 T.

With increasing power, however, I_+ and I_- become degenerate and eventually, they switch relative intensity and energy. In Figure 9.3a, we conducted continuous power sweep between 4μW to 40μW, ρ continuously changes from 0.41 to -0.37 and Δ from 3.7 to -1.3meV. To produce comparable Δ swing with a bare WSe_2 monolayer would require sweeping an external magnetic field for 20T.

An important observation in Figure 9.3b, c is that upon decreasing the power immediately after ramping the power up to 40μW, identical values of ρ and Δ was measured compared with the

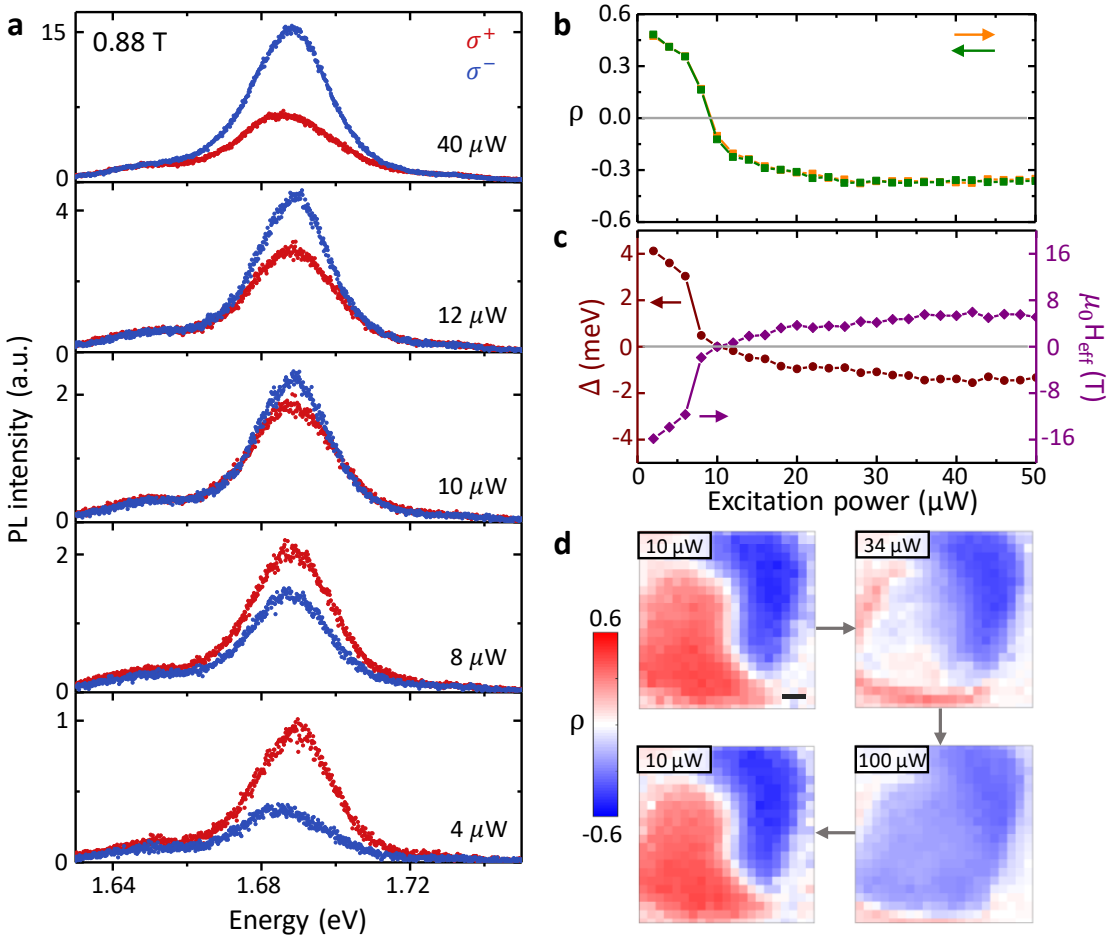

Figure 9.3. Manipulation of valley polarization and splitting via optical excitation power. (**a**) Circularly polarized PL spectra at selected excitation powers. The applied magnetic field was initialized to 0.88 T from 0.6 T. (**b**) Power dependence of ρ at 0.88 T with increasing (orange) and decreasing (green) power. (**c**) Power dependence at 0.88 T of the valley splitting (Δ, left) and the corresponding effective magnetic field ($\mu_0 H_{eff}$, right). (**d**) Spatial maps of ρ at 10, 34, 100, and 10 μW, in that order. The black scale bar represents the laser beam diameter (1 μm), which is much smaller than the domain size.

power sweeping up curve. This means that the effects are fully reversible with no hysteresis. In Figure 9.3d, we use power dependent spatial to further explore the reversibility. The arrows denote the acquisition order of the maps, which were all taken at 0.84T. At low laser excitation power, there are two areas of opposite polarization, which correspond to the two magnetic domains as discussed. As the power increases to 100μW, the domain of positive polarization completely reverses, which means that the optical excitation can flip all areas of domain A. Furthermore, as the excitation power is lowered back to 10μW, the original domain pattern covers. This result corroborates the power dependent result, demonstrating the reversibility of the effect occurs on all areas of domain A.

9.3 Exploration on The Origin of The Power-Dependent Loop

The excitation power control of ρ and Δ is clearly established. Still, we need to confirm that these effects arises from optical control of the CrI_3 magnetization. Therefore, we directly probed the CrI_3 magnetization via reflectance magneto circular dichroism (RMCD) on domain A. In contrast to ρ, which flips sign three times in a magnetic field sweep, the RMCD signal contains many step-like jumps and is monotonic with the magnetic field (Figure 9.5a). While there are changes in the RMCD signal where ρ and Δ flip sign, the additional jumps near 0T and ± 1.9T do not appear in the behavior of ρ. From the size of RMCD steps near 0.8T, we determine that they originate from the magnetization reversal of a single CrI_3 layer, and furthermore, the hysteresis exhibits power dependence very similar to ρ (Appendix E2). As we have demonstrated in the last chapter, the proximity effect is mostly decided by the interfacial CrI_3 layer. We thus confirmed that the RMCD jumps near ± 0.8T correspond to the magnetization flip of the top CrI_3

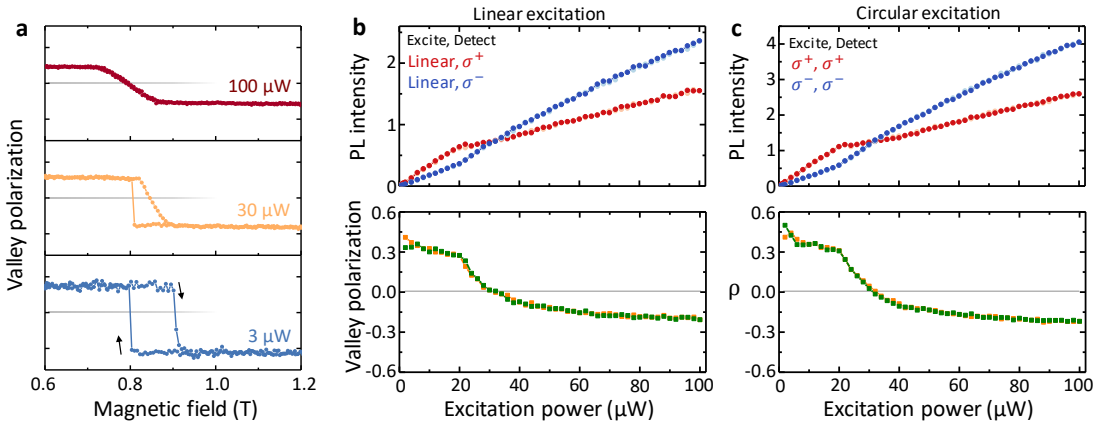

Figure 9.4. Polarization dependent hysteresis loop. (**a**) Hysteresis loops of the valley polarization (circular polarization under linear excitation) at selected excitation powers from 0.6 to 1.2 to 0.6 T. Power dependence of PL intensity and ρ for linear (**b**) and circular excitation (**c**) at 0.84 T.

layer, while the other step-like jumps in Figure 9.5a arises from magnetization reversal within deeper layers.

Next, we focus on the origin to the optical control of CrI_3 magnetization. The first hypothesis would be the spin torque effect. This hypothesis is favored on the fact that there is spin-polarized charge hopping from WSe_2 into CrI_3 when the former is optically excited. These induced spins could exert an effect on CrI_3 which flip its magnetization. This hypothesis is examined by comparing linear polarization excitation with circular. The former, according to the optical transition rules, excite half amount of carriers in both valleys as circularly polarized light does in one valley. First, the linear excitation leads to similar power dependent loop as circular excitation, as shown in Figure 9.4a. A comparison between the valley polarization tuning by linear excitation and circular polarization is shown in Figure 9.4b. The identical result between the circular and linear excitation demonstrates that the total magnetization switching effect relies on the total power of the laser rather than its polarization, which falsifies the hypothesis of the spin torque effect.

Another hypothesis is the laser induced heating. Since laser concentrates the power onto a small area (~1 μm) on the device, it could raise the local temperature, leading to a change in the coercive

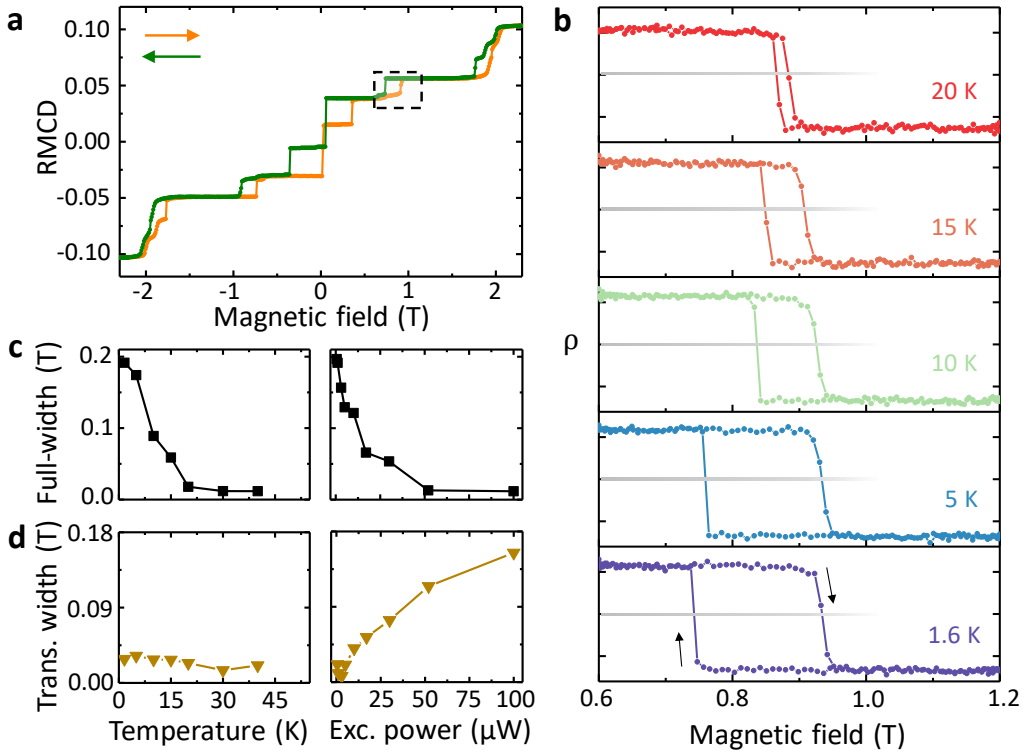

Figure 9.5. CrI_3 magnetization and temperature dependence of hysteresis loop. (**a**) RMCD as a function of the applied magnetic field sweeping up (orange curve) and down (green curve) on domain A at 1 μW optical excitation power. (**b**) ρ magnetic field sweeps as a function of temperature. The excitation power is 1 μW. Horizontal gray lines indicate $\rho = 0$ and the neighboring tick marks on the y-axis are ±0.5. Black arrows indicate the field sweep directions. (**c**) Full-width of the hysteresis loop (at $\rho = 0$) versus temperature at 1 μW excitation power(left) and versus excitation power at 1.6 K (right). (**d**) Transition width versus temperature for 1 μW power (left) and versus excitation power at 1.6 K.

field. This hypothesis can be examined by temperature dependent measurement with every low power excitation (1 μW), as shown in Figure 9.5b. The full-width of the loop decreases with temperature, similar to what occurs at high powers (Figure 9.2a). On the other hand, there is a clear difference in the shape of the hysteresis loop and the magnetic field range of the transition where ρ reverses (i.e., transition width). From 1.6K to 40K, the transition width remains small (Figure 9.5c), as is clear from the box-like loop shapes in Figure 9.5b. In contrast, higher power forces a slant in the loop shape (Figure 9.2a), increasing the transition width. The magnetization thus appears to gradually rotate with the magnetic field at high powers, unlike the rapid spin-flip transition that occurs at lower powers. Thus the laser induces heating is insufficient to entirely

account for the power dependent hysteresis loop. Future analysis of the CrI_3 magnetization flipping should thus consider other effects from the photoexcited carriers in addition to laser-induced lattice heating.

9.4 Conclusion

The optical control of magnetic coercivity has also been observed in magnetic semiconductor systems, such as (Ga,Mn)As[99], Ni/GaAs[100]. In these samples, photoexcited carriers reduce the coercivity by enhancing the carrier-mediated exchange interactions, which lower the domain wall energies. For CrI_3, further detailed optical studies and gate-dependent measurements are needed to clarify the role of photoexcited carriers on its layered magnetic ordering and domain structures. Moreover, time-resolved measurements may reveal magnetization switching dynamics and shed light on the underlying mechanisms. Our results thus open many new avenues of exploration for 2D magnets, revealing a promising new route to valley manipulation, and establish a strategy for optically controlling the interfacial magnetic exchange field in van der Waals heterostructures.

Appendix A Supplementary Materials for Chapter 5

A1 Electronic structure of CrI_3/WSe_2 bilayer

To determine the band alignment of the CrI_3-WSe_2 heterostructure, we perform first-principles electronic structure calculations for a bilayer made of a monolayer of CrI_3 and a monolayer of WSe_2. We used the generalized gradient approximation in the parametrization of Perdew, Burke, and Enzerhof (*44*, *45*), as implemented in the QUANTUM ESPRESSO simulation package (*46*). A vacuum slab of 15 Å was used. An energy cutoff of 130 Ry and a 12×12×1 Monkhorst-Pack special *k*-point mesh for the Brillouin zone integration was found to be sufficient to obtain convergence. To obtain a commensurate heterostructure, 3% strained 2x2 in-plane superlattice of WSe_2 (a_0 = 3.32 Å) is lattice matched to CrI_3 (a_0 = 6.84 Å). This leads to a reduction of the WSe2 band gap compared to the unstrained monolayers, but it does not affect the type of the band alignment. Structural optimization for the bilayer was performed by fixing the in-plane lattice constants to that of the theoretical bulk CrI_3 lattice constants. Semiempirical Grimme's DFT-D2 method was used to describe van der Waals interactions (*47*, *48*). The relaxation of the ions was done with the electronic degrees of freedom accurate up to 10^{-6} eV. The results presented here are for a stacking configuration where one of the magnetic Cr^{3+} ions is directly below a W atom (see Figure A.1.A).

The orbital projected electronic structure of the bilayer is shown in Figure A.1.C. The conduction band minima are mainly made of unoccupied Cr *d*-orbitals with their spin orientation the same as the occupied Cr *d*-orbitals. The valence band maxima (VBM) are mainly made of W d_{xy} and $d_{x^2-y^2}$ orbitals. There is also some hybridization with the I and Se *p*-orbitals in the

conduction and valence bands, respectively (not shown). Thus, the valence and conduction band edges are in the two different monolayers, resulting in a type-II band alignment.

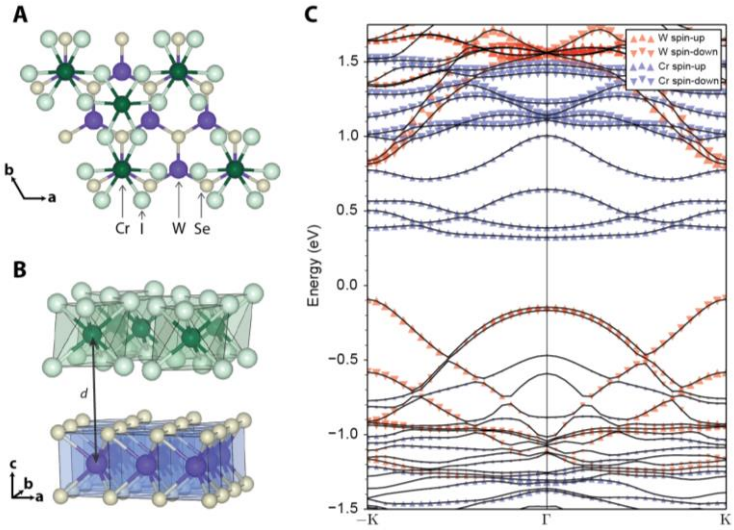

Figure A.1. The atomic structure and the electronic band structure of the CrI_3-WSe_2 bilayer. **(A)** Top and (**B**) side view of the CrI_3-WSe_2 bilayer. Dark green, light green, purple and tan spheres represent Cr, I, W and Se atoms, respectively. The Cr-W distance is labeled as *d*. (**C**) Electronic structure of the CrI_3-WSe_2 bilayer. The contribution from the W (Cr)-orbitals is shown with red (blue) triangles with the triangles pointing up (down) for up (down)-spins.

A2 Temperature dependence

Temperature dependence of the ρ spatial maps is shown in Figure A.2. The applied magnetic field is fixed at -0.15 T after sweeping up from -1.1 T. The main feature is the decrease in ρ as temperature increases and its eventual disappearance above ~ 65 K, which suggests that T_C in our ~10 nm CrI_3 is comparable to bulk samples (~61 K)[42]. While the domain structure remains mostly unchanged with temperature, there are subtle changes (e.g. in the shape of the large blue domain), which highlights the utility and sensitivity of the scanning PL technique for probing the CrI_3 magnetization.

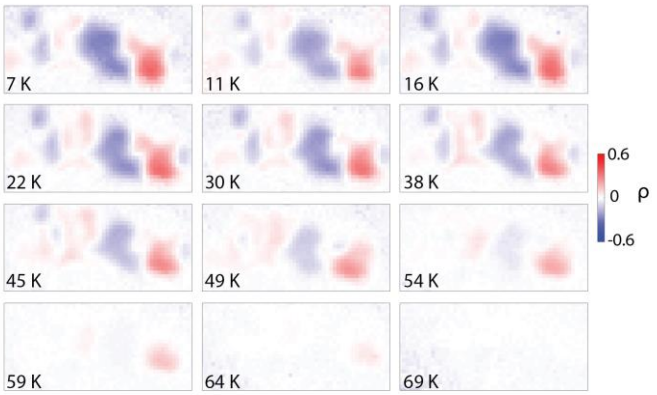

Figure A.2. Temperature dependence of CrI_3 magnetization. Spatial maps of ρ at selected temperatures. The temperatures are indicated on the respective plots.

A3 Model of strong and weak domain

The observed PL spectrum reflects the magnetization configuration of the CrI_3. In our convention, the absolute value of PL data and the absolute value of M_z (magnetization along the easy-axis) are of opposite sign. In the following, we model the hysteresis loop by focusing on the magnetization direction instead of the PL data, but one should be bear in mind that there is an overall minus sign difference between Figure A.3. and Figure 5.3. Consider a phenomenological model consisting of two monodomains with magnetization vectors denoted by m_1 and m_2. Let the polar angles of the two domains with respect to the *z* axis (i.e., the easy-axis) be θ_1 and θ_2. The magnetic switching is realized by individual domain flip, and we ignore DW dynamics induced by the magnetic field as it is not a prominent feature from the data. Nevertheless, the DW energy contributes a term $-D\cos(\theta_1-\theta_2)$ to the free energy, where D can be determined by system parameters but it suffices to treat D as a phenomenological constant for our purposes. According to the experimental condition, the magnetic field H is parallel to z. Assume that $M_1 = m_1V_1 > M_2 = m_2V_2$ where M_1 and M_2 are the magnetization amplitudes and $V_{1,2}$ are the volumes of the two domains. For either unequal values of magnetization or unequal volumes, the total Zeeman energy of domain 1 is larger than that of domain 2. It is in this sense that we call domain 1 the 'stronger' domain and domain 2 the 'weaker' domain. Our model can be easily generalized to the case of multi-domains, as long as their Zeeman energies are different enough to be divided into strong and weak. The free energy of such a two-domain system is

$$E = (JM_1M_2 - D)\cos(\theta_1-\theta_2) - H(M_1\cos\theta_1 + M_2\cos\theta_2) + K(M_1\sin^2\theta_1 + M_2\sin^2\theta_2), \quad \text{(A.1)}$$

where $K>0$ is the easy-axis anisotropy, $J>0$ characterizes the long-range dipolar interaction of two domains (which always favors anti-parallel) and the unit is chosen such that JM_1M_2 has an energy dimension. We have neglected all constant terms independent of $\theta_{1,2}$ in Eq. S1 to simplify the following analysis. It is easy to check that for the four configurations listed in Table 1, $\partial \mathrm{E}/\partial\theta_1 = \partial \mathrm{E}/\partial\theta_2 = 0$, which means that they are all local extrema of the free energy. However, the corresponding second-order derivatives

$$\frac{\partial^2 E}{\partial \theta_1^2} = \left(D - JM_1M_2\right)\cos\left(\theta_1 - \theta_2\right) + HM_1 cos\theta_1 + 2KM_1 cos2\theta_1 \qquad \text{(A.2)}$$

$$\frac{\partial^2 E}{\partial \theta_2^2} = \left(D - JM_1M_2\right)cos\left(\theta_1 - \theta_2\right) + HM_2 cos\theta_2 + 2KM_2 cos2\theta_2 \qquad \text{(A.3)}$$

are quite different, indicating that the stability depends on the magnetic field. For example, it is easy to see from Table 1 that in the range $\frac{J}{M_2} - 2K < H < J/M_2 + 2K$, both $(0,0)$ and $(0,\pi)$ are stable configurations as $\partial^2 E/\partial\theta_1^2 > 0$ and $\partial^2 E/\partial\theta_2^2 > 0$. This range defines a side hysteresis loop of M_2 around

$$H_t = \frac{JM_1M_2 - D}{M_2}, \qquad \text{(A.4)}$$

as illustrated in Figure A.3. Here, H_t marks the point where the Zeeman energy and the dipolar interaction compensate each other in the weak domain.

So long as the inter-domain coupling J is sufficiently large (here J is the dipolar interaction), there are three separate loops based on energy and stability analysis (*49*). The coercivity fields of the center loop and the side loops are, respectively,

$$H_{c1} = 2K \frac{\left(1+\frac{M_2}{M_1}\right)}{1-\frac{M_2}{M_1}} \tag{A.5}$$

$$H_{c2} = 2K\,. \tag{A.6}$$

The actual measured hysteresis loop is quite sensitive to the position of the laser spot. If the spot is placed on a strong domain, the Zeeman energy is always dominant, so it exhibits normal hysteresis loop as shown in Figure 5.5E. If the spot is positioned on a weak domain, however, the local magnetic configuration being monitored is determined by the competition between the dipolar J and the Zeeman energy, with a coercivity field set by the anisotropy. If the laser spot covers the boundary between two adjacent domains, things become complicated and cannot be captured by a simple model ignoring DW dynamics. For example, we observed in Figure 5.5D a successive step pattern when the laser spot is on a domain boundary, which might be an indication of Barkhausen jumps and that DW pinning is due to point defects rather than line defects.

Table A.1. The free energy and its second-order derivatives with respect to the angles of the two domains. Assume that $JM_1M_2 > D$.

θ_1	θ_2	E	$\partial^2 E / \partial \theta_1^2$	$\partial^2 E / \partial \theta_2^2$
0	0	$\left(JM_1M_2 - D\right)$ $-H\left(M_1 + M_2\right)$	$-\left(JM_1M_2 - D\right)$ $+HM_1 + 2KM_1$	$-\left(JM_1M_2 - D\right)$ $+HM_2 + 2KM_2$
0	π	$-\left(JM_1M_2 - D\right)$ $-H\left(M_1 - M_2\right)$	$\left(JM_1M_2 - D\right)$ $+HM_1 + 2KM_1$	$\left(JM_1M_2 - D\right)$ $-HM_2 + 2KM_2$
π	0	$-\left(JM_1M_2 - D\right)$ $+H\left(M_1 - M_2\right)$	$\left(JM_1M_2 - D\right)$ $-HM_1 + 2KM_1$	$\left(JM_1M_2 - D\right)$ $+HM_2 + 2KM_2$
π	π	$\left(JM_1M_2 - D\right)$ $+H\left(M_1 + M_2\right)$	$-\left(JM_1M_2 - D\right)$ $-HM_1 + 2KM_1$	$-\left(JM_1M_2 - D\right)$ $-HM_2 + 2KM_2$

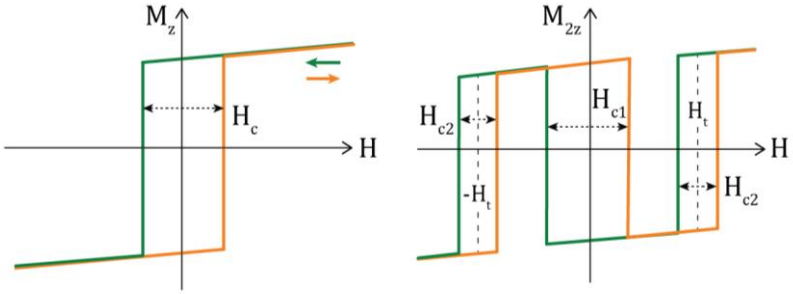

Figure A.3. Normal and triple-hysteresis loops. Normal loop corresponds to PL data from strong domains, while triple loops reflects PL data from weak domains.

Appendix B Supplementary Materials for Chapter 6

B1 Quantitaive optical microscopy in CrI_3

Optical microscopy images were taken using a Nikon Eclipse LV-CH 150NA optical microscope with a DS-Ri2 full-frame camera. The setup was located inside a glove box (argon atmosphere) in order to prevent sample degradation. The quantitative optical contrast analysis required that images were captured with a 100x objective under monochromatic illumination at normal incidence. In practice, 10 nm full-width at half maximum (FWHM) filters were used (Andover Corp.) to filter the light coming from a halogen lamp.

The thickness of the flakes was determined by contact-mode atomic force microscopy (AFM) in ambient conditions. Given the extreme sensitivity of the samples to atmospheric moisture, the CrI_3 flakes were encapsulated between two pieces of few-layer graphite (typically 5 nm in thickness) prior to being extracted from the glove box.

For each optical microscopy filtered image, individual RGB values were extracted and averaged over each flake and substrate region to give the reflected intensities of the flake and substrate. The intensity was chosen to be exclusively the value of the channel with the highest number of counts. The experimental optical contrast value was then calculated according to the following expression.

$$C(d,\lambda) = \frac{I_{flake} - I_{substrate}}{I_{flake} + I_{substrate}} \tag{B.1}$$

Equation (B.1) expresses the relationship between the optical contrast C between each flake and the substrate using the reflected intensities from the flake (I_{flake}) and the substrate ($I_{substrate}$).

For flakes that have been exfoliated on a SiO_2/Si substrate, *C* depends on the thickness of the flake and on the illumination wavelength [101, 102]. Following the quantitative microscopy analysis proposed for graphene on SiO_2/Si substrates[28], *C* can be computed for any kind of flake by using a model based on Fresnel's equations shown in (B.2) and (B.3):

$$I_{substrate}(\lambda) = \left| \frac{r_{02} + r_{23} e^{-2i\Phi_2}}{1 + r_{02} r_{23} e^{-2i\Phi_2}} \right|^2 \tag{B.2}$$

$$I_{flake}(\lambda) = \left| \frac{r_{02} e^{i(\Phi_1+\Phi_2)} + r_{12} e^{-i(\Phi_1-\Phi_2)} + r_{23} e^{-i(\Phi_1+\Phi_2)} + r_{01} r_{12} r_{23} e^{i(\Phi_1-\Phi_2)}}{e^{i(\Phi_1+\Phi_2)} + r_{01} r_{12} e^{-i(\Phi_1-\Phi_2)} + r_{01} r_{23} e^{-i(\Phi_1+\Phi_2)} + r_{12} r_{23} e^{i(\Phi_1-\Phi_2)}} \right|^2 . \tag{B.3}$$

In this calculation, the subscripts 0, 1, 2, and 3 refer to air (treated as vacuum), CrI_3, SiO_2, and Si, respectively. The amplitude of the reflected path at the interface between media *j* and *k* is given by r_{jk} in equation (B.5) and is calculated from the complex refractive indices defined in equation (B.4). Φ_j is the phase shift introduced by the interaction between light of wavelength λ and medium *j* with thickness d_j shown in equation (B.6).

$$\tilde{n}_j(\lambda) = n_j - i\kappa_j \tag{B.4}$$

$$r_{jk} = \frac{\tilde{n}_j - \tilde{n}_k}{\tilde{n}_j + \tilde{n}_k} \tag{B.5}$$

$$\Phi_j = \frac{2\pi \tilde{n}_j d_j}{\lambda} . \tag{B.6}$$

As can be noted from the previous expressions, if one wants to model *C* using the Fresnel equations, the complex index of refraction of the material under study must be known. The reflectivity of CrI_3 measured in vacuum at 300 K at normal incidence of a single crystal platelet of CrI_3 has been previously reported[69]. This data was used to calculate the phase of the amplitude reflection coefficient θ at energies in the visible range by numerical integration, according to the

Kramers-Kronig relation (B.7). The refractive index n and extinction coefficient κ of CrI_3 were then obtained throughout the visible range by combining equations (B.8) and (B.9) at each energy value. The results are plotted in Figure 3.

$$\theta(E) = -\frac{E}{\pi}\int_0^\infty \frac{\ln\left[R(E')\right]}{(E')^2 - E^2}\,dE' \tag{B.7}$$

$$r(E) = \sqrt{R(E)}e^{i\theta(E)} \tag{B.8}$$

$$r(E) = \frac{n(E) - 1 + i\kappa(E)}{n(E) + 1 + i\kappa(E)}. \tag{B.9}$$

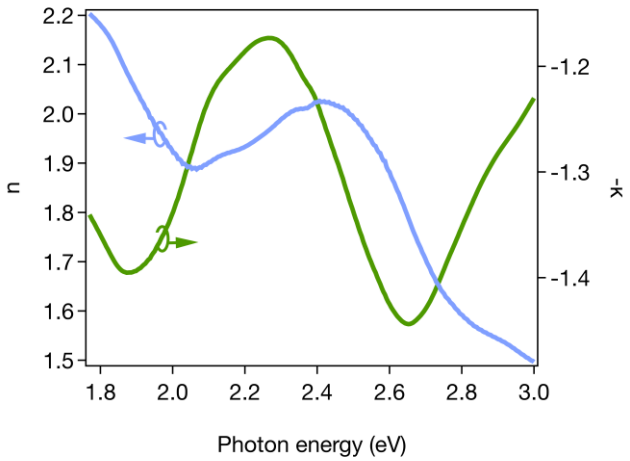

Figure B.1. Computed index of refraction of bulk CrI_3. Real (n) and imaginary (k) components are plotted as a function of photon energy in the visible range.

Substituting in for the complex indices of refraction of CrI_3, Si and SiO_2 [103] in equations (B.2) and (B.3), one can calculate the expected value of C for flakes of different thicknesses as a function of the illumination wavelength. Figure B.2a shows the contrast map for CrI_3 considering a fixed thickness of 285 nm of the SiO_2 layer in the SiO_2/Si substrate. We also present a line cut of that plot at an illumination wavelength of 635 nm in Figure B.2b. It can be seen that the experimental data points follow closely the trend predicted by the model. Given that the method is non-destructive and can be performed inside a glove box for many different illumination wavelengths,

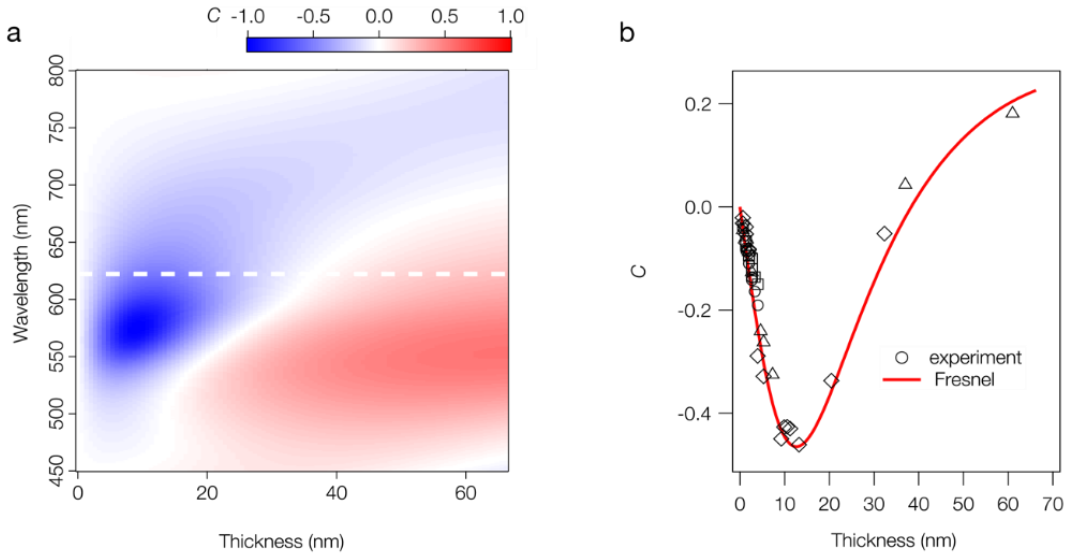

Figure B.2. Fresnel model for the optical contrast (*C*) of CrI_3 flakes on Si/285 nm SiO_2 substrates. **a**, Dependence of *C* with the number of layers for a CrI_3 flake as a function of the illumination wavelength. **b**, Comparison of the experimental data with the computed thickness dependence of *C* for a red-light-illuminated sample (line cut at 631 nm as shown by the dashed line in panel **a**). The different shape markers indicate data coming from different exfoliated samples.

the error in the determination of the number of layers can be reduced. This provides a fast and reliable method for the characterization of few-layer CrI_3 flakes.

Appendix C Supplementary Materials in Chapter 7

C1 Power dependence of monolayer PL

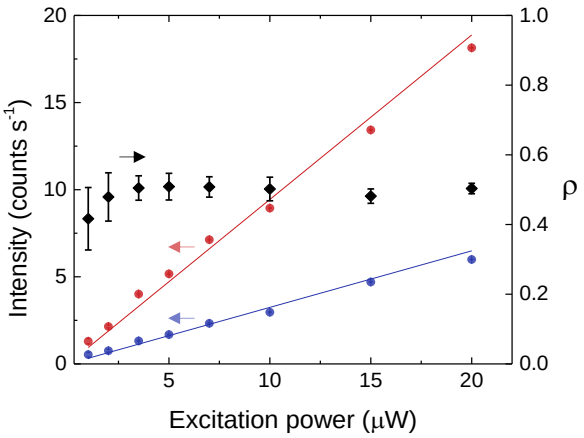

Figure C.1. Power dependence of monolayer PL Power dependence of σ^+ (red) and σ^- (blue) PL peak intensities and circular polarization (ρ, black). The data is taken at 0 T after decreasing from -0.5 T (same condition as in Figure 7.2d). Red and blue lines show a linear fit to the intensity data. We note that the low count rate prohibits accurate measurement of the PL below 1 μW. Furthermore, the power was kept less than or equal to 20 μW to avoid possible sample degradation. Error bars show the standard deviation of the intensities and ρ at the peak.

Appendix D Supplementary Materials for Chapter 8

D1 Comparison of two layered AFM domains of BD1

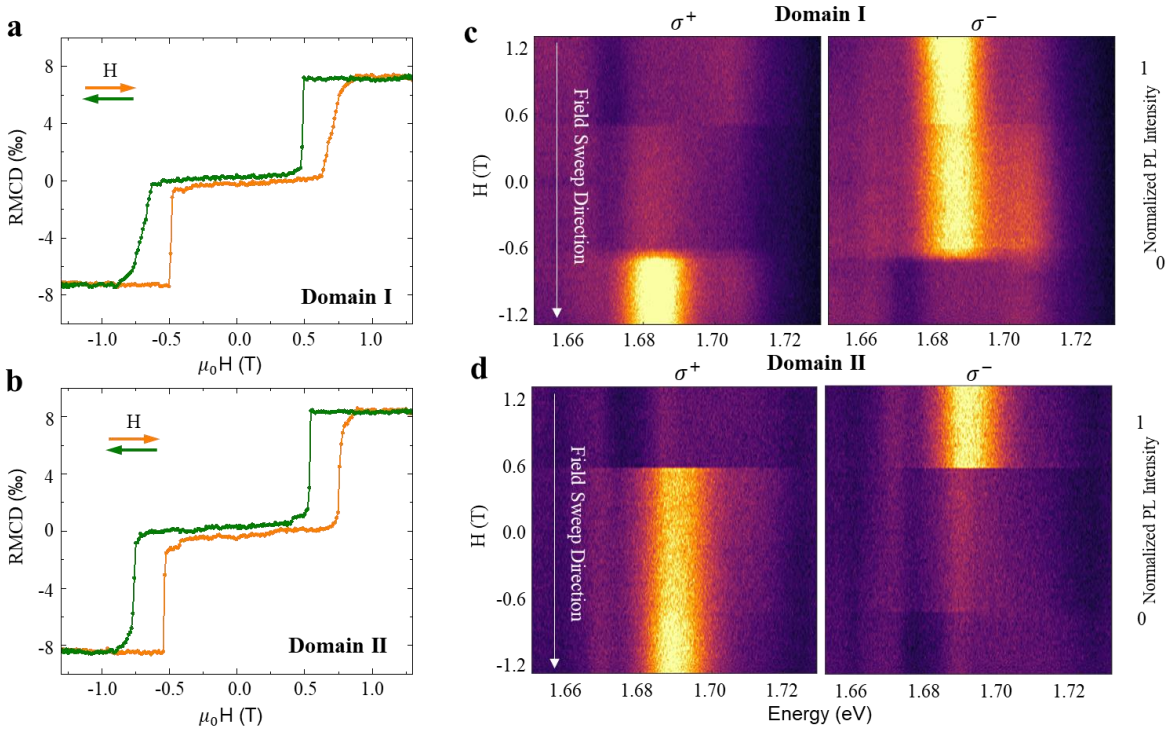

Figure D.1. Comparison of RMCD and polarization resolved PL of two layered antiferromagnetic domains of BD1. RMCD signal vs magnetic field of **a**, domain I and **b**, domain II. Co-circular polarization excitation and detection of **c**, domain I, and **b**, domain II. While there is little difference in RMCD between the two domains, polarization resolved PL can evidently resolve the two domains.

D2 ρ-H traces at two domains of bilayer device BD2.

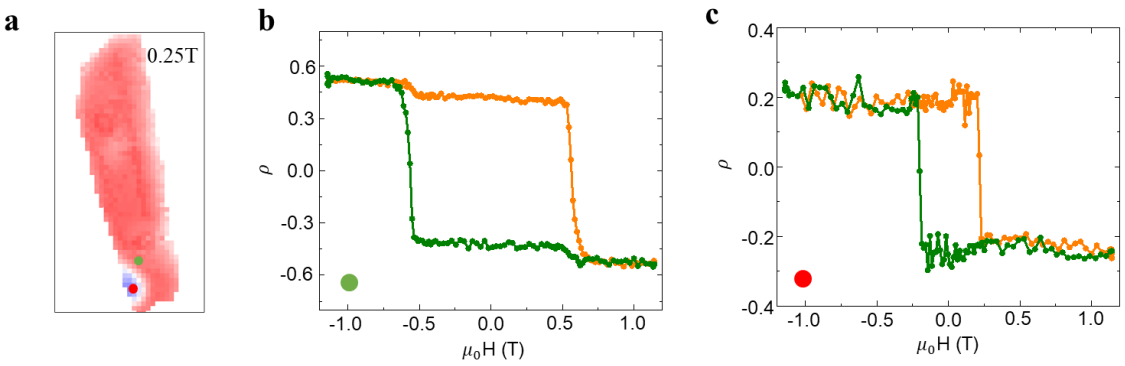

Figure D.2. ρ-H traces at two domains of bilayer device BD2. Two ρ-H traces were measured at locations denoted by yellow and purple dots in **a**. The results are shown in **b** and **c**, which are sharply contrasted. In **c**, we identified a FM domain where a ↑↑ to ↓↓ transition occurs at ~0.22T.

D3 Layered AFM/FM domains near the spin-flip transition in device BD1

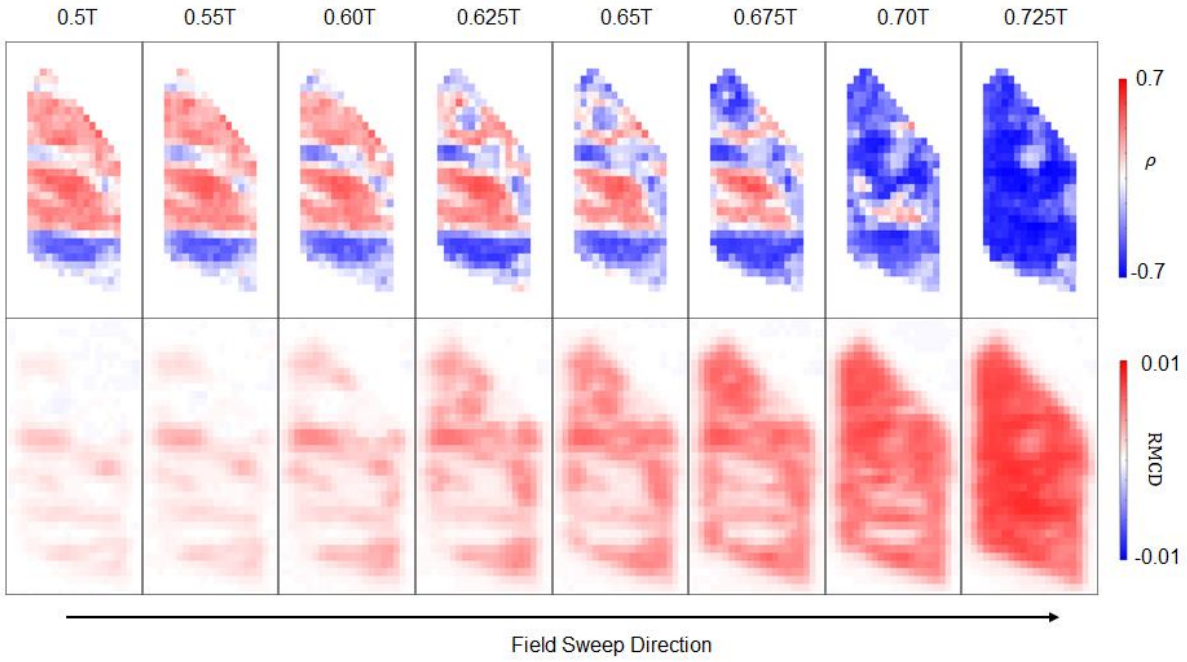

Figure D.3. Layered antiferromagnetic/ferromagnetic domains near the spin-flip transition in device BD1. Top and bottom rows show the spatial maps of ρ and RMCD, respectively, at selected magnetic fields μ_0H.

D4 Electron hopping model

The exchange interaction that leads to the valley splitting we observed in the experiment can be understood as a result of band edge shifting due to a second order electron/hole virtual hopping process. Here we present the model with monolayer WSe_2/bilayer CrI_3, and the analyzation for monolayer WSe_2/trilayer CrI_3 can be done similarly with minor modification.

We consider a kinetic exchange picture in which an excited electron in WSe_2's conduction band is allowed to hop between the WSe_2 and CrI_3's conduction band, with a hopping integral $-t_c$. For simplicity, we assume the interfacial CrI_3 has major spin pointing upward thus the hopping is with the spin up band in the +K valley of WSe_2.

In an AFM state CrI_3, where the bottom layer CrI_3 has the major spin pointing downward, this spin up electron considered above is thus spin forbidden to hop into the bottom layer. Using the basis specifying where the electron is located, the Hamiltonian can be written as a 2×2 matrix:

$$\boldsymbol{H}_c^{\boldsymbol{AFM}} = \begin{pmatrix} 0 & -t_c \\ -t_c & -\Delta_c \end{pmatrix} \begin{matrix} |\uparrow,\cdot\rangle \\ |\cdot,\uparrow\rangle \end{matrix} . \tag{D.1}$$

Here we have chosen the WSe_2's conduction band energy as zero of our energy scale. the $-\Delta_c$ is the band offset between WSe_2 and CrI_3's conduction band. $|\uparrow,\cdot\rangle$ and $|\cdot,\uparrow\rangle$ refer to the state with the electron located in the WSe_2 band and interfacial CrI_3 band, respectively.

The Hamiltonian is easily diagonalized with eigenenergies:

$$E_{\pm} = \frac{-\Delta_c \pm \sqrt{{\Delta_c}^2 + 4t^2}}{2} . \tag{D.2}$$

As for WSe_2 band, we take the solution with the plus sign. The energy shift thus for the WSe_2 conduction band is:

$$\Delta E_c^{AFM} = E_+ - 0 = \frac{-\Delta_c + \sqrt{\Delta_c{}^2 + 4t^2}}{2} \approx \frac{t^2}{\Delta_c} . \quad \text{(D.3)}$$

In an FM state CrI_3, the electron hopping from interfacial CrI_3 layer into the bottom CrI_3 layers is spin allowed, denoted with a hopping integral $-d_c$. The corresponding Hamiltonian can be written as a 3×3 matrix:

$$\boldsymbol{H}_c^{FM} = \begin{pmatrix} 0 & -t_c & 0 \\ -t_c & -\Delta_c & -d_c \\ 0 & -d_c & -\Delta_c \end{pmatrix} \begin{matrix} \left|\uparrow,\cdot,\cdot\right\rangle \\ \left|\cdot,\uparrow,\cdot\right\rangle \\ \left|\cdot,\cdot,\uparrow\right\rangle \end{matrix} . \quad \text{(D.4)}$$

Getting an algebraic expression for eigenenergies is not straightforward. However, using the downfolding method[104] to integrate out other states, partitioning the Hilbert space into states of interest, we could get a one-dimensional effective Hamiltonian in reduced Hilbert space:

$$E_{eff} = \begin{pmatrix} -t_c & 0 \end{pmatrix} \begin{pmatrix} \varepsilon + \Delta_c & d_c \\ d_c & \varepsilon + \Delta_c \end{pmatrix}^{-1} \begin{pmatrix} -t_c \\ 0 \end{pmatrix}, \quad = \frac{\Delta_c t_c{}^2}{(\Delta^2 - d_c{}^2)} \quad \text{(D.5)}$$

where in the last step we have set the ε, which is the typical energy for the states in reduced Hilbert space, to zero. Therefore, we obtained an algebraic approximation for the band edge shift of WSe_2 with the CrI_3 in FM state:

$$\Delta E_c^{FM} = E_{eff} = \frac{\Delta_c t_c{}^2}{(\Delta^2 - d_c{}^2)} \approx \frac{t_c{}^2}{\Delta_c}(1 + \frac{d_c{}^2}{\Delta_c{}^2}) . \quad \text{(D.6)}$$

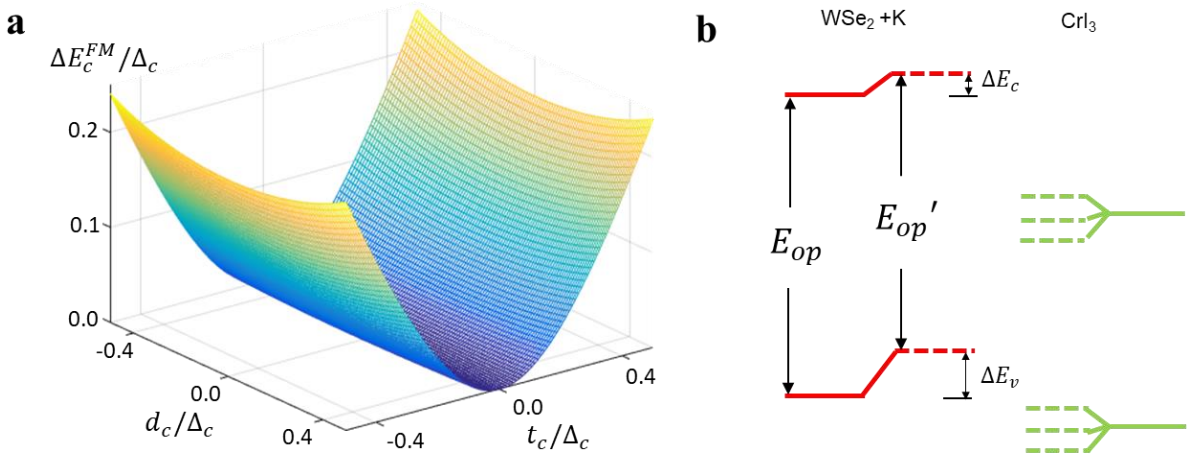

Figure D.4. Electron hopping model. (a). The induced energy shifting of WSe_2 conduction by Hopping Hamiltonian. **(b)**. Band diagram. For CrI_3, conduction and valence band in each layer are originally energetically degenerate. They splits into 3 bands when they are coupled, the coupling also pushes up the conduction band (CB) and valence band (CB) of WSe_2, leading to a change in optical resonance energy, the sign of which is determined on the relative magnitude of CB and VB shifting.

In Figure D.4a, we present the exact numerical solution for ΔE_c^{FM} as function of t_c and d_c by directly solving $\boldsymbol{H}_c^{\boldsymbol{FM}}$. We see a clear quadratic dependence on t_c and also a dependence on d_c in the form of $\frac{t_c^{\,2}}{\Delta_c}\cdot\frac{d_c^{\,2}}{\Delta_c^{\,2}}$. The $t_c^{\,2}$ factor in this term agrees with the fact the hopping from WSe_2 conduction band into bottom CrI_3 band is mediated by the interfacial CrI_3 layer.

To complete the picture, we also need to consider the hole hopping process as a consequence of type II band alignment between CrI_3 and WSe_2. A recent calculation indicates that the conduction band of CrI_3 is also major-spin polarized[105]. We hence could use a similar approach to deal with the valence band shift with a set of different variables, t_v, d_v, and Δ_v, obtaining the band valence band edge shift ΔE_v^{FM} and ΔE_v^{AFM}. The measured Zeeman splitting in the photoluminescence is the difference between the conduction and valence band shifts, expressed as

$$\Delta E_{optical}^{FM} = \Delta E_c^{FM} - \Delta E_v^{FM} \tag{D.7}$$

for FM state and

$$\Delta E_{optical}^{AFM} = \Delta E_{c}^{AFM} - \Delta E_{v}^{AFM} \tag{D.8}$$

for AFM state.

The experimental result can be reproduced with reasonable choices for the parameters. For example, taking t_c =150meV, d_c =150meV, Δ_c = 490meV[43], t_v =122.6meV, d_v =67.7meV $\Delta_v = 280\text{meV}$[3], . we end up with $\Delta E_{optical}^{FM} = -2.3\text{meV}$ and $\Delta E_{optical}^{AFM} = -3.83\text{meV}$, which agrees with the result presented in Figure 8.2d pretty well. However, we note that these parameters are not uniquely determined by the valley splitting. The precise determination of these parameters requires further experimental (e.g. angle-resolved photoemission spectroscopy) and computational studies.

Appendix E Supplementary Materials for Chapter 9

E1 Power-dependent hysteresis and switching of the valley Zeeman splitting

Figure E.1 provides similar data to Figure 9.2 in Chapter 9 for the valley Zeeman splitting (Δ). It is clear that Δ exhibits the same power-dependent hysteresis loop as ρ (Figure 9.2a). We are thus able to control Δ with the optical excitation power at fixed magnetic fields near the hysteresis loop, as shown in the 2D plot of Δ in Figure E.1b. The sign of the valley Zeeman splitting is tunable from positive to negative (and the reverse) when the external magnetic field is between ~0.82 T and 0.9 T. The curved white region indicates the critical excitation power that is required to switch the sign of Δ at the different fixed magnetic fields.

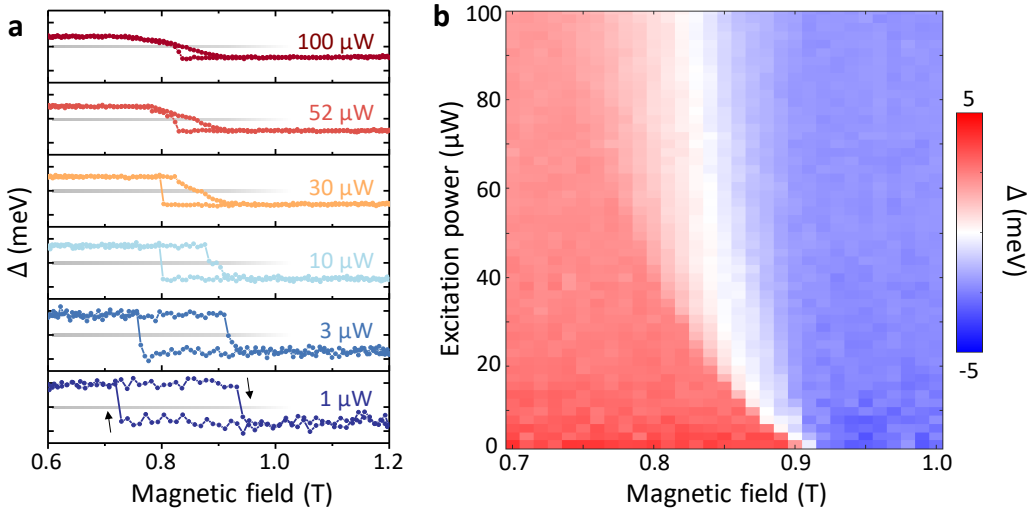

Figure E.1. Power dependent hysteresis and switching of the valley Zeeman splitting.(**a**) Valley Zeeman splitting (Δ) as a function of magnetic field sweeping from 0.6 to 1.2 to 0.6 T. The gray horizontal lines indicate the y-axis zero lines and the neighboring y-axis tick marks denote $\Delta = \pm 4$ meV. Black arrows indicate the sweep directions. These data are extracted from the same spectra used in Fig. 2a of the Chapter 9. (**b**) Map of the power dependence at different applied magnetic fields for Δ. The magnetic field was first initialized by sweeping up to 0.7 T. A power dependence was then performed from 1 to 100 μW at the different fixed magnetic fields from 0.7 to 1 T. These are extracted from the same dataset as Fig. 9.2 from the chapter 9.

E2 Power Dependent RMCD

In this section, we elaborate on our power-dependent measurements of the reflection magnetic circular dichroism (RMCD), which is proportional to the CrI_3 magnetization. We ignore the direct influence of the external magnetic field on the WSe_2 valley polarization since the exchange field due to the CrI_3 is much stronger (~10 T). In Figure E.2., we show the magnetic field dependence of the RMCD signal, which should be compared to the similar study for ρ from Figure 9.2a of Chapter 9. The RMCD exhibits a very similar power-dependent hysteresis loop behavior to ρ. As with ρ, the full-width of the RMCD loop decreases and the width of the transition region (where the RMCD signal jumps) increases with increasing power. However, unlike ρ, the RMCD does not switch signs. In addition, these RMCD steps (~0.013) are about 1/8 of the saturation value at 2.3 T in Figure 9.5a (~0.103), which indicates that the magnetization changes by the same

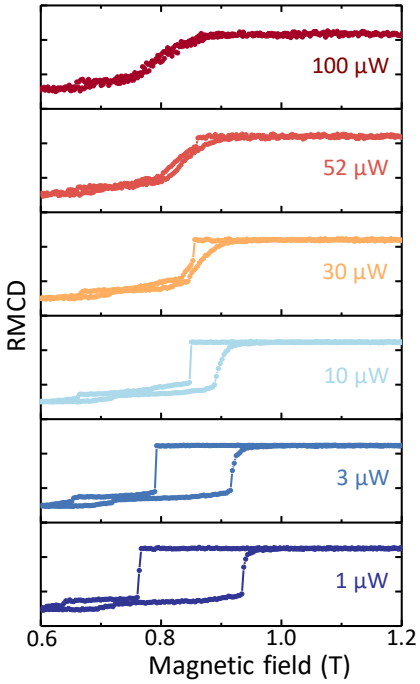

Figure E.2. Power dependent RMCD. Magnetic field dependence of the RMCD from 0.6 to 1.2 to 0.6 T at selected excitation powers. The RMCD range in each box is from 0.03 to 0.06 and the tick marks are separated by 0.01. The RMCD and field range is same as shown by the dashed box in Figure 9.5a.

fraction. If we assume that the step corresponds to a magnetization flip within a single CrI_3 layer, it implies that the CrI_3 is 16 layers thick, or ~10.6 nm (~0.66 nm per layer[42]). This is consistent with the ~10 nm CrI_3 thickness that we measured by atomic force microscopy. The measurements thus demonstrate that the valley switching originates from the photoinduced flipping of a single layer of CrI_3 magnetization. Furthermore, because the exchange interactions between WSe_2 and CrI_3 are short-ranged, the top CrI_3 layer dominantly influences the WSe_2 valley pseudospin behavior and is responsible for the valley switching effects. While the same power-dependent hysteresis may also occur on domain B, the affected CrI_3 layers are likely too far from the heterostructure interface to have a significant impact on the WSe_2 valley physics.

As discussed in Chapter 9, the origin of the optical control of the CrI_3 layer magnetization is an interesting issue for further study. One potentially important point to emphasize is that the focused laser spot (~1 μm^2) is significantly smaller than the sample. Therefore, in comparing the temperature and power dependences, future analyses should consider the difference between local laser induced heating and the global effects of higher temperature. In addition, the inhomogeneous distribution of photo-excited carriers from the laser spatial profile can be relevant, as it may provide a spatially dependent magnetic anisotropy across the laser spot that affects the hysteresis behavior. It will be important to systematically explore these issues, as well as the impact of laser excitation on the deeper CrI_3 layers and the magnetization jumps at different magnetic fields. Moreover, it will be both informative and fascinating to apply this technique to another CrI_3 van der Waals heterostructures.

Bibliography

1. Novoselov, K.S., et al., *Electric field effect in atomically thin carbon films.* Science, 2004. **306**(5696): p. 666-9.
2. Novoselov, K.S., et al., *Two-dimensional gas of massless Dirac fermions in graphene.* Nature, 2005. **438**: p. 197.
3. Nadj-Perge, S., et al., *Observation of Majorana fermions in ferromagnetic atomic chains on a superconductor.* Science, 2014. **346**(6209): p. 602.
4. Kane, C.L. and E.J. Mele, *Quantum Spin Hall Effect in Graphene.* Physical Review Letters, 2005. **95**(22): p. 226801.
5. Splendiani, A., et al., *Emerging Photoluminescence in Monolayer MoS_2.* Nano Letters, 2010. **10**(4): p. 1271-1275.
6. Zhang, Y., et al., *Experimental observation of the quantum Hall effect and Berry phase in graphene.* Nature, 2005. **438**: p. 201.
7. Geim, A.K., *Nobel Lecture: Random walk to graphene.* Reviews of Modern Physics, 2011. **83**(3): p. 851-862.
8. Shenderova, O.A., V.V. Zhirnov, and D.W. Brenner, *Carbon Nanostructures.* Critical Reviews in Solid State and Materials Sciences, 2002. **27**(3-4): p. 227-356.
9. Braga, S.F., et al., *Structure and Dynamics of Carbon Nanoscrolls.* Nano Letters, 2004. **4**(5): p. 881-884.
10. Mak, K.F., et al., *Atomically Thin MoS_2: A New Direct-Gap Semiconductor.* Physical Review Letters, 2010. **105**(13): p. 136805.
11. Radisavljevic, B., et al., *Single-layer MoS_2 transistors.* Nature Nanotechnology, 2011. **6**: p. 147.
12. Kim, B.S., et al., *Determination of the band parameters of bulk 2H-MX_2 (M = Mo, W; X = S, Se) by angle-resolved photoemission spectroscopy.* Scientific Reports, 2016. **6**: p. 36389.
13. Gunawan, O., et al., *Valley Susceptibility of an Interacting Two-Dimensional Electron System.* Physical Review Letters, 2006. **97**(18): p. 186404.
14. Mak, K.F., et al., *Control of valley polarization in monolayer MoS_2 by optical helicity.* Nature Nanotechnology, 2012. **7**: p. 494.
15. Zeng, H., et al., *Valley polarization in MoS_2 monolayers by optical pumping.* Nature Nanotechnology, 2012. **7**: p. 490.
16. Cao, T., et al., *Valley-selective circular dichroism of monolayer molybdenum disulphide.* Nature Communications, 2012. **3**: p. 887.
17. Yao, W., D. Xiao, and Q. Niu, *Valley-dependent optoelectronics from inversion symmetry breaking.* Physical Review B, 2008. **77**(23): p. 235406.
18. Bakun, A., et al., *Observation of a surface photocurrent caused by optical orientation of electrons in a semiconductor.* 1984. **40**(11).
19. Mak, K.F., et al., *The valley Hall effect in MoS_2 transistors.* 2014. **344**(6191): p. 1489-1492.
20. Gorbachev, R.V., et al., *Detecting topological currents in graphene superlattices.* Science, 2014. **346**(6208): p. 448.
21. Jones, A.M., et al., *Optical generation of excitonic valley coherence in monolayer WSe_2.* Nature Nanotechnology, 2013. **8**: p. 634.

22. Ross, J.S., et al., *Electrical control of neutral and charged excitons in a monolayer semiconductor.* Nature Communications, 2013. **4**: p. 1474.
23. Mak, K.F., et al., *Tightly bound trions in monolayer MoS_2.* Nature Materials, 2012. **12**: p. 207.
24. Zhang, L., et al., *Photonic-crystal exciton-polaritons in monolayer semiconductors.* Nature Communications, 2018. **9**(1): p. 713.
25. Aivazian, G., et al., *Magnetic control of valley pseudospin in monolayer WSe_2.* Nature Physics, 2015. **11**: p. 148.
26. Zhao, L., et al., *Influence of copper crystal surface on the CVD growth of large area monolayer graphene.* Solid State Communications, 2011. **151**(7): p. 509-513.
27. Li, X., et al., *Large-Area Synthesis of High-Quality and Uniform Graphene Films on Copper Foils.* Science, 2009. **324**(5932): p. 1312.
28. Blake, P., et al., *Making graphene visible.* Applied Physics Letters, 2007. **91**(6): p. 063124.
29. Huang, Y., et al., *Reliable Exfoliation of Large-Area High-Quality Flakes of Graphene and Other Two-Dimensional Materials.* ACS Nano, 2015. **9**(11): p. 10612-10620.
30. Zomer, P., et al., *Fast pick up technique for high quality heterostructures of bilayer graphene and hexagonal boron nitride.* Applied Physics Letters, 2014. **105**(1): p. 013101.
31. Ashcroft, N.W. and N.D. Mermin, *Solid state physics (saunders college, philadelphia, 1976).* Appendix N, 2010.
32. Baibich, M.N., et al., *Giant Magnetoresistance of (001)Fe/(001)Cr Magnetic Superlattices.* Physical Review Letters, 1988. **61**(21): p. 2472-2475.
33. Daughton, J., et al., *Magnetic field sensors using GMR multilayer.* IEEE Transactions on magnetics, 1994. **30**(6): p. 4608-4610.
34. Prinz, G.A., *Magnetoelectronics.* Science, 1998. **282**(5394): p. 1660.
35. Korenev, V.L., et al., *Dynamic spin polarization by orientation-dependent separation in a ferromagnet–semiconductor hybrid.* Nature Communications, 2012. **3**: p. 959.
36. Stiles, M.D., *Interlayer exchange coupling.* Journal of Magnetism and Magnetic Materials, 1999. **200**(1-3): p. 322-337.
37. Binasch, G., et al., *Enhanced magnetoresistance in layered magnetic structures with antiferromagnetic interlayer exchange.* Physical review B, 1989. **39**(7): p. 4828.
38. Buzdin, A.I., *Proximity effects in superconductor-ferromagnet heterostructures.* Reviews of modern physics, 2005. **77**(3): p. 935.
39. Lee, C., et al., *Direct measurement of proximity-induced magnetism at the interface between a topological insulator and a ferromagnet.* Nature communications, 2016. **7**: p. 12014.
40. Katmis, F., et al., *A high-temperature ferromagnetic topological insulating phase by proximity coupling.* Nature, 2016. **533**(7604): p. 513.
41. Koren, G., *Magnetic proximity effect of a topological insulator and a ferromagnet in thin-film bilayers of $Bi_{0.5}Sb_{1.5}Te_3$ and $SrRuO_3$.* Physical Review B, 2018. **97**(5): p. 054405.
42. McGuire, M.A., et al., *Coupling of Crystal Structure and Magnetism in the Layered, Ferromagnetic Insulator CrI_3.* Chemistry of Materials, 2015. **27**(2): p. 612-620.
43. Zhong, D., et al., *Van der Waals engineering of ferromagnetic semiconductor heterostructures for spin and valleytronics.* Science Advances, 2017. **3**(5): p. e1603113.

44. Srivastava, A., et al., *Valley Zeeman effect in elementary optical excitations of monolayer WSe_2.* Nature Physics, 2015. **11**: p. 141.
45. Wang, G., et al., *Magneto-optics in transition metal diselenide monolayers.* 2D Materials, 2015. **2**(3): p. 034002.
46. Mitioglu, A., et al., *Optical investigation of monolayer and bulk tungsten diselenide (WSe_2) in high magnetic fields.* Nano letters, 2015. **15**(7): p. 4387-4392.
47. Hellwig, O., et al., *A new phase diagram for layered antiferromagnetic films.* Nature materials, 2003. **2**(2): p. 112.
48. Hellwig, O., A. Berger, and E.E. Fullerton, *Domain walls in antiferromagnetically coupled multilayer films.* Physical review letters, 2003. **91**(19): p. 197203.
49. Yao, Y., et al., *Negative differential magnetization in ultrathin Fe on vicinal W (100).* Physical Review B, 2003. **67**(17): p. 174409.
50. Huang, B., et al., *Layer-dependent ferromagnetism in a van der Waals crystal down to the monolayer limit.* Nature, 2017. **546**: p. 270.
51. Novoselov, K.S., et al., *Unconventional quantum Hall effect and Berry's phase of 2π in bilayer graphene.* Nature Physics, 2006. **2**: p. 177.
52. Stryjewski, E. and N. Giordano, *Metamagnetism.* Advances in Physics, 1977. **26**(5): p. 487-650.
53. Zhang, W.-B., et al., *Robust intrinsic ferromagnetism and half semiconductivity in stable two-dimensional single-layer chromium trihalides.* Journal of Materials Chemistry C, 2015. **3**(48): p. 12457-12468.
54. Soumyanarayanan, A., et al., *Emergent phenomena induced by spin–orbit coupling at surfaces and interfaces.* Nature, 2016. **539**: p. 509.
55. Bruno, P., *Absence of Spontaneous Magnetic Order at Nonzero Temperature in One- and Two-Dimensional Heisenberg and XY Systems with Long-Range Interactions.* Physical Review Letters, 2001. **87**(13): p. 137203.
56. Mermin, N.D. and H. Wagner, *Absence of Ferromagnetism or Antiferromagnetism in One- or Two-Dimensional Isotropic Heisenberg Models.* Physical Review Letters, 1966. **17**(22): p. 1133-1136.
57. Sato, K., *Measurement of Magneto-Optical Kerr Effect Using Piezo-Birefringent Modulator.* Japanese Journal of Applied Physics, 1981. **20**(12): p. 2403-2409.
58. Baberschke, K. and M. Farle, *Higher-order contribution and temperature dependence of the magnetic anisotropy in ultrathin films (invited).* Journal of Applied Physics, 1997. **81**(8): p. 5038-5043.
59. Lee, J.-U., et al., *Ising-Type Magnetic Ordering in Atomically Thin $FePS_3$.* Nano Letters, 2016. **16**(12): p. 7433-7438.
60. Gong, C., et al., *Discovery of intrinsic ferromagnetism in two-dimensional van der Waals crystals.* Nature, 2017. **546**: p. 265.
61. Deng, Y., et al., *Gate-tunable room-temperature ferromagnetism in two-dimensional Fe3GeTe2.* Nature, 2018. **563**(7729): p. 94-99.
62. Fei, Z., et al., *Two-dimensional itinerant ferromagnetism in atomically thin Fe_3GeTe_2.* Nature Materials, 2018. **17**(9): p. 778-782.
63. Bonilla, M., et al., *Strong room-temperature ferromagnetism in VSe_2 monolayers on van der Waals substrates.* Nature Nanotechnology, 2018. **13**(4): p. 289-293.

64. O'Hara, D.J., et al., *Room Temperature Intrinsic Ferromagnetism in Epitaxial Manganese Selenide Films in the Monolayer Limit.* Nano Letters, 2018. **18**(5): p. 3125-3131.
65. Seyler, K.L., et al., *Ligand-field helical luminescence in a 2D ferromagnetic insulator.* Nature Physics, 2018. **14**(3): p. 277-281.
66. Tsubokawa, I., *On the Magnetic Properties of a $CrBr_3$ Single Crystal.* Journal of the Physical Society of Japan, 1960. **15**(9): p. 1664-1668.
67. Foster, L.S., *New developments in ferromagnetic materials.* Journal of Chemical Education, 1948. **25**(6): p. 360.
68. Dillon, J.F., H. Kamimura, and J.P. Remeika, *Magnetic Rotation of Visible Light by Ferromagnetic $CrBr_3$.* Physical Review Letters, 1962. **9**(4): p. 161-163.
69. Grant, P. M., and G. B. Street. "*OPTICAL PROPERTIES OF CHROMIUM TRIHALIDES IN REGION 1-11 eV*." In BULLETIN OF THE AMERICAN PHYSICAL SOCIETY, vol. 13, no. 3, p. 415. CIRCULATION FULFILLMENT DIV, 500 SUNNYSIDE BLVD, WOODBURY, NY 11797-2999: AMER INST PHYSICS, 1968.
70. McIntyre, J.D.E. and D.E. Aspnes, *Differential reflection spectroscopy of very thin surface films.* Surface Science, 1971. **24**(2): p. 417-434.
71. Shinagawa, K., et al., *Charge-transfer transitions in chromium trihalides.* Journal of Physics: Condensed Matter, 1996. **8**(44): p. 8457-8463.
72. McAven, L.F., et al., *The Kerr magneto-optic effect in ferromagnetic $CrBr_3$.* Journal of Physics B: Atomic, Molecular and Optical Physics, 1999. **32**(3): p. 563-576.
73. Dillon, J.F., H. Kamimura, and J.P. Remeika, *Magneto-optical properties of ferromagnetic chromium trihalides.* Journal of Physics and Chemistry of Solids, 1966. **27**(9): p. 1531-1549.
74. Pollini, I. and G. Spinolo, *Intrinsic Optical Properties of $CrCl_3$.* physica status solidi (b), 1970. **41**(2): p. 691-701.
75. Bermudez, V.M. and D.S. McClure, *Spectroscopic studies of the two-dimensional magnetic insulators chromium trichloride and chromium tribromide—I.* Journal of Physics and Chemistry of Solids, 1979. **40**(2): p. 129-147.
76. Knochenmuss, R., et al., *Broadband near‐infrared luminescence of Cr_3 in the elpasolite lattices $Cs_2NaInCl_6$, Cs_2NaYCl_6, and Cs_2NaYBr_6.* The Journal of Chemical Physics, 1986. **85**(8): p. 4280-4289.
77. Barton, T.J. and R.C. Slade, *Chemical significance of ligand-field parameters in chromium(III) complexes of quadrate symmetry.* Journal of the Chemical Society, Dalton Transactions, 1975(8): p. 650-657.
78. Wei, P., et al., *Strong interfacial exchange field in the graphene/EuS heterostructure.* Nature Materials, 2016. **15**: p. 711.
79. Zhao, C., et al., *Enhanced valley splitting in monolayer WSe_2 due to magnetic exchange field.* Nature Nanotechnology, 2017. **12**: p. 757.
80. Zhong, D., et al., *Van der Waals engineering of ferromagnetic semiconductor heterostructures for spin and valleytronics.* Science Advances, 2017. **3**(5).
81. Gong, C., et al., *Discovery of intrinsic ferromagnetism in two-dimensional van der Waals crystals.* Nature, 2017. **546**(7657): p. 265-269.
82. Lin, M.-W., et al., *Ultrathin nanosheets of $CrSiTe_3$: a semiconducting two-dimensional ferromagnetic material.* Journal of Materials Chemistry C, 2016. **4**(2): p. 315-322.

83. Tian, Y., et al., *Magneto-elastic coupling in a potential ferromagnetic 2D atomic crystal.* 2D Materials, 2016. **3**(2): p. 025035.
84. Wang, X., et al., *Raman spectroscopy of atomically thin two-dimensional magnetic iron phosphorus trisulfide ($FePS_3$) crystals.* 2D Materials, 2016. **3**(3): p. 031009.
85. Ghazaryan, D., et al., *Magnon-assisted tunnelling in van der Waals heterostructures based on $CrBr_3$.* Nature Electronics, 2018. **1**(6): p. 344-349.
86. Zhang, Z., et al., *Direct Photoluminescence Probing of Ferromagnetism in Monolayer Two-Dimensional $CrBr_3$.* Nano Letters, 2019. **19**(5): p. 3138-3142.
87. McGuire, M.A., et al., *Magnetic behavior and spin-lattice coupling in cleavable van der Waals layered $CrCl_3$ crystals.* Physical Review Materials, 2017. **1**(1): p. 014001.
88. May, A.F., et al., *Ferromagnetism Near Room Temperature in the Cleavable van der Waals Crystal Fe_5GeTe_2.* ACS Nano, 2019. **13**(4): p. 4436-4442.
89. Thiel, L., et al., *Probing magnetism in 2D materials at the nanoscale with single-spin microscopy.* Science, 2019: p. eaav6926.
90. Song, T., et al., *Giant tunneling magnetoresistance in spin-filter van der Waals heterostructures.* Science, 2018. **360**(6394): p. 1214-1218.
91. Klein, D.R., et al., *Probing magnetism in 2D van der Waals crystalline insulators via electron tunneling.* Science, 2018. **360**(6394): p. 1218-1222.
92. Wang, Z., et al., *Very large tunneling magnetoresistance in layered magnetic semiconductor CrI_3.* Nature Communications, 2018. **9**(1): p. 2516.
93. Kim, H.H., et al., *One Million Percent Tunnel Magnetoresistance in a Magnetic van der Waals Heterostructure.* Nano Letters, 2018. **18**(8): p. 4885-4890.
94. Jiang, S., J. Shan, and K.F. Mak, *Electric-field switching of two-dimensional van der Waals magnets.* Nature Materials, 2018. **17**(5): p. 406-410.
95. Huang, B., et al., *Electrical control of 2D magnetism in bilayer CrI_3.* Nature Nanotechnology, 2018. **13**(7): p. 544-548.
96. Jiang, S., et al., *Controlling magnetism in 2D CrI_3 by electrostatic doping.* Nature Nanotechnology, 2018. **13**(7): p. 549-553.
97. Seyler, K.L., et al., *Valley Manipulation by Optically Tuning the Magnetic Proximity Effect in WSe_2/CrI_3 Heterostructures.* Nano Letters, 2018. **18**(6): p. 3823-3828.
98. Jones, A.M., et al., *Optical generation of excitonic valley coherence in monolayer WSe_2.* Nat Nano, 2013. **8**(9): p. 634-638.
99. Astakhov, G.V., et al., *Nonthermal Photocoercivity Effect in a Low-Doped (Ga,Mn)As Ferromagnetic Semiconductor.* Physical Review Letters, 2009. **102**(18): p. 187401.
100. Zakharchenya, B.P. and V.L. Korenev, *Integrating magnetism into semiconductor electronics.* Physics-Uspekhi, 2005. **48**(6): p. 603-608.
101. Beal, A.R. and W.Y. Liang, *Reflectivity spectra of some first row transition metal intercalates of NbS_2.* The Philosophical Magazine: A Journal of Theoretical Experimental and Applied Physics, 1976. **33**(1): p. 121-131.
102. Castellanos-Gomez, A., et al., *Fast and reliable identification of atomically thin layers of $TaSe_2$ crystals.* Nano Research, 2013. **6**(3): p. 191-199.
103. Herzinger, C., et al., *Ellipsometric determination of optical constants for silicon and thermally grown silicon dioxide via a multi-sample, multi-wavelength, multi-angle investigation.* Journal of Applied Physics, 1998. **83**(6): p. 3323-3336.

104. Wu, M., et al., *Physical origin of giant excitonic and magneto-optical responses in two-dimensional ferromagnetic insulators.* eprint arXiv:1903.07787, 2019: p. arXiv:1903.07787.
105. Koch, E., *7 Exchange Mechanisms.* Correlated Electrons: From Models to Materials: p. 41.

VITA

Ding was born in Hubei, China to Wenan Hu and Dongsheng Zhong and was raised in City of Wuhan. He was keen on math since primary school, and won many city-level and national wide math competitions. After he entered high school, he started to develop interests in Physics. He thought it was cool for physics laws to predict the motion of almost anything in the world, and he liked it that the math he had learnt can be put to practical use. He attended Peking university where he found the Condense Matter Experiment to be his research interest after many trails. He was admitted by the University of Washington and began his physics PhD pursuit since 2014.